DISS. ETH No. 28948

From Ferroelectricity to Quantum Paraelectricity — Evolution and Doping from First Principles

Submitted to obtain the title of

DOCTOR OF SCIENCES
(Dr. sc. ETH Zurich)

Presented by

TOBIAS MICHAEL ESSWEIN
MSc ETH in Materials Science, ETH Zurich

born on 02.10.1992

citizen of Germany

Accepted on the recommendation of

Prof. Dr. Nicola A. Spaldin, examiner
Prof. Dr. Morgan Trassin, co-examiner
Prof. Dr. Rossitza Pentcheva, co-examiner

2022

Tobias Michael Esswein
From Ferroelectricity to Quantum Paraelectricity —
Evolution and Doping from First Principles
December 2022

Abstract

Quantum paraelectric materials like $SrTiO_3$ and $KTaO_3$ exhibit many unusual material properties arising from their quantum fluctuations, including a high dielectric constant and unconventional superconductivity. In combination with other unusual properties like strong spin orbit coupling and charged ionic layers in $KTaO_3$, this leads to the observation of various intriguing phenomena. The primary goal of this thesis is to investigate these ferroelectric and quantum paraelectric states, with a focus on the evolution of polarization, quantum fluctuations and electron-phonon coupling with chemistry and doping, using computational first-principle methods and $SrTiO_3$, $KTaO_3$ and $BaTiO_3$ as model systems.

To achieve this goal, I first investigate ferroelectric polarization in $BaTiO_3$ and how it can persist despite the presence of free charge carriers, two principally contraindicated phenomena. Next, I create a model, based on quantities easily extracted from DFT and DFPT calculations, to better understand the quantum paraelectric state and use this model to study the so-called isotope effect in $SrTiO_3$. Finally, I calculate the electron-phonon coupling strength in $KTaO_3$, motivated by its highly anisotropic surface superconductivity, to gain insight into which phonon modes may be relevant for the electron-phonon pairing mechanism.

From the study of $BaTiO_3$, we learn both that polarity and metallicity can coexist in an originally ferroelectric material, up to relatively high doping levels, and how doping ions affect the geometry and polarization of the resulting structure, ranging from complete suppression to an unexpected increase of polarization. Next, we show that the simple model for quantum paraelectricity works well and see that the actual isotope effect in $SrTiO_3$, namely the substitution of ^{16}O with its heavier isotope ^{18}O, probably has a smaller effect than expected and geometry effects may be more important than initially thought.

The electron-phonon coupling calculations show that while there is no direct correlation between the orientation dependence of the coupling strength λ and the experimentally measured superconducting critical temperatures, confirming that classical BCS theory is not directly applicable to $KTaO_3$, a strong localization of λ around Γ indicates a pairing mechanism involving the polar soft mode.

Overall, this thesis reveals new insights into the relationship between chemistry, conductivity, ferroelectricity, quantum paraelectricity and electron-phonon interactions in this important class of materials.

ZUSAMMENFASSUNG

Quantenparaelektrische Materialien wie $SrTiO_3$ und $KTaO_3$ weisen viele ungewöhnliche Materialeigenschaften auf, die auf ihre Quantenfluktuation zurückzuführen sind, unter anderem eine hohe Dielektrizitätskonstante und unkonventionelle Supraleitung. In Kombination mit anderen unüblichen Eigenschaften, wie zum Beispiel einer starken Spin-Bahn-Kopplung und geladenen ionischen Schichten in $KTaO_3$, führt dies zu sehr interessanten Phänomenen. Das primäre Ziel dieser Arbeit ist es, diese ferroelektrischen und quantenparaelektrischen Zustände zu untersuche, mit $SrTiO_3$, $KTaO_3$ und $BaTiO_3$ als Modellsystemen und computergestützten *ab-initio* Methoden. Der Schwerpunkt liegt dabei auf der Entwicklung der Polarisation, der Quantenfluktuationen und der Elektron-Phonon-Kopplung in Abhängigkeit von der Chemie und der Dotierung.

Um dieses Ziel zu erreichen, untersuche ich zunächst die ferroelektrische Polarisation in $BaTiO_3$ und wie sie trotz der Anwesenheit von freien Ladungsträgern bestehen bleiben kann – zwei sich grundsätzlich ausschliessende Phänomene. Als Nächstes erstelle ich ein Modell, das auf leicht aus DFT- und DFPT-Berechnungen zu extrahierenden Grössen basiert, um den quantenparaelektrischen Zustand besser zu verstehen, und verwende dieses Modell, um den sogenannten Isotopeneffekt in

$SrTiO_3$ zu untersuchen. Motiviert durch die hochgradig anisotrope Oberflächensupraleitung berechne ich schliesslich die Elektron-Phonon-Kopplungsstärke in $KTaO_3$, um besser verstehen zu können, welche Phononmoden für den Mechanismus dieser Kopplung relevant sein könnten.

Aus der Untersuchung von $BaTiO_3$ lernen wir, dass Polarisation und metallische Leitungsfähigkeit in einem ursprünglich ferroelektrischen Material bis zu relativ hohen Dotierungswerten koexistieren können. Zudem sehen wir, wie sich Dotierungsionen auf die Geometrie und Polarisation der resultierenden Struktur auswirken, von der vollständigen Unterdrückung bis hin zu einer unerwarteten Erhöhung der Polarisation. Wir zeigen, dass das Modell für Quantenparaelektrizität funktioniert und dass der effektive Isotopeneffekt in $SrTiO_3$, nämlich die Substitution von ^{16}O durch das schwerere Isotop ^{18}O, wahrscheinlich einen geringeren Effekt hat und dass Geometrieeffekte wichtiger sein könnten als bisher angenommen. Die Berechnung der Elektron-Phonon-Kopplungsstärke zeigt, dass es keine direkte Korrelation zwischen der Orientierungsabhängigkeit der Kopplungsstärke λ und den experimentell gemessenen supraleitenden kritischen Temperaturen gibt, was bestätigt, dass die klassische BCS-Theorie nicht direkt auf $KTaO_3$ anwendbar ist. Eine starke Lokalisierung von λ um Γ deutet aber darauf hin, dass die polare Phononmode am Paarungsmechanismus wesentlich beteiligt ist.

Insgesamt liefert diese Arbeit neue Erkenntnisse über die Beziehungen zwischen Chemie, Leitfähigkeit, Ferroelektrizität, Quantenparaelektrizität und Elektron-Phonon-Wechselwirkungen in dieser wichtigen Materialklasse.

Acknowledgments

This work would not have been possible without the great support, scientific knowledge and intuition of my PhD supervisor Nicola Spaldin. I want to thank Nicola not only for her scientific guidance, but also for making those almost two years of more-or-less isolation during the Covid-19 pandemic as pleasant and productive as possible, by always looking after everyone's well-being, especially that of all the new group members who started during this period.

That brings me to Schrödingers' Kittens, all the current and former members of the Materials Theory group at ETH Zurich: Nicola, Claude, Andrea, Aria, Carl, Marek, Sayantika, Sophie, Alberto, Edith, Luca, Max, Peter, Tara, Xanthe, Alex, Awadhesh, Chiara, Jaime, Kane, Alex, Ankit, Bastien, Boris, Dominik, Florian, Maryam, Natalya, Quintin, Sophie, Veronica, Nelly, and all current and former master students. It was a pleasure working with you, discussing scientific (and not so scientific) topics and running at the SOLA every year. A special thanks to Alex, who guided me in my first steps with DFT calculations during my master's project on nickelates, and to Awadhesh, who, together with Nicola, laid the foundation for this work by introducing me to the fascinating topics of quantum paraelectricity and superconductivity during my master's thesis. I would especially like to thank both master students I had the pleasure to supervise: Veronica for her independent and inspired work, with which she contributed greatly to a part of this thesis, and Nelly, who within just a few weeks obtained many valuable results which are part of this thesis as well. Finally, a big thank you to Susanne for making life at ETH as unproblematic and smooth as possible and always being there to solve any issue that might arise.

A big thank you to my parents, Theo and Gerlinde, who made it possible for me to study materials science at ETH Zurich and start this scientific journey of more than eleven years, and to all my friends who made these years so much more memorable.

Last but not least, the biggest thank you goes to my fiancée Desirée, who has always been there for me, not only during my PhD, and without whose continuous support this whole endeavor would certainly not have been possible!

Contents

List of Figures

List of Tables

Acronyms

BCS	Bardeen-Cooper-Schrieffer
BTO	barium titanate, $BaTiO_3$
DFT	density functional theory
DFPT	density functional perturbation theory
DOS	density of states
EPC	electron-phonon coupling
EPW	electron-phonon coupling using Wannier functions
FE	ferroelectricity
KNO	potassium niobate, $KNbO_3$
KTO	potassium tantalate, $KTaO_3$
LDA	local density approximation
LO	longitudinal optical
PBE	Perdew-Burke-Ernzerhof
PBEsol	PBE revised for solids
QCP	quantum critical point
QE	Quantum Espresso
QPE	quantum paraelectricity
QPT	quantum phase transition
SC	superconductivity
SOC	spin-orbit coupling
STO	strontium titanate, $SrTiO_3$
TO	transverse optical
VASP	Vienna Ab initio Simulation Package
VCA	virtual crystal approximation

1

Introduction

Materials with the perovskite structure are astoundingly versatile, with applications ranging from capacitors and piezoelectric actuators [1, 2] to highly efficient electro-chemical water-splitting [3, 4], solar cells [5] and solid-oxide fuel cells [6]. Their general chemical formula is ABX_3, with A and B being two different cations, and X being the anion, often O^{2-}. The high-symmetry reference structure is cubic, with the A and B ions sitting at the middle and the corners of the cube, respectively, and the oxygen ions sitting on the edge centers, enclosing the B ion in a octahedral fashion (see figure 1.1).

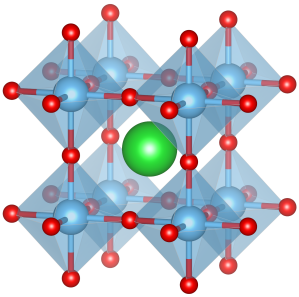

Figure 1.1: High-symmetry cubic perovskite crystal structure with chemical formula ABO_3 and $Fm\bar{3}m$ symmetry (spacegroup 225). The A ion sits in the middle of the cube and eight B ions at each corner, each contributing $1/8$ to the atom count per formula unit. The oxygen ions surround each B ion in a octahedron, each oxygen sitting at the center of one of the cube's edges.

An important property for perovskites is the so-called *Goldschmidt* or tolerance factor

$$t = \frac{r_A + r_O}{\sqrt{2}(r_B + r_O)} \quad , \tag{1.1}$$

with r_X being the respective ionic radii. If $t \sim 1$, then the perovskite structure is formed, and if $t = 1$, the cubic structure without distortions should be most stable. If $t > 1$, then the B atom is too small for the space it is supposed to occupy, and a polar distortion may occur (BTO is a good example for this). If $t < 1$, then the A atom is too small and the oxygen octahedra usually rotate or tilt to lower the overall energy (STO is a good example).

These frequently observed symmetry-lowering distortions can be separated into three distinct groups, as categorized by Megaw [7] and Glazer [8]. The first is the tilting of the anion octahedra, as e.g. observed in STO in its "soft-mode" phase transition at 105 K, where the oxygen octahedra rotate in alternating directions around the c-axis [9]. The second group consists of polar displacements of the cations relative to the anions in either a ferroelectric or antiferroelectric manner. A good example for a ferroelectric perovskite is $BaTiO_3$, which undergoes three phase transitions to ferroelectric phases. The third group is distortions of the octahedra themselves, one example being the breathing mode in rare earth nickelates [10].

Because the perovskite structure is quite flexible, both in the choice of ions occupying its A, B and X sites, and in the small structural differences between phases, the actual chemistry can be tuned to enable the many interesting phenomena and wide array of applications mentioned in the beginning.

In the following part, I will first give a description of the phenomena relevant for this thesis, and then cover the three perovskite materials in which these phenomena can be observed and which we study here. A brief overview of the structure of this thesis completes this chapter.

1.1 Phenomena

1.1.1 Ferroelectricity

Ferroelectric materials show a spontaneous electric polarization that is switchable by an external field, the latter requirement means that

they are usually insulating. Ferroelectricity is a structural effect, meaning that atoms of different charges need to be off-centered relative to each other for the polarization to arise, making any ferroelectric a non-centrosymmetric material lacking an inversion center. Many different materials show ferroelectricity, from Rochelle salt (the first discovered ferroelectric) to the prototypical examples $BaTiO_3$ and $PbZr_{1-x}Ti_xO_3$ (PZT, one of the most technologically important ones). Their applications range from piezo- or pyroelectric actuators and sensors [11] to ferroelectric memories [12] and solar cells [13]. Note that not all piezo- and pyroelectrics are ferroelectric, but all ferroelectrics must be piezo- and pyroelectric.

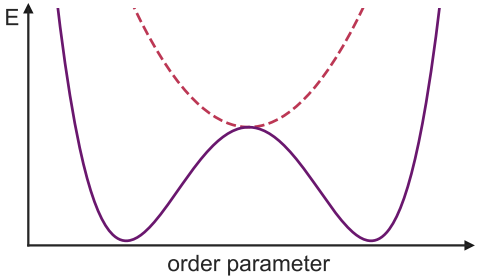

FIGURE 1.2: Schematic evolution of the Landau free energy, corresponding to eq. 1.2, going e.g. from a paraelectric phase (dashed line) with one non-polar energy minimum, to a ferroelectric phase (solid line) with two energy minima of opposite polarization.

The theoretical description of the ferroelectric phase transition is based on the Landau theory of second-order phase transitions and can be described by the softening of a phonon mode, as first described by Cochran [14]. The energy landscape of the para- and ferroelectric phase is given by the phenomenological fourth-order Landau free energy

$$F(T,\eta) = F_0 + a(T)\eta^2 + \frac{b(T)}{2}\eta^4 \quad , \tag{1.2}$$

with T being the temperature, ν the order parameter and $a(T)$ and $b(T)$ being parameters. $b(T)$ is usually assumed to be constant close to the critical temperature, and must be larger than zero ($b(T) \sim b_0 > 0$).

$a(T)$ changes sign across the phase transition, being positive at higher temperatures and negative below ($a(T) \sim a_0(T - T_c)$). The free energies above and below the phase transition are visualized in fig. 1.2.

Experimentally, one can observe such a phase transition by e.g. measuring the transverse optical (TO) phonon frequency ω_{TO} at Γ, which softens upon approaching the critical temperature, following $\omega_{TO} \propto (T - T_c)^{1/2}$ in both the ferroelectric and paraelectric phase, as visualized in fig. 1.3.

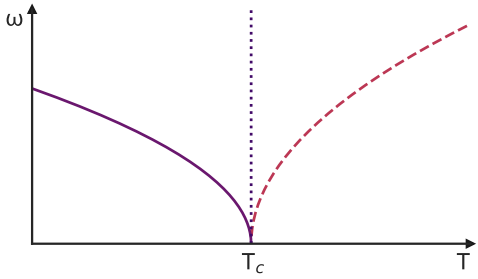

FIGURE 1.3: Development of the soft mode phonon frequency ω with temperature. Upon cooling (coming from the right), the phonon frequency in the paraelectric phase (dashed line) is lowered (becomes *soft*) until it reaches zero at the critical temperature (vertical dotted line). Upon further cooling, the phonon frequency in the ferroelectric phase rises again, it *hardens*.

The textbook *Physics of ferroelectrics: a modern perspective* serves as an excellent starting point for a more detailed look at the vast topic of ferroelectrics [15].

In the context of this thesis, ferroelectricity plays a central role. Later in this chapter, we introduce the ferroelectric material $BaTiO_3$ in more detail (sec. 1.2.1). Chapter 3 then covers the contraindicated properties of ferroelectricity and metallicity in BTO. Additionally, chapters 4 and 5 concern the incipient ferroelectric materials $SrTiO_3$ (sec. 1.2.2) and $KTaO_3$ (sec. 1.2.3). To better understand the peculiar quantum paraelectric state of these materials, a short overview of quantum phase transitions follows next.

1.1.2 Quantum phase transitions

Quantum phase transitions are phase transitions that occur at zero temperature, so that the order parameter governing the transition is *not* temperature, but e.g. pressure or strain. The crossing of the quantum critical point at zero kelvin is driven by quantum fluctuations, whereas in a classical phase transition which is thermally driven, the system freezes in place below the critical temperature and has no thermal fluctuations anymore at zero kelvin. The quantum critical point itself, as it only exists at exactly zero kelvin, is more a theoretical topic, but the quantum effects "reach out" to finite temperatures above the quantum critical point into a regime called *quantum critical* (see figure 1.4), where many unusual phenomena persist.

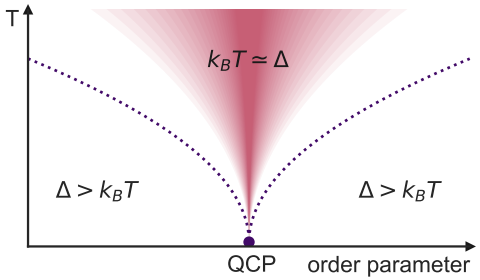

FIGURE 1.4: Sketch of a quantum critical phase diagram. The quantum critical point sits on the horizontal axis at zero temperature, with two different regimes extending above: In the regimes left and right of the point, and below a certain temperature, the quantum fluctuations dominate the behavior, as their energy, Δ, is larger than the thermal energy, $k_B T$, and classical equations of motion can be used to describe the system. The region in the center, indicated by the colored fan, is called the *quantum critical* region, where the thermal fluctuations are of the same order of magnitude as the quantum ones and the classical description does not work anymore. The dashed lines between these two regions indicate the crossover from one region to the other. (Adapted from fig. 1.3 in ref. [16].)

These phenomena arise because quantum fluctuations and thermal effects are of the same order of magnitude and interact, leading to unexpected effects such as quantum paraelectricity [17, 18], multiferroic

quantum criticality [19], and non-Fermi liquid behavior which is a precursor of cuprate superconductivity [20]. The book *Quantum Phase Transitions* covers the basics and more, extending far beyond what is relevant for this work [16].

Experimentally and computationally, this region is challenging to probe and analyze. Chapter 4 covers our work on trying to make the nature of the quantum fluctuations more tangible for the quantum paraelectrics STO and KTO.

1.1.3 Superconductivity

Superconductivity is a property in which an electrical current flows without resistance, and magnetic fields are expelled from the material, below a critical temperature T_c and a critical external magnetic field H_c. Figure 1.5 shows the typical evolution of the electrical resistance with temperature, with the clear drop to zero resistivity below the critical temperature.

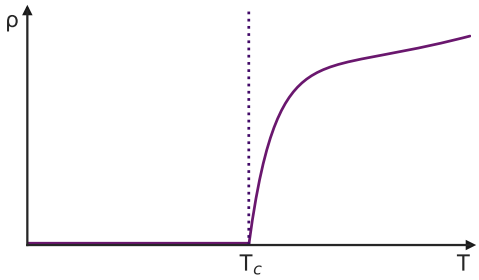

FIGURE 1.5: Sketch of the resistivity ρ versus temperature T of a superconducting material. Above the critical temperature, indicated by the dashed vertical line, the resistivity usually shows metallic behavior and rises with temperature. Below the critical temperature, the resistivity is exactly zero and an electric current will flow without dissipation in a closed circuit.

First observed in 1911 in mercury [21], a basic understanding of conventional superconductivity took until the 1950s with the phenomenological Ginzburg-Landau theory [22] and the microscopic Bardeen–

Cooper–Schrieffer (BCS) theory [23]. The conventional superconducting transition was shown to be a second-order phase transition, and the superconducting current to be a superfluid made up of Cooper pairs which interact mediated by lattice vibrations [24].

The discovery of the isotope effect, in which the BCS superconducting critical temperature is lowered upon substitution with a heavier isotope, played a key role in identifying the coupling between electrons [25–28]. The so-called Eliashberg theory, published 3 years later, describes the role of phonons in providing the interactive attraction, called electron-phonon coupling (EPC) [29, 30]. Shortly after, the first oxide-based *unconventional* superconducting material was discovered in 1964 by Schooley *et al.* [31], namely $SrTiO_3$, a material in which both BCS and Eliashberg theory are not directly applicable anymore, mainly due to its low carrier density [32].

Despite a lot of experimental and theoretical research going into understanding unconventional superconductivity, especially after the discovery of high-temperature superconductivity in 1975 [33] and the discovery of cuprate superconductors in 1986 [34], its origin in STO and other materials remains largely unexplained until today. An excellent entry into the topic of superconductivity is the book by Schrieffer [28].

The possible link between superconductivity and quantum paraelectricity, as first suggested for $SrTiO_3$ by Edge et al. in 2015 [35], was a motivation for this research project, and provides the link between the three main parts of thesis. While motivated by this initial idea, we extended into "normal" ferroelectricity in BTO to see if free carriers and polarization can coexist (see chapter 3), created a method to better understand quantum paraelectricity in STO and KTO and the isotope effect in STO (see chapter 4), and calculated electron-phonon coupling of KTO to find an explanation for the highly anisotropic surface superconductivity (see chapter 5). The following sections cover these three materials and their basic properties in more detail.

1.2 Materials

1.2.1 Ferroelectric $BaTiO_3$

Barium titanate ($BaTiO_3$, BTO) is one of the most well-known prototypical ferroelectric materials. Because of its high dielectric constant it is used in capacitors [36], and its piezoelectric effect is used e.g. in microphones and various sensors [37].

It has the ideal cubic perovskite structure above 393 K, which is paraelectric, and undergoes three phase transitions from cubic to tetragonal, orthorhombic and rhombohedral, with the latter three being ferroelectric [38, 39]. In all four cases the unit cell contains only five atoms, as shown in figure 1.6.

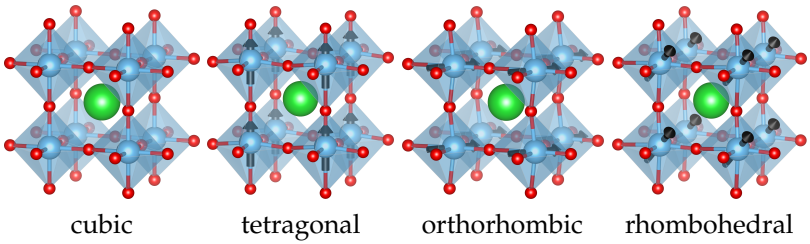

FIGURE 1.6: Visualization of the four different phases of $BaTiO_3$, going from cubic (left) to rhombohedral (right). The polarization directions are (001), (110) and (111), respectively, and indicated by the dark arrows on the titanium ions inside the oxygen octahedra. The overall changes in polarization between the three non-cubic ferroelectric phases are relatively small, but increasing from tetragonal to orthorhombic and rhombohedral [39].

The experimentally measured polarization ranges from 16 $\mu C/cm^{-2}$ to 23 $\mu C/cm^{-2}$, depending on the phase and temperature [39]. To calculate the polarization from first principles, there are essentially two ways: One is the calculation of the so-called *Berry phase* (see refs. [40, 41] for an introduction to the Berry phase within the modern theory of polarization), and the other is by using the relative displacements of the ions and their born effective charges (BEC) (see infobox on page 21).

Computational values of polarization are usually a bit larger than the experimental ones, ranging from 22 $\mu C/cm^{-2}$ to 44 $\mu C/cm^{-2}$ [42, 43]. One reason for this is the fact that DFT calculates properties at zero kelvin, whereas experiments are at finite temperature, and additionally, GGA functionals within DFT can "underbind" and hence over-estimate the lattice constants, leading to larger polarization values.

Ferroelectric materials are usually insulators, as any free charge in the material would screen the polarization. Additionally, free carriers would make it impossible to switch the polarization, as they screen the field used for switching. Nevertheless, such *ferroelectric metals* were proposed theoretically as early as 1965 by Anderson and Blount [44], but due to the seemingly exclusive properties, no such material was found or synthesized until recently, when Shi et al. observed a phase transition to a polar phase in metallic $LiOsO_3$ below 140 K [45]. This observation sparked more research in that direction, including studies of doping of ferroelectric BTO [46–48] and quantum paraelectric STO [49, 50]. A polar metal phase was stabilized in doped BTO thin films [51], and it was shown that ferroelectricity persists even in oxygen-vacancy-doped bulk BTO [52], with both experiments being conducted at room temperature. For an overview of polar metals research, see ref. [53].

This peculiar coexistence of two seemingly contraindicated phases is intriguing, and was motivation for us to conduct a first-principles study to first see if the polarization persists after doping, and if so, understand how the introduction of free carriers influences the polar structure of BTO. Additionally, as doping in DFT can be modeled either by introducing additional carriers compensated by a background charge, or by the explicit chemical substitution of either the A or B ion in supercells, we compare the differences between these two methods and from different doping atoms. The results of this study can be found in chapter 3.

1.2.2 Quantum paraelectric and superconducting $SrTiO_3$

Strontium titanate ($SrTiO_3$, STO) has many different fascinating material properties and is well-known for its soft-mode antiferrodistortive (AFD)

phase transition at 105 K [9] and for being the first oxide superconductor discovered [31].

The well-studied phase transition from cubic to tetragonal at 105 K to 110 K was first observed in 1962 [9], and later determined to involve anti-symmetrical octahedral rotations around the [001] axis [54–58]. Just two years later, in 1964, superconductivity up to 250 mK was discovered in reduced STO, making it the first unconventional superconductor, with superconductivity being observed at unusually low carrier densities down to $7 \times 10^{17}\,\mathrm{cm}^{-3}$ [31]. The first mention of a "superconducting dome" in STO was made in 1968 [59], and a link to the ferroelectric soft mode made in the year after [60].

This ferroelectric soft mode is linked to the so-called *quantum paraelectric* (QPE) state, which can be characterized experimentally by an upturn of the dielectric constant, which reaches values of up to 18 000 [61], even higher than in ferroelectric BTO, upon cooling in the paraelectric phase. Theories for this intriguingly high dielectric constant at low temperatures were published in the 1960s [62, 63], in parallel to the discovery of superconductivity, with long discussions following about if and when STO becomes ferroelectric [64–66]. In 1979, Müller et al. explained the measured high dielectric constant with a quantum-mechanical model and coined the term *quantum paraelectric* for materials with a "quantum-mechanical stabilization of the paraelectric phase" [18].

This QPE state is a quantum phase stabilized by quantum fluctuations, which are independent of temperature (see also section 1.1.2 on quantum phase transitions), and give rise to many of the phenomena observed in STO. One of them could be superconductivity, which was proposed in 2015 by Edge et al. [35], linking the quantum paraelectric state to superconductivity and proposing a large isotope effect in the opposite direction to that of BCS superconductors. Several subsequent experiments confirmed the proposed unusual increase of T_c with heavier-isotope substitution, and led to a surge of research in this area in recent years.

Other theories for superconductivity in STO have been proposed recently, many of which also incorporate the soft ferroelectric phonon mode, and an extensive review can be found in ref. [67].

The main challenge in describing superconductivity in STO is that fact the Fermi energy ϵ_F is much lower than the Debye frequency ω_D ($\epsilon_F < \omega_D$), which stands in contrast to the Migdal criterion ($\epsilon_F > \omega_D$), which is one of the main assumption of the Migdal-Eliashberg theory [68], which therefore can not be applied to STO [67]. A second challenge follows from the low density of states at the Fermi energy because of the low carrier concentration, which makes the estimated BCS T_c essentially zero, if BCS theory were applicable at all.

In the model by Edge et al. from 2015, the ferroelectric soft mode fluctuations provide the coupling for the superconducting Cooper pairs. At low doping values, the lower carrier density limits this strength, leading to an increase of T_c with doping, until above a certain doping value, the increased distance to the quantum critical point reduces T_c again, resulting in the typical superconducting dome observed in STO [35]. The main validation for this model came just one year later, when the suggested *increase* of T_c with O^{18} was measured [69], instead of the usual *decrease* of T_c with heavier isotope substitution in BCS superconductors [27].

Looking into this interplay of phases at low temperatures, we found no intuitive picture for describing the quantum paraelectric state, and contradictions in the literature concerning the tunneling nature of the atoms. We thus developed a computationally affordable method to model this quantum paraelectric state at zero kelvin, including explicitly the quantum-mechanical treatment of the ions, which I present in chapter 4. There, we analyze at the isotope effect and compare its influence with that of geometric changes of the unit cell, and also propose a description for the nature of the tunneling ions.

1.2.3 Quantum paraelectric and superconducting $KTaO_3$

Potassium tantalate ($KTaO_3$, KTO) shares many properties and phenomena with STO, especially the closeness to a ferroelectric phase transition and, discovered much more recently, superconductivity up to 2 K on surfaces and interfaces [70–74]. It has an upturn of the dielectric constant at low temperatures making it a quantum paraelectric, similar to STO, but less pronounced in absolute values [75, 76].

Its cubic structure without phase transition throughout the whole temperature range [77] makes KTO an ideal material for a computational study (see figure 1.1 for the cubic structure). Additionally, its heavy tantalum ion replacing the titanium of STO and BTO, leads to a large spin-orbit coupling [78–80] and Rashba effect, both of which are especially important for spintronic devices [81] and possibly for the aforementioned interfacial superconductivity. KTO is also used as a thermoelectric material with relatively high figure of merit ZT [82, 83].

Around ten years ago, the first measurements of superconductivity up to 50 mK on KTO surfaces were made using ionic liquid gating [70, 71]. Very recently, several independent measurements of superconductivity up to 2 K on surfaces and interfaces of KTO [72–74] have sparked research interest into the possible origin of this highly anisotropic superconductivity [84, 85]. While most assumptions and theories valid for STO, as presented e.g. in ref. [67], should also be applicable to KTO, the two-dimensional geometry changes certain things.

The most successful theory to date describing the anisotropy is based on local symmetry-breaking on the surface [84]. An out-of-plane polar displacement of the Ta and O ions allows linear coupling to electrons within the three tantalum t_{2g} orbitals, which would approach zero otherwise. Because this polar displacement is highly dependent on the actual surface orientation, the highest inter-orbital hopping of electrons is possible on (111)-terminated surfaces, followed by (110)-terminated ones. In contrast to that, the (001)-terminated surfaces do not allow hopping due to their symmetry, which is in perfect agreement with the experimentally measured superconducting critical temperatures in KTO [72–74].

A recent theory for STO proposed that, because the superconducting gap follows the traditional BCS theory [85], BCS theories could still be relevant for STO and KTO. This, and the fact that electron-phonon coupling is one of the central elements of the pairing between electrons, motivated us to calculate the mode-resolved electron-phonon coupling in KTO. We believe that the insights gained from these results are highly relevant for the scientific community and present them in chapter 5.

Additionally, there is no simple model for the quantum paraelectric state in KTO at zero Kelvin, similar to STO, which is why KTO is another material covered by our publication presented in chapter 4.

1.3 Structure of this thesis

The remainder of this thesis is as follows: In the next chapter, we describe the computational methods used to study the materials and phenomena.

Each of the following three chapters contains either a peer-reviewed or preprint article as main part, enclosed by a more general introduction to the topic, computational details, additional results and a brief summary in the context of the whole thesis.

First, in chapter 3, we show that polarization can be preserved even when insulators are doped and made metallic, using $BaTiO_3$ as model material, with a focus on the different atomic contributions (published as *J. Mater. Chem. C* 9, 8640–8649 (2021) [86]).

Next, in chapter 4, we focus on quantum paraelectricity and present a simple model including the quantum-mechanical treatment of the ions to better understand and describe this phase in $SrTiO_3$ and $KTaO_3$ and the peculiar isotope effects in $SrTiO_3$ (published as *Phys. Rev. Research* 4, 033020 (2022) [87]).

Then, in chapter 5, we compute the mode-resolved electron-phonon coupling strength λ in $KTaO_3$ along different reciprocal directions in search of an explanation for the highly anisotropic superconducting

critical temperatures in (001)-, (110)- and (111)-terminated surfaces (preprint available as *arXiv* 2210.14113 (2022) [88]).

Finally, chapter 6 contains a short summary and gives an outlook on open questions and potential future research directions.

2

Methods

2.1 Density functional theory

All results in this work are computationally obtained properties of solid-state systems. To calculate the electronic properties of materials, one has to in principle solve the many-body Schrödinger equation, which in its most general form is given as

$$H\Psi(\vec{R},\vec{r}) = E\Psi(\vec{R},\vec{r}) \quad , \tag{2.1}$$

with an arbitrary number of nuclei at positions $\vec{R_i}$ and electrons at positions $\vec{r_i}$. The Hamiltonian can be split into several contributions according to

$$H = T_n + T_e + U_{nn} + U_{ne} + U_{ee} \quad , \tag{2.2}$$

with T being the kinetic energy of the nuclei (T_n) and electrons (T_e), respectively, and U representing the Coulomb interaction between nuclei (U_{nn}), electrons (U_{ee}) and nuclei and electrons (U_{ne}). Unfortunately, the solution of this equation for any system, apart from the most simple ones like a single hydrogen atom, quickly becomes impossible and simplifications are necessary. In this section, I briefly describe the main simplifications and approximations needed to be able obtain the material properties of interest.

Born-Oppenheimer approximation As the timescale of nuclear motion is much slower than that of electron motion, we can approximate the nuclei as static, resulting in an external potential V_{ext} including all contributions from the nuclei, the so-called *Born-Oppenheimer approximation* [89]. This simplifies our problem and leaves only the electronic contributions to the total energy

$$E = V_{ext} + T_e + U_{ee} \quad , \tag{2.3}$$

with the external potential computed from the position of the fixed nuclei and possible external fields, and the kinetic energy of the electrons being defined as

$$T_e = -\frac{\hbar^2}{2}\sum_i \frac{\nabla_i^2}{m_i} \quad . \tag{2.4}$$

Hohenberg-Kohn theorem

An important discovery was made by Hohenberg and Kohn, when they found that the ground-state electron density $n_0(\vec{r})$ is uniquely defined, that $n(\vec{r})$ defines the total energy through a unique functional, and that this total energy is minimized by the ground-state density ($E_0 = E[n_0]$) [90]. Further, one can compute any ground-state observable from the electron density alone, not only the ground-state energy. This makes computations much easier, as the density depends on only three spatial coordinates, in contrast to the wavefunctions of the whole system.

Kohn-Sham equations To make the calculation of the electron-electron interaction U_{ee} possible, Kohn and Sham mapped the full interacting system to a non-interacting system with an effective potential

$$V_{eff} = V_{ext} + V_H + V_{xc} \quad , \tag{2.5}$$

with the same ground-state density $n(\vec{r})$ as the original system [91]. The effective potential contains the external potential from the nuclei and possible external fields, V_{ext}, and the electron-electron interaction U_{ee}, split into two parts. The first part is the classical Coulomb interaction (Hartree potential, V_H), and the second part, called the *exchange-correlation* potential V_{xc}, contains all quantum mechanical many-body effects going beyond this classical interaction. The Schrödinger equation with this Kohn-Sham Hamiltonian is then

$$[T_e + V_{eff}]\,\Psi_i(\vec{r}) = E_{KS,i}\Psi_i(\vec{r}) \quad . \tag{2.6}$$

Theoretically, one can now start from an initial guess of the electron density $n^{(0)}(\vec{r})$, calculate the effective potential $V_{eff}^{(0)}$ in eq. 2.5 using this

density, solve the Kohn-Sham equation 2.6 and obtain the wavefunctions $\Psi_i^{(1)}(\vec{r})$ of the system, which in turn can be used to calculate the density $n^{(1)}(\vec{r})$ again after one iteration. This scheme can be repeated iteratively in a self-consistent fashion, and terminated if the difference between new and previous densities is below a certain threshold.

Up to now, no approximations were made, and despite not describing the exact same system as the original one, minimizing the total energy of the Kohn-Sham Schrödinger equation will result in exactly the same electron density $n(\vec{r})$ as that of the original system.

The only part missing now is the exchange-correlation potential, for which no exact description is known. Therefore, approximations for the exchange-correlation potential are necessary in practice and used in the form of different *functionals*. Additionally, a widely-used approximation in practical DFT are pseudo potentials, which are used to remove core electrons from the density and treat them as part of the external potential. This accelerates calculations significantly because there are fewer electrons and thus degrees of freedom in the system.

Exchange-correlation potentials

The exchange correlation potential V_{xc} is the main challenge remaining, and several different approaches have been made to tackle this, resulting in a variety of *functionals* to approximate this exchange correlation potential. In general, V_{xc} is calculated from the exchange correlation energy E_{xc}

$$V_{xc}[n] = \frac{\delta E_{xc}[n]}{\delta n} \quad . \tag{2.7}$$

The first and simplest approximation for the exchange correlation energy E_{xc} assumes that it corresponds to the one of a free electron gas [92] at any point $\vec{r}$. This approximation is called the *local density approximation* (LDA) [93] and works surprisingly well, despite its conceptual simplicity. It usually "overbinds" atoms, however, resulting in e.g. too small lattice constants.

To counter this issue, one can include the gradient of the exchange correlation energy E_{xc}, leading to the *generalized gradient approximation* (GGA). There exist several methods to include this gradient, and thus there are many different GGA functionals. One of the most widely used is the one by Perdew, Burke and Ernzerhof (PBE) [94], which, like most GGAs, softens the bonds, most of the time too much in the case of solids. To improve on this "underbinding", a revised parametrization especially for solids (PBEsol) was introduced in 2008 [95].

Throughout this work, we use a selection of all three functionals, depending on the properties we want to describe, as every functional has its unique advantages.

Pseudo potentials

A popular approximation, though not necessary for DFT to work, is the use of pseudo potentials. The idea is that the chemical binding of atoms is dominated by their valence (outer) electrons, while the core (inner) electrons remain mostly unchanged. These core electrons can thus be approximated by merging them with the external potential of the atoms, which we now call V_{ext}^{PP}. The Hartree and exchange correlation terms of the effective potential in eq. 2.5 then have to be evaluated only for the valence electrons, which lowers the computational cost significantly. Different methods for constructing such pseudo potentials are known and available, all with their own advantages and suitability for certain systems or properties, and also depending on the DFT software used [96].

We note in each chapter which pseudo potentials we use, most of the time these are the GBRV ones when using Quantum Espresso, named after their creators Garrity, Bennett, Rabe and Vanderbilt [97, 98].

2.2 Density functional perturbation theory

This section closely follows the PhD thesis of Andrea Urru [99] and the review by Baroni et al. [100], both of which cover this topic in much more detail.

In DFT, the lattice is assumed to be static, which is the core of the Born-Oppenheimer approximation. This means that the electrons are decoupled from the dynamical properties of the nuclei and treated separately by DFT.

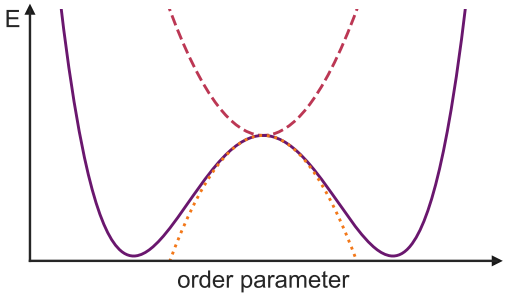

FIGURE 2.1: Schematic energy potential within the harmonic approximation, as used in density functional perturbation theory (DFPT). The dashed line resembles a harmonic potential with real frequency, where any displacement from the central position results in a restoring force towards the center (e.g. in a paraelectric). The dotted line resembles a harmonic potential with imaginary frequency, where any displacement from the central position results in a deviating force away from center (e.g. in a ferroelectric). The solid line resembles a quartic potential of e.g. a ferroelectric, where both the top of the barrier and the bottom of each well can be approximated using a harmonic potential individually, but the overall potential shape goes beyond the harmonic approximation.

One can now model the motion of the nuclei with a harmonic approximation, using a Taylor expansion around their equilibrium position up to second order (see figure 2.1 for a visualization in the absence of a linear field). The equilibrium position is given by the constraint that

the forces acting on the nuclei are zero. These forces can be derived directly from the first derivative of the energy according to

$$F_I = \frac{\partial E(\vec{R})}{\partial \vec{R_I}} \quad , \tag{2.8}$$

which is defined by the electron density, as calculated by DFT, and the electron-nucleus interaction, which depends only on the position of electrons and nuclei.

The vibrational frequencies (phonon frequencies) ω can be calculated from the second derivative of the energy according to

$$\det \left| \frac{1}{\sqrt{M_I M_J}} \frac{\partial^2 E(\vec{R})}{\partial \vec{R_I} \partial \vec{R_J}} - \omega^2 \right| = 0 \quad . \tag{2.9}$$

The individual elements

$$\frac{\partial^2 E(\vec{R})}{\partial \vec{R_I} \partial \vec{R_J}}$$

are called *interatomic force constants*.

To obtain a system's ground-state geometry and phonon frequencies, one has to calculate both first and second derivatives of the Born-Oppenheimer energy surface. The *Hellmann-Feynman theorem* states that the derivative of the total energy E, defined by a Hamiltonian H, with respect to a parameter, is given by the expectation value of the derivative of H with respect to this parameter [101, 102]. Using this theorem, the calculation of forces depends directly on the electron density $n(\vec{r})$, and the calculation of the interatomic force constants requires the linear response of the electron density $n(\vec{r})$ to a lattice distortion.

With density functional perturbation theory (DFPT), this linear response of the electron density can be calculated self-consistently and directly from a perturbation of the Kohn-Sham orbitals. Computing the response to a single perturbation is of similar computational cost as the computation of the unperturbed ground-state density, and responses to perturbations are decoupled. This makes it possible to calculate phonon

frequencies at relatively low cost and at any arbitrary wavevector $\vec{q}$ without using supercells of corresponding size.

As we are dealing with (incipient) ferroelectrics, and thus (almost) polar systems in this thesis, we note that polar insulators need a special treatment within DFPT. The long-range Coulomb interaction, present in polar materials, induces an electric field that splits optical modes at Γ into longitudinal optical (LO) modes, which are parallel to the electric field, and transverse optical (TO) modes, which are perpendicular. This splitting is proportional to the Born-effective charges (BEC) of the ions (see infobox) and inversely proportional to the macroscopic dielectric constant. The TO modes are equivalent to the normal phonon modes without this splitting, but the LO modes are shifted to higher energies. Computationally, the interatomic force constants are split into an analytical, short-range, part, and a non-analytical, long-range, part, which are treated differently during the different computational steps.

Born effective charges

Born effective charges (BEC),

$$Z^*_{\alpha\beta} = \frac{\Omega}{e}\frac{\partial P_\alpha}{\partial u_\beta} \quad , \tag{2.10}$$

describe the dimensionless effective charge of an ion by the change of polarization P_α in cartesian direction α, caused by a displacement u_β in cartesian direction β. Here, e is the electronic charge and Ω the unit cell volume [15].
They can be the same as the formal charges of the ion (e.g. -2 for a O^{2-}), e.g. in non-polar and ionic compounds, but especially in ferroelectric materials, they are usually much larger than the formal ion charges. One example is BTO, where the BEC of Ba and Ti are $+2.7$, $+7.25$ and the BEC of O are -5.7 or -2.1, depending on the orientation of the polarization and displacement, whereas their corresponding formal charges are just $+2$, $+4$ and -2, respectively. While the BEC matrix is symmetric in cubic systems, it is not in lower-symmetry structures.

They can be used to quite accurately calculate the change in "polarization"

$$\delta P = \frac{e}{\Omega} \sum_i Z_i^* d_i \quad , \tag{2.11}$$

based just on ionic displacements d_i, without the need for a full Berry phase calculation, as we show in chapter 3.

Phonon dispersions are usually quite smooth, making it possible to efficiently interpolate frequencies on a fine mesh based on direct calculation at only a few $\vec{q}$ points on a uniform grid in the Brillouin zone. The reciprocal-space interatomic force constants are then transformed into real-space interatomic force constants, using fast Fourier transformation (FFT). Based on these real-space interatomic force constants, phonon frequencies at any arbitrary q-point can be efficiently interpolated. This scheme also works for polar insulators: the non-analytical part is subtracted before the FFT takes place, leaving the analytical short-range part, and then restored again when the interpolation back into k-space is performed [103].

Apart from DFPT, there are other methods to calculate phonon frequencies and dispersions. The most used alternative is probably the so-called *frozen-phonon* method, as e.g. implemented in phonopy [104], which has interfaces with VASP, QE and many other DFT codes. The frozen-phonon approach works in real space and utilizes small displacements of atoms in supercells to obtain the forces required to calculate the interatomic force constants.

The main advantage of this method is that there is no special software required, as it works with bare DFT. Calculating phonons only at Γ requires only one unit cell and is thus very fast using both frozen phonons and DFPT.

The biggest disadvantage of the frozen-phonon method is the poor scaling with the required supercell size as soon as one moves away from Γ: Calculation of phonons at e.g. the R point ([111]) in a cubic Brillouin zone requires a $2 \times 2 \times 2$ supercell with the frozen-phonon method, corresponding to eight times as many atoms in the system.

As usual DFT codes scale cubically with the number of particles, this increases the computational time considerably.

In DFPT, the calculation of phonons at R requires only one computation, without the use of supercells and independent of the position of the q point. Calculations for an arbitrary q point, e.g. $q = (\frac{1}{10}, \frac{1}{10}, \frac{1}{10})$ quickly become impossible with the frozen-phonon approach, while there are no such computational scaling limitations with DFPT.

Nevertheless, its simple implementation makes this approach appealing, as well as the fact that it can also be combined with DFPT to study anharmonic effects going beyond the second-order harmonic approximation.

2.3 Electron-phonon coupling using Wannier functions

The following part closely follows the structure and notation of ref. [105], which is the most recent publication describing general electron-phonon coupling in the context of the EPW software package. Recent advances in both computational methods and resources make it now possible to calculate this coupling with useful accuracy and resolution.

The calculation of electron-phonon coupling needs both electronic states and phonon eigenvectors on a fine mesh in the first Brillouin zone. Electronic states can be calculated using DFT (see sec. 2.1), and phonons can be calculated using DFPT (see sec. 2.2).

If we now take an electronic wavefunction of band m and wavevector $\vec{k}$ and a phonon with wavevector $\vec{q}$ and branch ν, we can write the general electron-phonon matrix element as

$$g_{mn,\nu}(\vec{k}, \vec{q}) = \frac{1}{\sqrt{2\omega_{\vec{q}\nu}}} \langle \psi_{m\vec{k}+\vec{q}} | \partial_{\vec{q}\nu} V | \psi_{n\vec{k}} \rangle \quad . \tag{2.12}$$

This electron-phonon matrix element quantifies the scattering process from one Kohn-Sham state ($\psi_{n\vec{k}}$) to another ($\psi_{m\vec{k}+\vec{q}}$), mediated by the phonon with momentum $\vec{q}$ and frequency $\omega_{\vec{q}\nu}$ (see figure 2.2).

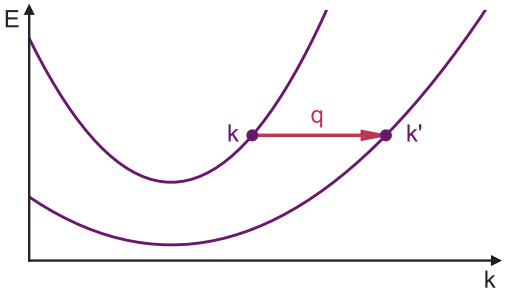

FIGURE 2.2: Visualization of the electron-phonon coupling between electronic states at k and $k' = k + q$, mediated by a phonon with momentum q, corresponding to an electron-phonon matrix element as given in eq. 2.12.

These electron-phonon matrix elements can be used to calculate several important quantities.

First are the phonon linewidths $\Pi''(\omega_{\vec{q}\nu}, T)$, which correspond to the imaginary part of the phonon self energy

$$\begin{aligned}\Pi''(\omega_{\vec{q}\nu}, T) = \; & 2\pi \sum_{mn} \int_{BZ} \frac{d\vec{k}}{\Omega_{BZ}} \left| g_{mn,\nu}(\vec{k}, \vec{q}) \right|^2 \\ & \times \left[f_{n\vec{k}}(T) - f_{m\vec{k}+\vec{q}}(T) \right] \delta(\epsilon_{m\vec{k}+\vec{q}} - \epsilon_{n\vec{k}} - \omega_{\vec{q}\nu}) \quad ,\end{aligned} \tag{2.13}$$

where the sum is taken over all electronic states m and n (with energies $\epsilon_{m\vec{k}+\vec{q}}$ and $\epsilon_{n\vec{k}}$), the integral is taken over the whole Brillouin zone (BZ) with volume Ω_{BZ}, $f_{n\vec{k}}(T)$ is the electronic occupation at wavevector $\vec{k}$ and band n, and δ is the Dirac delta function.

Second are the mode-resolved electron–phonon coupling strengths, $\lambda_{\vec{q}\nu}$, given by

$$\begin{aligned}\lambda_{\vec{q}\nu} = \; & \frac{1}{N(\epsilon_F)\omega_{\vec{q}\nu}} \sum_{mn} \int_{BZ} \frac{d\vec{k}}{\Omega_{BZ}} \\ & \times \left| g_{mn,\nu}(\vec{k}, \vec{q}) \right|^2 \delta(\epsilon_{n\vec{k}} - \epsilon_F) \delta(\epsilon_{m\vec{k}+\vec{q}} - \epsilon_F) \quad ,\end{aligned} \tag{2.14}$$

where $N(\epsilon_F)$ is the density of states at the Fermi energy ϵ_F. These are a key quantity in chapter 5.

Finally, summing over all phonons results in the total electron–phonon coupling strength

$$\lambda = \sum_{\vec{q}\nu} w_{\vec{q}\nu} \lambda_{\vec{q}\nu} \quad , \tag{2.15}$$

where $w_{\vec{q}\nu}$ is the weight of $\lambda_{\vec{q}\nu}$ in the first Brillouin zone.

To obtain an accurate representation of the physics of the system, one needs a large number of both electronic states and phonons (up to millions), making it difficult to calculate using traditional DFT and DFPT. The *Electron-Phonon coupling using Wannier functions* (EPW) method alleviates this problem. EPW uses maximally-localized Wannier functions (see infobox) to transform the electron part into real space, and uses a similar approach for the phonon part, to allow for a much denser sampling of the Brillouin zone. It relies on the fact that the electron-phonon matrix element is highly localized in real space in both electron and phonon variables, which means that one needs to know fewer elements in real space to successfully interpolate on a denser mesh in reciprocal space, similarly to the interpolation scheme in DFPT.

Wannier functions

Electronic states of solids are usually described in reciprocal space, or *Bloch* space. One can transform these Bloch orbitals into real space representations, called *Wannier* representations after Gregory Wannier [106]. Many different ways of performing this transformation into different real space representations are known, with one very useful and widely used one called *maximally localized Wanner functions* [107], which are the solid-state physics equivalent to chemistry's molecular orbitals. They are constructed by minimizing their so-called spread in real space, resulting in a complete set of orthogonal functions representing the electronic charge distribution, and are very useful in understanding bonding, defects, polarization, magnetization and many other properties in solids. The main use they provide in our case is as an intermediary in the calculation of electron-phonon matrix elements, as described in section 2.3.
An extensive review of this topic can be found in ref. [108].

The typical cycle of an EPW calculation starts with the calculation of both electronic states and phonon frequencies throughout the whole Brillouin zone on a uniformly spaced *coarse mesh* including Γ. These electronic and phonon states are then Fourier transformed from their Bloch representation into their Wannier representation. The electron-phonon matrix elements are transformed into real space as well, using the same transformation matrices. Now a much denser *fine mesh* can be used as a target mesh to calculate electronic and phonon states in reciprocal space, using an inverse Fourier transform based on the real-space quantities. As the target mesh does not have to be commensurate or equally spaced, random meshes can be used as well; these have been shown to converge faster, which means one can use fewer points on the fine mesh compared to a regular mesh [105].

For the exact mathematical formulation and details on the implementation of the calculation of electron-phonon coupling in EPW, I refer the interested reader to refs. [105, 109, 110].

2.4 Software and technical details

The methods mentioned in this chapter are implemented in many different computer codes. This section serves as a short overview of the actual programs used in this work.

DFT, as the cornerstone of all other methods, has a plethora of implementations, both in chemistry and physics (a comprehensive and up-to-date list can be found on Wikipedia [111]). Two of the most-used software packages in solid-state physics are the Vienna Ab initio Simulation Package (VASP) [112–114] and Quantum ESPRESSO (QE) [115–117].

VASP is commercial software and a license has to be bought to use it. Its main advantages are ease-of-use, computational speed, and widespread use in the solid-state community. Documentation is available in the form of an online Wiki [118], and despite being commercially licensed, the source code is available for inspection and compilation. Because of its widespread use, certain post-processing software packages are

only interfaced with VASP, e.g. the LOBSTER package [119, 120] to calculate Crystal orbital Hamilton populations (COHP) [121], which we use extensively in chapter 3. (As a note, LOBSTER has been extended recently [120] to support not only VASP, but also QE and ABINIT [122, 123].) Additionally, VASP comes packaged with an extensive library of highly-optimized pseudo potentials and functionals.

Quantum ESPRESSO is a suite of individual programs that can perform many different types of calculations related to computational chemistry and physics. It is open-source software, available free of charge and development takes place on Gitlab [124]. Documentation has been improved immensely in the past few years, an overview is on the project homepage at [125]. Its main advantage, at least for our purposes, is the implementation of both DFPT and EPW directly within the software package, on top of the DFT capabilities. In contrast to VASP, QE does not come with pseudo potentials, making it necessary to either compile them yourself, or use precompiled ones. Luckily, many variants are readily available and well-tested, including different functionals, with a good starting point provided here [126].

Finally, I want to mention the python programming language [127], which has been an essential part of this work, not only in the pre- and post-processing of data, but also in the scientific part. The libraries *jupyterlab* [128] as the interface to everything else, *numpy* [129] and *scipy* [130] for the mathematical part, and *pandas* [131, 132] and *matplotlib* [133] for data management and visualization were an integral part as well.

3

Coexistence of polarization and metallicity in $BaTiO_3$

3.1 Preface

In this chapter, we take a close look at the possible coexistence of ferroelectricity and metallicity in barium titanate (BTO). Ferroelectricity involves the polar displacement of the atoms in the crystal, which is usually screened by the free carriers present in metals, thus these two properties are contraindicated. Nevertheless, it was shown theoretically in 1965 [44] that both phenomena can coexist, up to to certain doping limits. Recently it was also shown experimentally, first in $LiOsO_3$ [45], then in BTO [47, 48, 52], that "polar metals" do exist.

$BaTiO_3$ is an ideal material to study these two contraindicated properties as it is a prototypical ferroelectric and there are known substitutions to make BTO metallic by replacing either the barium or the titanium ion. A quick note on polarons [134, 135] is appropriate here, as they have been proposed as the conduction mechanism in La- and Nb-doped BTO [136–138]. Polarons are quasi particles arising from the interaction of the lattice with a charge in a dielectric material, creating essentially a "polar phonon cloud" around the charge, as first described by Landau in 1933 [139], with the term "polaron" coined by Pekar [140–142]. Polarons are in general important for electron mobility in semiconductors, as they can strongly modify the effective mass of the electrons [143], a fact that makes them also important e.g. in the optimization of thermoelectric materials [144].

Three main points motivated us to study these phenomena in $BaTiO_3$. The first is the fact that the coexistence of two material properties that are in principle mutually exclusive is a fascinating thing, since novel physical phenomena often result from such combinations, such as the flourishing research field of multiferroics initiated by an article in 2000 [145]. The second relates to the other topics presented in the first chapter, namely superconductivity and quantum paraelectricity. If these two phenomena should be linked, then superconductivity and polarization fluctuations have to coexist, making it only logical to first study the "simpler" phenomena of conventional conductivity and classical ferroelectricity. The third and final reason is more of a technical nature. Previous DFT studies of polarization in doped BTO have either used fully-relaxed unit cells with the background-charge doping method [146], a practice later shown to be ill-defined [147], or cover only a few of the experimentally feasible dopants [148]. We therefore want to not only provide methodically correct results for the background-charge doping, but also to give a full overview of a larger selection of dopants and compare the results of both methods.

Before presenting our peer-reviewed work and results, another quick note on the meaning and computation of Crystal Orbital Hamiltonian Populations (COHP). COHP indicate if a certain part of the DOS is bonding, anti-bonding or non-bonding, and are obtained as the product of the electron density matrix with the projected Hamiltonian matrix, which consists of the elements $H_{mn} = \langle \Phi_m | \hat{H}^{PW} | \Phi_n \rangle$, with Φ_m being localized orbitals, and $\hat{H}^{PW}$ being the plane-wave Hamiltonian [121, 149, 150]. Integrated COHP values (ICOHP) of the occupied states are a measure for the strength of a certain bond. COHP and ICOHP are usually given and plotted as negative values to make them directly comparable to e.g. DOS or COOP plots, because weighting the DOS with the Hamiltonian results in energy-saving bonds having negative values. To calculate both COHP and ICOHP, we use a software called LOBSTER [119, 120, 150], which efficiently implements these calculations based on the results of plane-wave DFT calculations. A special way of projecting the eigenstates onto local orbitals improves the number of retained electrons during this step significantly compared to the usual projection implemented in DFT codes [149–152]. This results not only

in the correct representation of the total and projected DOS, but also in accurate COHP and ICOHP values based on ab-initio calculations.

Explanatory Remarks

The following section is published as:

Veronica F. Michel, Tobias Esswein and Nicola A. Spaldin. Interplay between Ferroelectricity and Metallicity in $BaTiO_3$ *J. Mater. Chem. C* 9, 8640–8649 (2021). DOI: 10.1039/D1TC01868J.

—

3.2 Abstract

We explore the interplay between ferroelectricity and metallicity, which are generally considered to be contra-indicated properties, in the prototypical ferroelectric barium titanate, $BaTiO_3$. Using first-principles density functional theory, we calculate the effects of electron and hole doping, first by introducing a hypothetical background charge, and second through the introduction of explicit impurities (La, Nb and V for electron doping, and K, Al and Sc for hole doping). We find that, apart from a surprising increase in polarization at small hole concentrations, both charge-carrier types decrease the tendency towards ferroelectricity, with the strength of the polarization suppression, which is different for electrons and holes, determined by the detailed structure of the conduction and valence bands. Doping with impurity atoms increases the complexity and allows us to identify three factors that influence the ferroelectricity: structural effects arising largely from the size of the impurity ion, electronic effects from the introduction of charge carriers, and changes in unit-cell volume and shape. A competing balance between these contributions can result in an increase or decrease in ferroelectricity with doping.

3.3 Introduction

Ferroelectricity and metallicity are generally considered to be contra-indicated properties since the metallic charge carriers screen the long-range interactions that favor the ferroelectric structural distortion [153]. These two properties can nevertheless be combined in systems where the interaction between the itinerant electrons and the polar distortion is weak, as shown theoretically by Anderson and Blount in 1965. Such materials were called "ferroelectric metals" [44], although the term is somewhat ambiguous: Ferroelectricity is in fact defined for materials that show a spontaneous polarization that is *switchable by an applied electric field*; in the presence of metallic charge carriers however, the electric field is screened by the itinerant electrons and induces an electric current rather than a polarization switch [52, 146], so that a ferroelectric can formally not be metallic. A more rigorous term is perhaps polar metal, which is a material, such as $LiOsO_3$ [45], that has a polar crystal class combined with a non-zero density of states at the Fermi level [154]. In addition to their fundamental interest, polar metals are promising for a range of applications. Some of them are reported to show giant optical responses, and could thus be used in optoelectronic devices [155]. They are also good candidates for the design of materials with tunable metal-insulator transitions [156]. Furthermore, they are of relevance for polar superconductors, which have the potential to show unconventional superconducting states [157].

Barium titanate ($BaTiO_3$) is the prototypical ferroelectric material. It has the ideal ABO_3 perovskite structure at high temperatures, corresponding to a centrosymmetric cube with formally Ba^{2+} cations at the corners, Ti^{4+} at the center and O^{2-} at the face centers [39]. Upon lowering the temperature, three phase transitions occur: At 393 K a phase transition from a paraelectric cubic to a ferroelectric tetragonal phase is observed, followed by a transition to a ferroelectric orthorhombic phase at 278 K and to a ferroelectric rhombohedral phase, with polarization along a <111> direction, at 183 K [39]. Multiple efforts have been made to make $BaTiO_3$ metallic. In 2008, an insulator-metal transition was reported in $BaTiO_3$ doped with oxygen vacancies ($BaTiO_{3-\delta}$) [47],

which was later shown to retain its ferroelectric structural distortion up to an electron concentration $n \sim 1.9 \cdot 10^{21}$ cm^{-3} [48]. This work was challenged by Jeong *et al.*, who reported, based on neutron diffraction studies, that the ferroelectric ordering and the metallic conduction are not coexisting but rather form two distinct phases in $BaTiO_{3-\delta}$ [158]. Recently, Cordero *et al.* showed through elastic response studies that the ferroelectric transitions persist in metallic $BaTiO_{3-\delta}$ [52], confirming the observations of Ref. [48]. In addition to the introduction of oxygen vacancies, doping in $BaTiO_3$ can be achieved through atomic substitutions, the most common being La^{3+} for Ba^{2+} and Nb^{5+} for Ti^{4+}. Both La- and Nb-doped $BaTiO_3$ show electrical conductivity with a polaronic conduction mechanism [136, 137], with the polaron formation in Nb-doped $BaTiO_3$ believed to come from incoherent B-site off-centering resulting from the random Nb substitution [138].

A few computational investigations on doped $BaTiO_3$ have been reported in the last decade. Wang *et al.* and Iwazaki *et al.* studied metallic $BaTiO_3$ with the background-charge method in 2012 and showed that the ferroelectric displacements are sustained up to 0.11 electrons per unit cell (0.11 e/u.c.) [146, 148]. A drawback of those works is that the calculations were performed with fully relaxed lattice constants, that were shown to be ill-defined with the background-charge method by Bruneval *et al.* in 2015 [147]. The specific effects of doping on chemical bonding and the effect of electron-doping on ferroelectricity and phonon dynamics of $BaTiO_3$ were discussed by Hickox-Young *et al.* and Gu *et al.*, respectively [159, 160].

In 2016, Benedek *et al.* compared the effect of doping in $LiOsO_3$ and $ATiO_3$ perovskites (A = Ba, Sr, Ca) [154]. They showed that the ferroelectricity is suppressed by electron doping in $BaTiO_3$, whereas the non-centrosymmetricity in metallic $LiOsO_3$ and pseudocubic $CaTiO_3$ (with octahedral rotations not allowed) is robust to addition of charge carriers because of the local-bonding nature of the mechanism underlying the off-centering of the ions. Recently, a meta-screening effect was proposed by Zhao *et al.* as the main factor determining the persistence of the polar phase in metallic ferroelectrics [161].

In this work, we explore theoretically the interplay between the contra-indicated properties of ferroelectricity and metallicity in $BaTiO_3$. Using first-principles density functional theory, we address the question of how the ferroelectric B-site off-centering and the likelihood of polarization switchability are affected by metallic charge carriers in $BaTiO_3$. We investigate both electron and hole doping in $BaTiO_3$ first through the background-charge method and subsequently by introducing explicit dopants (La, Nb, V, K, Al and Sc). The dopants are chosen based on experimental feasibility and allow us to separate the effects of dopant size, substitution site as well as second-order Jahn-Teller (SOJT) activity on the polarization.

3.4 Computational Methods

Our calculations are performed using density functional theory (DFT) as implemented in the VASP code [162], with recommended projector-augmented wave potentials and the PBEsol exchange-correlation functional [95]. We include plane waves up to a kinetic energy cutoff of 600 eV. All the used k-point grids are Gamma-centered; details on the sampling meshes are given below. We converge total free energies to 10^{-6} eV and relax atomic positions until all force components converge below 10^{-3} eV/Å.

Crystal structure relaxations are computed for both single unit cells and supercells of $BaTiO_3$. We consider both tetragonal and cubic $BaTiO_3$ single unit cells, corresponding to the room-temperature and high-temperature structures, respectively. We compute the tetragonal $BaTiO_3$ single unit cell structural relaxation as follows: We start with the experimental high-temperature, cubic structure and fully relax its atomic positions and lattice constants with a $6 \times 6 \times 6$ k-points grid, while retaining the cubic symmetry. We subsequently displace the Ti atom by 1% along the c direction and fully relax the atomic positions and the lattice constants with a $12 \times 12 \times 12$ k-point grid, while retaining the tetragonal symmetry. We obtain $a = b = 3.967$ Å and $c = 4.065$ Å; these lattice constants are consistent with experimental literature values for the room-temperature tetragonal phase [163]. We apply the same proce-

dure for the cubic $BaTiO_3$ single unit cell but fix the lattice constants for the second structural relaxation. This keeps the cubic equal lattice constants while allowing for a lower internal symmetry to permit a polar distortion; we refer to this unit cell as pseudocubic throughout the manuscript. We construct the supercells as multiples of the single unit cell in the a, b and c directions and we investigate $2 \times 2 \times 2$ supercells in detail, for which we use a $12 \times 12 \times 12$ k-point grid.

We compute densities of states for $BaTiO_3$ single unit cells with a $24 \times 24 \times 24$ k-point grid. Crystal Orbital Hamiltonian Populations are calculated using the LOBSTER package [119–121, 149, 150, 152]. Our basis sets for COHP calculations are Ba (5s, 5p, 5d, 6s), Ti (3s, 3p, 3d, 4s) and O (2s, 2p). A $16 \times 16 \times 16$ k-point grid is used for these calculations.

We dope the $BaTiO_3$ single unit cells with the background-charge method, in which the number of electrons in the system is manually adapted to the desired doping level and a uniform background charge is added to enforce charge neutrality [118]. Note that the relaxation of lattice constants is not well-defined when using the background-charge method [147], so we keep them fixed. We dope supercells by introducing impurity atoms and allowing for relaxation of the lattice constants.

The presented "polarization" values are calculated using

$$\delta P = \frac{e}{\Omega} \sum_i Z_i^* d_i, \tag{3.1}$$

where e is the electronic charge, Ω the unit cell volume, Z_i^* the Born effective charge (BEC) of atom i, and d_i its relative displacement in the polar direction [41]. The BECs we use are +2.7 for barium, +7.25 for titanium, -5.71 for oxygens that displace parallel to their Ti-O bond direction and -2.15 for oxygens that displace perpendicular to this direction [164]. This procedure yields a polarization value of 38 $\mu C/cm^2$ for undoped $BaTiO_3$, which is close to the value of 34 $\mu C/cm^2$ that we compute using the Berry-phase method with a $24 \times 24 \times 24$ k-point grid (see Figure 3.8), in agreement with literature values [42, 43]. For impurity-doped supercells we set the BEC of the impurity to that of the

atom it substitutes. Note that the polarization of the doped (metallic) systems is ill-defined as it cannot be switched. This quantity does not correspond to a true polarization obtained through a Berry-phase approach [40, 165], is not necessarily switchable and does not require insulating behavior. Its value reflects, rather, the amount of ferroelectric-like structural distortion present in the system. Throughout this paper, we use the term polarization to refer to this effective polarization, and the term ferroelectricity to refer to the non-centrosymmetric structural distortion, without implying polarization switchability.

3.5 Results and Discussion

3.5.1 Introduction of Background Charge into a $BaTiO_3$ Unit Cell

In the first part of our study, we investigate the introduction of doping in $BaTiO_3$ through the background-charge method. This approach allows us to isolate the effect of the electronic charge from other influences such as ion size or change in chemistry associated with the introduction of explicit dopant atoms. Consistent with previous literature results [159], we find the polarization to be reduced by the introduction of charge carriers, and to be more sensitive to the introduction of electrons than holes, due to the different character of the valence and conduction bands.

3.5.1.1 Electron Doping

The calculated polarization of $BaTiO_3$ as a function of charge-carrier concentration is shown in the top panel of Figure 3.1, for both electron and hole doping, and tetragonal and cubic unit cells. We discuss the electron-doped tetragonal system first. On electron addition, the polarization of tetragonal $BaTiO_3$ decreases until it is completely suppressed at 0.2 e/u.c.

The decrease in polarization can be understood through simple electronic structure considerations: In Figure 3.2 we show the calculated

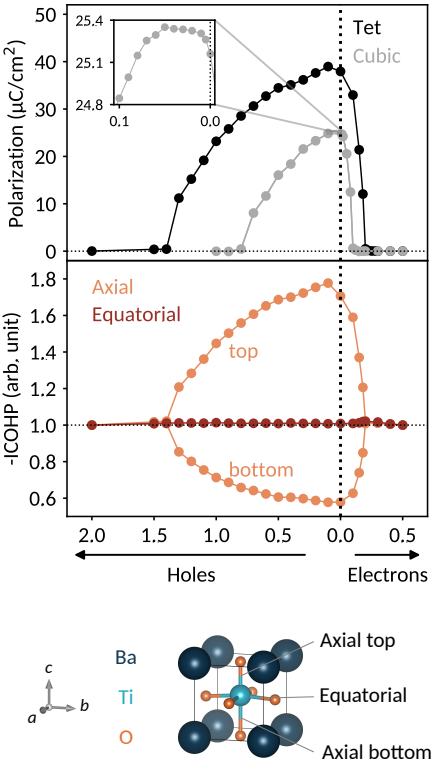

FIGURE 3.1: Top: Polarization as a function of the charge-carrier concentration (electrons on the right, holes on the left) for tetragonal and pseudocubic (abbreviated *tet* and *cubic*) $BaTiO_3$. The pseudocubic symmetry refers to equal lattice constants with an allowed lower internal symmetry so that a polar distortion can occur. We see that the polarization is reduced on electron doping for all concentrations. The addition of holes first increases the polarization before reducing it, with a slower polarization suppression than in the electron doping case. The pseudocubic and tetragonal systems behave in a very similar manner, although the pseudocubic system has lower polarization values for the same charge-carrier concentration. Bottom: Integrated Crystal Orbital Hamiltonian Populations (ICOHPs) for the Ti-O bonds of tetragonal $BaTiO_3$ as a function of the charge-carrier concentration. Three Ti-O bonds are considered and showed in the figure: the Ti-O axial top, axial bottom and equatorial. All ICOHPs are normalized to their value in the centrosymmetric structure. The higher the ICOHP value, the stronger its corresponding bond.

density of states in the region of the Fermi energy for tetragonal $BaTiO_3$ doped with 0.5 e/u.c. We see that the valence band has mainly O 2p character, whereas the conduction band has mainly Ti 3d character and the barium ions have no significant contribution to the DOS in the region of the band gap. Compared to pure $BaTiO_3$ (not shown), the DOS is not strongly affected by the charge carriers, apart from the shift of the Fermi level into the conduction band.

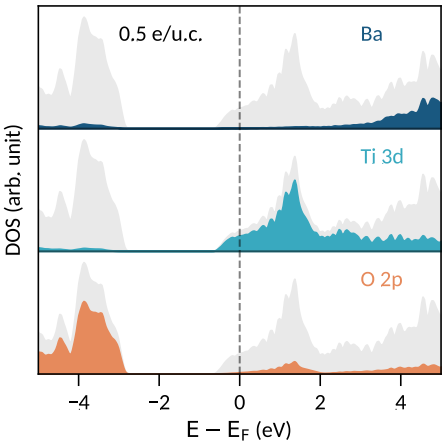

FIGURE 3.2: Density of states for tetragonal $BaTiO_3$ doped with 0.5 e/u.c. The total DOS is shown in gray and the Ba, Ti 3d and O 2p contributions are shown in blue, teal and orange, respectively. The valence band has mainly O 2p character, whereas the conduction band has a high Ti 3d contribution. The Fermi energy, E_F, lies close to the bottom of the conduction band due to the addition of electrons.

The added electrons occupying primarily the Ti 3d energy levels can also be seen clearly in the charge densities of Figure 3.3, where the gray surfaces indicate the added electron density. With increasing electron doping, we see that the charge density on the Ti 3d orbitals progressively increases and as a result the Ti ion deviates further from its formally d^0 electron configuration. Correspondingly, the off-centering described by the SOJT effect, which is favored for d^0 electronic configurations, is reduced [166].

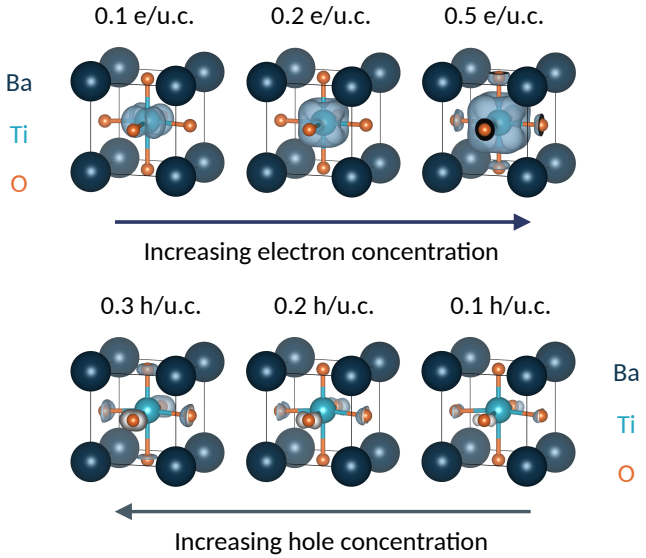

FIGURE 3.3: Conduction-band electron charge density (top) and valence-band hole charge density (bottom) for tetragonal $BaTiO_3$. For electron doping, the gray surfaces all have the same isosurface level (charge $\sim 7.5 \cdot 10^{-4}$ e) and show the location of the added electrons. For hole doping, the gray surfaces also have the same isosurface level, which is one order of magnitude larger than for electrons (charge $\sim 7.3 \cdot 10^{-3}$ e), and reveal where the electron depletion occurs.

We compute integrated Crystal Orbital Hamiltonian Populations (ICOHP) to confirm our explanation for the polarization decrease with increasing electron concentration. The bottom of Figure 3.1 shows the ICOHP as a function of the charge-carrier concentration for the Ti-O axial top, axial bottom and equatorial bonds (these are also illustrated in Figure 3.1). All the values are normalized to their respective value in the centrosymmetric structure. In the polar structure, the Ti is off-centered along c, resulting in a strong, short Ti-O axial top bond with a high ICOHP value and a weak, long bottom bond with a low ICOHP value. Upon adding electrons, the top bond is weakened and its ICOHP value is lowered. Conversely, the bottom bond is strengthened and its ICOHP

value increases. The Ti-O equatorial bonds are not particularly affected by the structural distortion decrease.

3.5.1.2 Hole Doping

In contrast to electron doping, the introduction of holes in tetragonal $BaTiO_3$ causes first an increase in polarization (from 0 to 0.2 h/u.c., as seen in the top of Figure 3.1), followed by a decrease ($>$ 0.2 h/u.c.) and complete suppression at 1.5 h/u.c. Overall, the amount of charge carriers needed to suppress the polar distortion is a factor 7.5 larger for hole doping than for electron doping.

The particular behavior of the hole-doped systems can be understood by considering their detailed densities of states. Figure 3.4 shows the oxygen site-resolved DOS for 0.1 and 0.5 h/u.c., with axial and equatorial sites shown separately. On removing electrons, the Fermi energy shifts down into the valence band, corresponding to a charge depletion of the oxygen atoms. For doping concentrations less than 0.1 h/u.c., we see (Figure 3.4, top panel) that electrons are largely only removed from the equatorial oxygen band, and the axial oxygens are almost unaffected. We will come back to this point below. For higher charge-carrier concentrations, depletion from the axial oxygen atoms starts to take place. We show in Figure 3.4 the case of 0.5 h/u.c. and see that the Fermi energy lies in both the axial and equatorial bands. Again invoking the SOJT effect, in which axial oxygens transfer electrons to the empty Ti d orbitals and stabilize the off-centering, we see that removing electrons from the axial oxygens reduces the tendency for the polar structural distortion to occur. The evolution of the electron depletion from equatorial to axial oxygens with increasing hole concentration can also be seen in the charge densities of Figure 3.3.

Next we consider the ICOHP which is plotted as a function of the hole concentration in Figure 3.1. This allows us to understand the polarization increase at small hole concentrations, where charge depletion from the equatorial oxygen is dominant. This electron depletion weakens the equatorial Ti-O bonds, reduces the tension in the equatorial plane, and allows the polar displacements along c to increase. (Note that

the equatorial bond weakening is not resolved in the equatorial Ti-O ICOHPs because of its small amount). Correspondingly, between 0 and 0.2 h/u.c., the Ti-O axial bottom bond is weakened and the Ti-O axial top bond is strengthened, as seen in their respective decreasing and increasing ICOHP values. For 0.3 h/u.c. and larger, a behavior similar to the electron doping case is observed, consistent with the observed loss of polarization. The ICOHP values for the Ti-O axial top bond follow the trend of the polarization values, indicating a direct relation between changes in polarization and Ti-O bond strength.

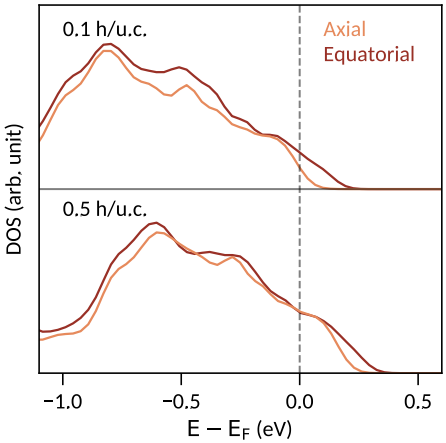

FIGURE 3.4: Oxygen site-resolved densities of states for tetragonal $BaTiO_3$ doped with 0.1 h/u.c. (top) and 0.5 h/u.c. (bottom). At 0.1 h/u.c., electrons are primarily removed from the equatorial oxygen atoms. At 0.5 h/u.c., the axial oxygen atoms are also strongly depleted.

3.5.1.3 Influence of Unit Cell Shape

Next we investigate the influence of the unit cell shape by comparing the behavior of tetragonal and pseudocubic (abbreviated *tet* and *cubic* in Figure 3.1) $BaTiO_3$. Note that, as mentioned above, the pseudocubic system has equal lattice parameters and therefore cubic shape, but we allow for a lower internal symmetry to permit a polar distortion. The tetragonal and pseudocubic systems follow the same trends, as seen in

the top of Figure 3.1. Their similarity can be explained by their comparable electronic structures (the DOS for the pseudocubic system can be found in Figures 3.6 and 3.7). The polarization of the pseudocubic system is, however, smaller than the tetragonal one and its polarization is suppressed faster. This is related to the absence of coupling to strain, and correspondingly smaller space in the c direction, resulting in smaller atomic displacements and thus a smaller polarization. In the rest of the paper, we present only the results for tetragonal $BaTiO_3$. Note that we focus on the tetragonal symmetry to provide guidelines on the behavior of $BaTiO_3$ at room temperature, and that we do not expect the mechanisms to be particularly different for other symmetries, for example the rhombohedral that occurs at low temperatures.

3.5.2 Introduction of Impurity Atoms in $BaTiO_3$ Supercells

In the second part of our study, we include explicit impurity atoms in tetragonal $BaTiO_3$ and investigate their effect on the polarization of the system. We consider electron and hole doping through A-site as well as B-site substitution. For electron doping, we introduce La on the A site and Nb or V on the B site. We explore hole doping through the introduction of K on the A site and Al or Sc on the B site. All dopants of interest add or remove one charge carrier per $2 \times 2 \times 2$ supercell, resulting in carrier concentrations of 0.125 carriers/u.c. Results for smaller charge-carrier concentrations can be found in Figure 3.9. Note that we consider only single substitutional impurities that introduce either one electron or one hole in their usual formal charge state. We do not investigate vacancies, the introduction of multiple defects or impurity-vacancy complexes.

For every X-$BaTiO_3$ system (where X denotes a general dopant), we perform three different calculations in order to identify and separate contributions to the polarization change. The first calculation consists of a structural relaxation of the internal coordinates of X-$BaTiO_3$ containing the impurity atom but not its corresponding charge carriers and with lattice constants fixed to their undoped values. We achieve this by compensating the charge carriers added with the dopant by

background-charge doping (the background charge requires the use of fixed lattice constants). We refer to this component as the *Impurity-atom contribution*. In the second calculation we remove the compensating background-charge and relax the internal coordinates of X-$BaTiO_3$ with the impurity atom and its charge carriers, still keeping the lattice constants fixed. We refer to this as the *Charge-carrier contribution*. In the third calculation, we make a full structural relaxation of both the internal coordinates and lattice parameters of X-$BaTiO_3$, containing the impurity atom with its charge carriers; we call this situation *free lattice constants* and we refer to this third component as the *Lattice-constant contribution*. This last system corresponds to the most realistic one. These three scenarios allow us to separate the contributions to the polarization change coming from the impurity atom, from the charge carriers and from changes in lattice constants. In the next sections, we present a detailed analysis of these contributions for the different impurity-doped $BaTiO_3$ systems. A compact overview of the discussed systems and features can be found in Table 3.1. The polarization changes arising from the different contributions are illustrated in Figure 3.5. Background-charge results are given as a reference in both cases and all given polarization changes ΔP in % refer to the changes compared to the original $BaTiO_3$ polarization.

Note that all the listed Shannon ionic radii are taken from Refs. [167, 168] and that tolerance factors are calculated with these values, with the charge of the impurity ion taken as its formal charge when introduced as a dopant – e.g. 5+ for Nb – with the coordination number appropriate to the substituted site (12 for the A site and 6 for the B site).

3.5.2.1 Donor Doping

A-Site Dopants We start by considering the La-doped $BaTiO_3$ system ($Ba_{1-x}La_xTiO_3$, BLTO). The La substitutes on the A site as formally trivalent La^{3+}, which has a smaller ionic radius than Ba^{2+} and, as we discuss below, influences therefore the structure of the system.
Impurity-atom contribution When a La atom without its respective charge carriers is added to $BaTiO_3$, we find that the polarization of the system increases by 8 %, due to a displacement of the small La^{3+} cation in the c

TABLE 3.1: Overview of the investigated doped $BaTiO_3$ systems and their calculated total polarization changes ΔP. The dopants are listed with specification of their type and site. *Background* refers to doping through the background-charge method and is intended to serve as a reference. The contributions from the impurity atom, the charge carriers and the free lattice constants are highlighted. The size of the impurity atom refers to its Shannon ionic radius. The reference ionic radii of Ba^{2+}, Ti^{4+} and O^{2-} are 1.61 Å, 0.61 Å and 1.35 Å, respectively. The systems can be described as *non-polar* or *polar*

Doping type	Dopant	Site	Impurity atom		Charge carriers		Lattice constants		Total ΔP (%)	Description
			Size (Å)	SOJT	Type	Localization	Volume	Tetragonality		
Donors	Background	-	-	-	e^-	no	-	-	−29	-
	La^{3+}	A	1.36	-	e^-	no	↓	loss	−100	non-polar
	Nb^{5+}	B	0.64	yes	e^-	yes	const.	loss	−58	polar
	V^{5+}	B	0.54	yes	e^-	yes	↓	loss	−30	polar
Acceptors	Background	-	-	-	h^+	no	-	-	+2	-
	K^+	A	1.64	-	h^+	no	const.	gain	+24	polar
	Al^{3+}	B	0.54	no	h^+	no	↓	loss	−36	polar
	Sc^{3+}	B	0.75	yes	h^+	no	↑	loss	−19	polar

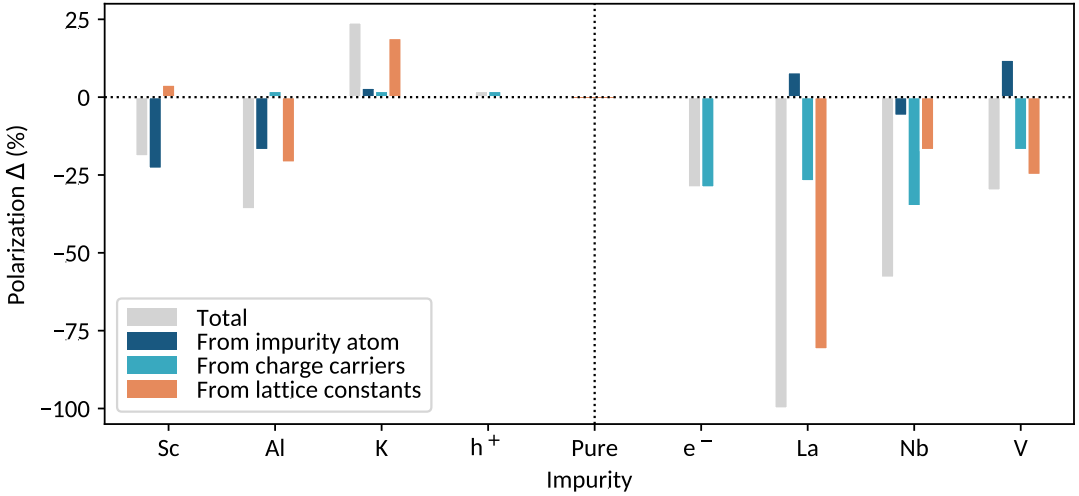

FIGURE 3.5: Polarization difference caused by the introduction of doping in tetragonal $BaTiO_3$. All the systems have a charge-carrier concentration of 0.125 carriers/u.c., corresponding to one impurity atom in a $2 \times 2 \times 2$ supercell. Positive polarization Δ values (y axis) correspond to a polarization gain, negative ones to a polarization loss. The total polarization difference (gray) is split into contributions corresponding to: i) The effect of the impurity atom without its carriers (dark blue). ii) The effect of the introduced charge carriers (teal). iii) The effect of the changing shape and volume of the system (orange). The total polarization change is obtained as the sum of the competing contributions present in the system.

direction. Besides directly contributing to the polarization of the system, the La also has an influence on the Ti sites in two ways: First, the La is underbound and pulls the Ti atoms immediately above it towards itself, reducing their off-centering. Second, the La displacement along c leaves more space for the Ti below it to off-center; this contribution dominates over the first.

Charge-carrier contribution Upon adding the electrons, the polarization of the system is reduced by 27 % compared to the original $BaTiO_3$ polarization. This value is close to that found in the background-charge doped reference (29 %). In fact, the introduction of the La does not influence the density of states of the system. The La f states lie high in energy and do not affect the region around the Fermi energy; the bottom of the conduction band therefore has pure Ti character and the electrons distribute homogeneously over the B sites of the system.

Lattice-constant contribution Finally we consider the relaxation of the lattice constants. Here we find that the decreases in both volume and tetragonality, due to the small La size, reduce the polarization by a further 81 %.

Summary The introduction of La in $BaTiO_3$ results in a complete polarization suppression with all the atoms adopting their centrosymmetric positions. The volume and tetragonality decrease caused by the small La size are the main factors dominating the polarization loss. Experimental reports claim that the conduction mechanism in BLTO is of polaronic nature [136]. No polaronic localization is seen in the above presented results. This could be due to an incomplete description of the charge imbalance compensation mechanisms present in the system. We consider only an electronic compensation of $Ba^{2+} \Rightarrow La^{3+} + e^{-}$, without any further ionic contributions as reported in the literature (e.g. $4Ba^{2+} + Ti^{4+} \Rightarrow 4La^{3+} + V_{Ti}$) [169]. Furthermore, hybrid functionals might be necessary to capture polaronic behavior, as they have been shown to properly describe polarons coexisting with delocalized electrons in TiO_2 [170].

B-SITE DOPANTS We consider Nb and V as B-site substituting donor impurities; the respective systems can be written as $BaTi_{1-x}Nb_xO_3$ (BTNO) and $BaTi_{1-x}V_xO_3$ (BTVO). When introduced in $BaTiO_3$, Nb

and V are present as Nb^{5+} and V^{5+}, respectively, and have therefore formally empty d orbitals, making them SOJT active. Nb^{5+} (0.64 Å) is larger than Ti^{4+} (0.61 Å), whereas V^{5+} (0.54 Å) is smaller. The off-centering of the two dopants depends on their size and the tolerance factor of the structure.

We begin with the Nb-doped $BaTiO_3$ system:
Impurity-atom contribution The introduction of the Nb without its charge carriers decreases the polarization by 6 %, due to the reduced off-centering of the Nb atom and its axial neighboring Ti along the polar axis. The reduced structural distortion is due to the Nb size: The tolerance factor of $BaNbO_3$ is 1.03, compared to 1.07 for $BaTiO_3$. Although it has the empty d orbital configuration needed to be SOJT active, it is too big to actually off-center. The Ti atoms axial to the Nb are directly affected by the Nb behavior: Since the Nb is less off-centered, they have less space to displace in the c direction and are more centrosymmetric.
Charge-carrier contribution The addition of the electrons reduces the polarization by a further 35 %, which is more than expected from the background-charge reference (29 %). The additional suppression results from a slight accumulation of the electrons on the Nb atom and its axial neighboring Ti along the polar axis, which have the largest contribution to the bottom of the conduction band (Figure 3.10). The electron accumulation heavily reduces the structural distortion of these two sites, increasing the polarization loss due to the presence of the charge carriers.
Lattice-constant contribution When the lattice constants are relaxed, the polarization is reduced by a further 17 %. This polarization change can be assigned to the reduced tetragonality since the volume of the system stays rather constant. Note that this constant volume is not directly intuitive. In fact, Nb^{5+} is larger than Ti^{4+}, so that a structural expansion would be expected. It is nevertheless counterbalanced by the loss of polarization, resulting in an unchanged volume.
Summary Nb-doped $BaTiO_3$ remains polar, although with an overall polarization decrease of 58 %. The charge carriers are the most important factor contributing to the polarization loss. We find that they tend to accumulate on the Nb atom and its nearest axial Ti, consistent with the polaronic conduction mechanism proposed in the literature [137, 138].

Next we evaluate the polarization change in the V-doped system where we find that the small size of V leads to markedly different behavior.
Impurity-atom contribution The addition of V without its respective charge carriers induces a polarization increase of 12 %: The V is smaller than the Ti and therefore able to off-center more ($BaVO_3$ has a large tolerance factor of 1.11). The Ti axial to the V are also off-centered more because the V influences its axial environment and induces a cascade off-centering – the same effect but in the reverse direction as that seen for the BTNO system.
Charge-carrier contribution The introduction of electrons decreases the polarization by 17 % compared to pure $BaTiO_3$, which is less than expected from the background-charge reference (29 %). The added charge carriers strongly localize on the V because of its very large contribution to the bottom of the conduction band (Figure 3.11). We might expect this localization to increase the polarization suppression, as seen in the BTNO system. However, in this case the V is so small that it displaces and contributes to the polarization even if its SOJT hybridization stabilization is quenched by the extra electrons. In addition, the electron localization on the V reduces their accumulation on the Ti sites, so that their polar structural distortions are not affected much by the doping.
Lattice-constant contribution The relaxation of the lattice constants results in a further polarization decrease of 25 %. This is explained by the reduced volume and tetragonality, due to the small V size.
Summary The introduction of V in $BaTiO_3$ reduces the polarization by overall 30 %. The addition of electrons reduces the expected polarization loss compared with the background-charge reference because of charge-carrier localization on the V site, an effect which has also been reported in the literature [171]. V doping in $BaTiO_3$ has been observed experimentally to increase the polarization for low V concentrations ($<$ 0.5 at%), followed by a polarization loss at higher concentrations [172], consistent with our calculations.

3.5.2.2 Acceptor Doping

A-Site Dopants Now we move to acceptor doping and begin with the substitution of monovalent K on the Ba A site. In the K-doped

$BaTiO_3$ system ($Ba_{1-x}K_xTiO_3$, BKTO), the K is present as K^+, which is only slightly larger than Ba^{2+}.

Impurity-atom contribution Adding a K atom with no additional charge carriers causes a polarization gain of 3 %, caused by complex atom rearrangement, which shows the tendency of the system towards tetragonality, as we will further discuss in the *Lattice-constant contribution* section. This results in a displacement of the K^+ ion in the c direction, increased displacements of the Ti on the plane below the K – they have more space to off-center because of the K displacement – and decreased off-centering of the Ti above the K.

Charge-carrier contribution Electron depletion increases the polarization by a further 2 %. This is in agreement with the effect observed in the background-charge doped $BaTiO_3$ (2 %). In fact, the introduction of the K atom has no particular influence on the valence band of the system, which has still O 2p character.

Lattice-constant contribution The lattice constant relaxation induces a further polarization increase of 19 %. When adding a K atom, the volume of the system stays rather constant, as K^+ is only slightly bigger than the Ba^{2+}. More interestingly, the tetragonality of the system is considerably increased, explaining the polarization increase. This indicates that structural factors affect the polarization of the system primarily through their influence on the polar c axis: the more space in the c direction (rather than the overall volume), the higher the potential for a polar distortion.

Summary The introduction of K in $BaTiO_3$ at a concentration 0.125 h/u.c. overall increases the polarization of the system by 24 %, mainly because of the increased tetragonality. We remind the reader that our polarization values are obtained using the Ba Born effective charge of + 2.7 for K and that they are therefore likely to be smaller in practice.

B-Site Dopants Finally we move to the B-site hole dopants and consider two impurities: Al^{3+} which is quite ionic, and Sc^{3+} which is SOJT active.

We begin with the Al-doped $BaTiO_3$ ($BaTi_{1-x}Al_xO_3$, BTAO) in which the trivalent Al^{3+} is smaller than Ti^{4+}; we expect it therefore to have a strong structural influence.

Impurity-atom contribution Introducing an Al atom in $BaTiO_3$ without its corresponding charge carriers reduces the polarization by 17 %. The Al atom has in fact a reduced off-centering, since it has no d orbitals that would favor its hybridization with the axial oxygen atom. It is nevertheless still slightly displaced compared to its centrosymmetric position because of its small size. The tolerance factor of pure $BaAlO_3$, 1.11, indicates that the Al is small enough to rattle. The decreased Al off-centering also reduces the off-centering of the its axial neighboring Ti along the polar axis.
Charge-carrier contribution Electron depletion increases the polarization by 2 %, consistent with the background-charge doped reference and the minimal influence of the Al on the electronic structure in the region of the Fermi energy. While the electron depletion on the oxygen atoms around the Al has a small effect, the depleted equatorial oxygens around the Ti ions cause an increased off-centering of the Ti as in the background-charge case. The Ti axial to the Al are particularly affected, because of the high contribution of the oxygen atoms around them to the top of the valence band, and contribute most to the polarization gain.
Lattice-constant contribution Upon relaxing the lattice constants, a polarization loss of 21 % occurs. This is due to a decrease of the volume and tetragonality of the system, reducing the B-site off-centering homogeneously.
Summary The introduction of Al into $BaTiO_3$ reduces the polarization, overall by 36 %. This is mainly due to the non-off-centering of the Al, which has no d orbitals and is therefore not SOJT active, as well as the loss of space through volume contraction and tetragonality decrease.

The last system that we analyze is Sc-doped tetragonal $BaTiO_3$ (BTSO, $BaTi_{1-x}Sc_xO_3$), where Sc is present as Sc^{3+}. Sc^{3+} is larger than Ti^{4+} so that we expect it to influence the structure of the system.
Impurity-atom contribution Adding a Sc without its charge carriers reduces the polarization by 23 %. The transition metal sites causing the polarization loss are the Sc site and its axial neighboring Ti along the polar axis. The origin, as in the BTNO system, is the large Sc^{3+} size: The $BaScO_3$ tolerance factor is 0.99, meaning that, even though it is SOJT active, the Sc is too big to actually displace in the c direction. The

Ti axial to the Sc also off-center less. This is due to the Sc influencing its axial environment; as it is almost centrosymmetric, there is less space for the atoms around it to off-center.
Charge-carrier contribution Electron depletion increases the polarization by less than 1 %, a smaller amount compared to the background-charge doped reference (2 %). The oxygen atoms contributing most to the top of the valence band, and therefore most depleted upon doping, are the equatorial and axial oxygens around the Sc. However, because of its large size, the Sc is not affected by this depletion, reducing the net polarization gain.
Lattice-constant contribution When the lattice constants of the system are relaxed, the polarization increases by 4 %. This is related to the volume expansion due to the Sc^{3+} being bigger than the Ti^{4+}. The tetragonality of the system stays constant and therefore neither counterbalances the volume effect nor increases it.
Summary The net polarization loss in BTSO amounts to 19 %. This is due to the large size of the Sc counteracting the other factors that would increase the polarization of the system.

3.5.2.3 Overview Impurity Doping

Our results suggest that the factors contributing to the polarization change can be divided into three effects: i) the chemistry and size of the impurity atom, ii) the charge carriers and their degree of localization, and iii) changes in tetragonality and volume.

The influence of the impurity atom depends on its size and SOJT activity. On the A site, small dopants tend to increase the polarization by cation displacement (e.g. La). Note that the polarization increase due to doping with small A-site cations cannot be achieved if all the A sites are substituted, where cooperative rotations would be preferred over the polar distortion (as seen in e.g. $SrTiO_3$) [173]. On the B site, off-centering is controlled by the presence of empty d orbitals (for the atom to be SOJT active) and the space available for off-centering, which correlates with the size of the atom. The off-centering of SOJT active atoms can be suppressed if they are too large (e.g. Nb and Sc) and does not occur if they lack empty d orbitals in an appropriate

energy range (e.g. Al). If both SOJT activity and small size are present, increased off-centering is observed (e.g. V). A theoretically promising (although experimentally inaccessible) avenue would correspond to doping $BaTiO_3$ with a SOJT active acceptor atom that is smaller than Sc. This is however not feasible as Sc^{3+} is the smallest trivalent SOJT active ion that exists.

The effect of the charge carriers depends on their type and degree of localization. Electrons have a stronger influence on the polarization than holes, as already discussed for the background-charge doped systems. Overall, electrons reduce the polarization, while charge carrier localization can increase (e.g. Nb) or decrease (e.g. V) the extent of the reduction. In contrast, the introduction of holes very slightly increases the polarization of the system at 0.125 carriers/u.c.

The relaxation of the lattice constants permits changes in the tetragonality and volume of the system depending on the introduced dopant. Small atoms tend to induce a volume contraction, reducing the polarization; conversely, large atoms expand the volume and increase the polarization. The determining factor for the polarization change is the gain or loss of space in the polar direction, which results in a change in tetragonality through the coupling to strain.

We find that the contributions from the impurity atom, the charge carriers and the free lattice constants are additive. At 0.125 carriers/u.c., the polarization change ranges from a gain of 25 % to a loss of 100 % (compared to pure $BaTiO_3$), depending on the introduced impurity. Which of the contributions dominates depends on the dopant. A general trend can nevertheless be recognized from Figure 3.5. For donor dopants, the charge carriers are a dominating factor for the polarization loss, in contrast to acceptor doping, where the chemistry and size of the impurity atom have a prevailing contribution. In both doping regimes, the changes in tetragonality and volume have a strong influence on the system behavior.

Based on our calculations, we can classify the investigated impurity-doped systems with 0.125 carriers/u.c. into one of three categories, based on structural and electronic considerations. In the electron-doped

systems, BLTO can be considered to be metallic and non-polar. In fact, it has homogeneously spread out electron charge carriers and a centrosymmetric crystal structure, since the polar distortion is completely suppressed. BTNO and BTVO can be regarded as being polar-metal-like with a polaronic conduction mechanism, due to the electron localization on the impurity atom or its axial neighboring Ti along the polar axis. They show both a polar structural distortion, have a non-zero density of states at the Fermi level and the polaronic electron localization could enable polarization switching. The hole-doped systems can also be considered as being polar-metal-like, and in the case of K doping their polarization is even increased over the undoped case.

3.6 Conclusions

In conclusion, we demonstrated computationally that $BaTiO_3$ can sustain the combination of ferroelectric and metallic properties. With the background-charge method, we found that at low carrier concentrations (< 0.2 carriers/u.c.), hole doping increases the polarization, whereas electron doping reduces it. At higher concentrations, both electrons and holes reduce the polarization of the system by suppressing the B-site off-centering. The effect of electrons is stronger than that of holes because of the nature of the conduction and valence bands: The electrons strongly affect the Ti ions, whereas the holes spread out over both equatorial and axial oxygens. We found that in impurity-doped systems, multiple structural and electronic factors contribute to the polarization change. The contributions can be separated into effects coming from the chemistry and size of the impurity atom, from the charge carriers and from changes in the shape and volume of the system. These contributions are additive and can overall yield a gain (K) or loss (La, Nb, V, Al, Sc) of polarization, depending on the introduced dopant. Based on our calculations, we propose a classification of the investigated materials at low doping concentration as either non-polar metallic (La) or polar-metal-like (Nb, V, K, Al, Sc).

Based on our findings, we propose following experiments to further investigate the interplay between ferroelectricity and metallicity in

$BaTiO_3$. Field effect doping could contribute to understanding the effect of charge carriers in $BaTiO_3$, as predicted by our calculations with background charges. Furthermore, doping of $BaTiO_3$ with Nb or V could be particularly promising for polarization switchability, which could be allowed by the polaronic localization of the charge carriers in these systems.

Conflicts of Interest

There are no conflicts to declare.

Acknowledgments

This work was funded by the European Research Council under the European Union's Horizon 2020 research and innovation program Grant Agreement No. 810451, the Körber Foundation and ETH Zurich. V. F. M. was supported by a MARVEL INSPIRE Potentials Master's Fellowship from the NCCR MARVEL, funded by the Swiss National Science Foundation. Calculations were performed on the ETH Zurich Euler cluster.

3.7 Supplementary Information

If not otherwise specified in the caption of the figures, the computational parameters used correspond to those described in the methods section of the main text.

Background-charge Doped Pseudocubic $BaTiO_3$

Additional densities of states for doped cubic $BaTiO_3$.

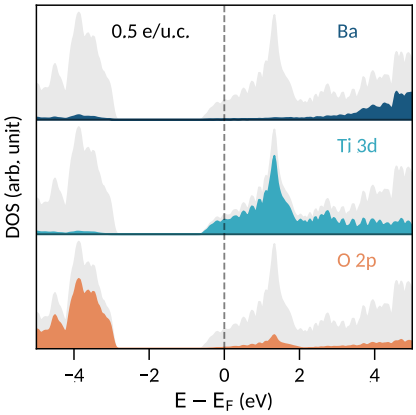

FIGURE 3.6: Density of states for pseudocubic $BaTiO_3$ doped with 0.5 e/u.c.

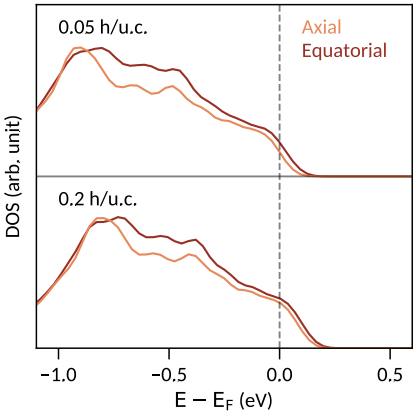

FIGURE 3.7: Oxygen site-resolved densities of states for pseudocubic $BaTiO_3$ doped with 0.05 h/u.c. (top) and 0.2 h/u.c. (bottom).

Undoped Tetragonal $BaTiO_3$

Results of the Berry-phase calculation for undoped tetragonal $BaTiO_3$.

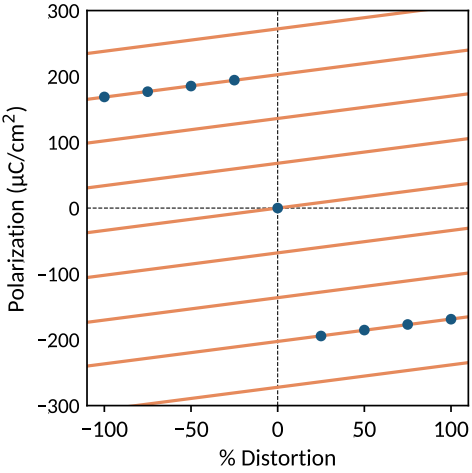

FIGURE 3.8: Berry-phase calculation for tetragonal $BaTiO_3$. The calculated spontaneous polarization of the system is 34 $\mu C/cm^2$.

Impurity-doped $BaTiO_3$ Supercells

Additional calculation results for $BaTiO_3$ supercells: Polarization, volume and tetragonality; bond ratios; and densities of state.

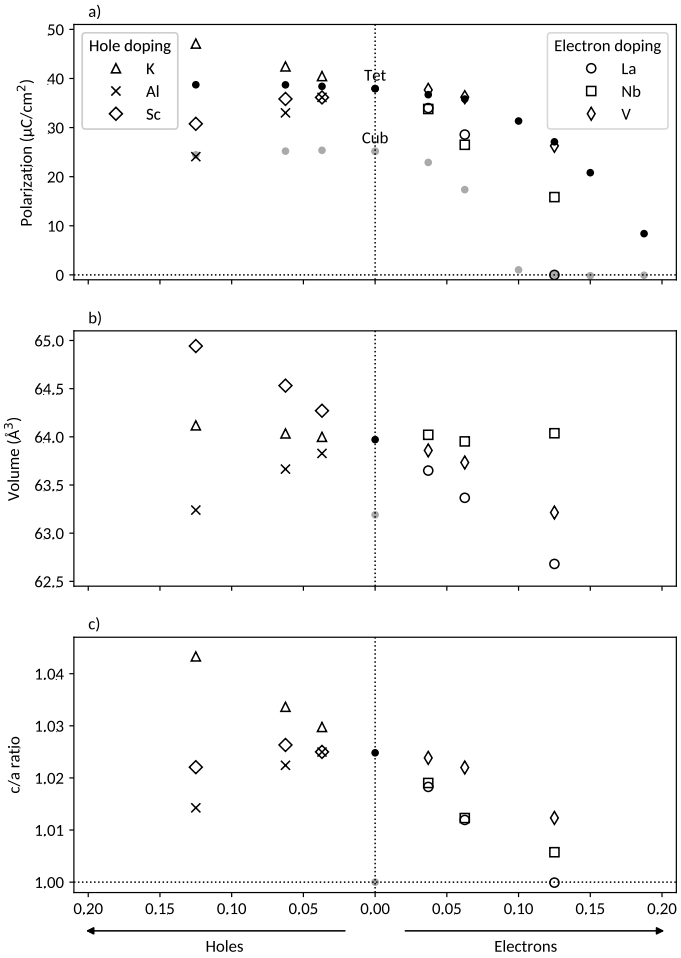

FIGURE 3.9: Polarization (a), average volume (b) and c/a ratio (c) of doped $BaTiO_3$ as a function of the charge-carrier concentration (electrons on the right, holes on the left). The charge carriers are introduced through doping with impurity atoms in $2 \times 2 \times 2$, $2\sqrt{2} \times 2\sqrt{2} \times 2$ and $3 \times 3 \times 3$ supercells and their charge-carrier concentrations are 0.125, and 0.0625 and 0.037 carriers/u.c., respectively. The k-point grids used for these calculations are $12 \times 12 \times 12$, $6 \times 6 \times 6$ and $4 \times 4 \times 4$, respectively. The systems are labeled with the name of their respective dopant. The black and grey dots correspond to the tetragonal and pseudocubic background-charge references.

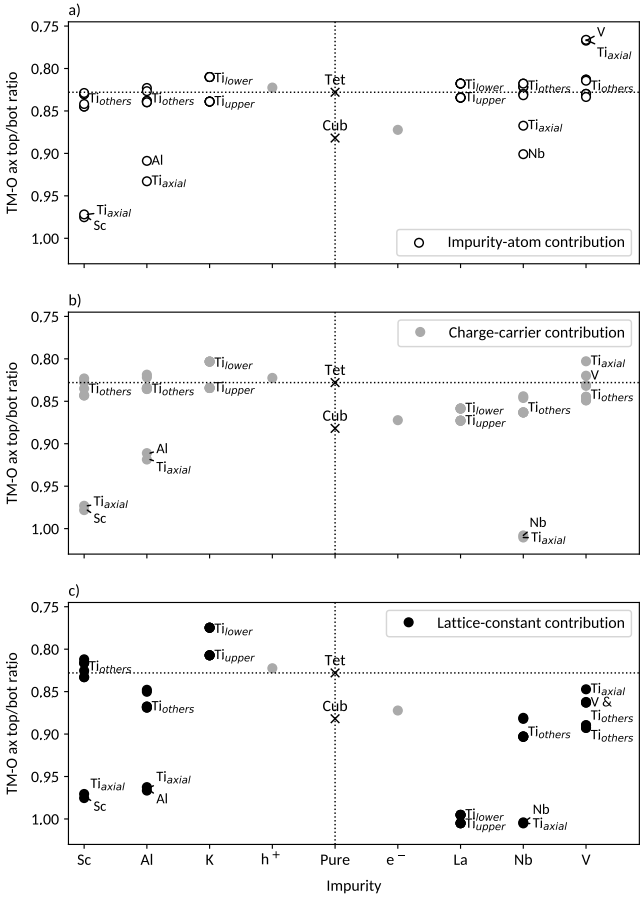

FIGURE 3.10: Bond ratios of the transition metal – oxygen axial top to bottom bonds for tetragonal $BaTiO_3$. a) Impurity-atom contribution with the impurity atom, 0 carriers/u.c. and fixed lattice constants (white circles), b) Charge-carrier contribution with the impurity atom, 0.125 carriers/u.c. and fixed lattice constants (grey circles) and c) Lattice-constant contribution with the impurity atom, 0.125 carriers/u.c. and free lattice constants (black circles). The impurity atom is indicated on the x-axis. Each system corresponds to a $2 \times 2 \times 2$ supercell and therefore has eight bond ratio values (for its eight transition metals), partly overlapping. Pure $BaTiO_3$ in tetragonal and pseudocubic symmetry (abbreviated *tet* and *cub*) as well as background-charge doped tetragonal systems (holes: h^+, electrons: e^-) are given as a reference.

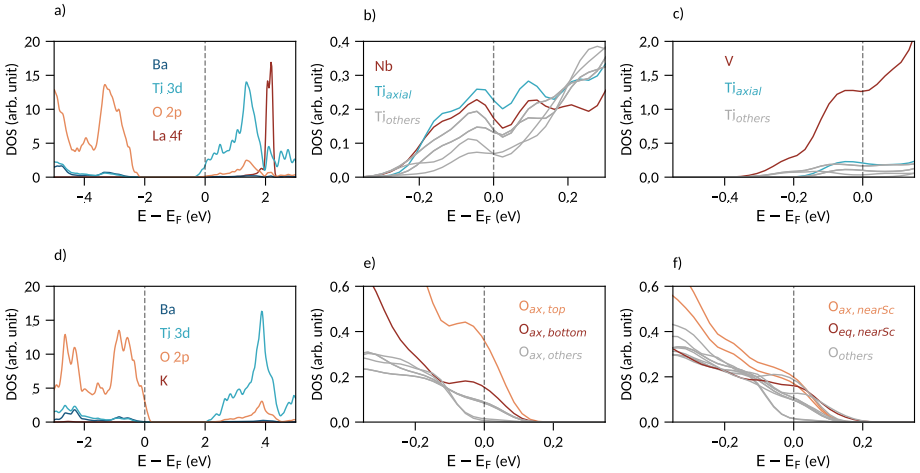

FIGURE 3.11: a) Density of states for La-doped $BaTiO_3$ (with one La in a $2 \times 2 \times 2$ $BaTiO_3$ supercell with fixed lattice constants). As the La introduces one valence electron into the system, the Fermi energy lies in the conduction band. The La f-states lie at higher energies and the main contribution to the conduction band comes from the Ti d orbitals. b) Transition-metal site-resolved density of states of Nb-doped $BaTiO_3$ (BTNO with one Nb in a $2 \times 2 \times 2$ $BaTiO_3$ supercell and fixed lattice constants). The region around the Fermi energy in the conduction band is shown. Two sites, the Nb and its axial neighboring Ti along the polar axis, have particularly large contributions. c) Transition-metal site-resolved density of states for V-doped $BaTiO_3$ (with one V in a $2 \times 2 \times 2$ $BaTiO_3$ supercell with fixed lattice constants). The conduction band region around the Fermi energy is shown. The V has a particularly large contribution, whereas the its axial neighboring Ti along the polar axis hardly contributes to the conduction band. d) Density of states for K-doped $BaTiO_3$ (BKTO with one K in a $2 \times 2 \times 2$ $BaTiO_3$ supercell and fixed lattice constants). One valence electron is depleted from the system so that the Fermi energy lies in the valence band. The K does not affect the DOS around the Fermi energy. e) Axial oxygen site-resolved density of states of Al-doped $BaTiO_3$ (with one Al in a $2 \times 2 \times 2$ $BaTiO_3$ supercell with fixed lattice constants). The most contributing sites are the axial oxygens around the Al atom (top and bottom). f) Oxygen site-resolved density of states of Sc-doped $BaTiO_3$ (BTSO with one Sc in a $2 \times 2 \times 2$ $BaTiO_3$ supercell and fixed lattice constants). The most contributing sites are the axial and equatorial oxygens around the Sc atom. All the supercells have tetragonal symmetry. All DOS are computed with a $12 \times 12 \times 12$ k-point grid.

3.8 Data availability

All input data and selected output data is available here:

Veronica F. Michel, Tobias Esswein and Nicola A. Spaldin. Interplay between ferroelectricity and metallicity in $BaTiO_3$, *Materials Cloud Archive* 2021.75 (2021). DOI: 10.24435/materialscloud:f4-94 .

3.9 Summary and Outlook

In this section we have learned several things, some of them unexpected, which are relevant for the rest of this thesis. The first is that polarization can exist even if there are free carriers present, which is relevant for the topic of polar-fluctuation mediated superconductivity. Compared with the case of electron doping, in the case of hole doping, the polarity is sustained up to surprisingly higher carrier concentrations, mainly because the emptying of the valence band changes chemical bonding differently from the filling of the conduction band. We also saw that different impurity atoms have strongly varying effects on the geometric and electronic properties, ranging from complete suppression of polarization in the case of La doping, to the increase of polarization in the case of K doping. The predicted increase of polarization in the cases of hole doping and K doping is surprising, and experiments to verify this prediction would be interesting. Finally, the change of volume and tetragonality seems to have the largest influence on polarization, followed by the charge carriers in the electron-doped cases, and the chemistry of the impurity atom in the hole-doped cases.

A few comments on the computational choices we made for this project: We used a tetragonal unit cell for several reasons, mainly because it is the crystal structure that is stable at room temperature, but also because the actual change of polarization between tetragonal, orthogonal and rhombohedral is actually quite small [39]. We used $2 \times 2 \times 2$ supercells, with one atom replaced, for the main body of the paper, resulting in a doping of 0.125 e/u.c. – increasing the size of the supercells proved computationally challenging. Results for larger supercells of sizes $2\sqrt{2} \times$

$2\sqrt{2} \times 2$ and $3 \times 3 \times 3$ are therefore restricted to the geometric analysis presented in figure 3.9. Generally, the advantage of larger supercells is threefold: they allow lower doping values (down to 0.0625 and 0.037, respectively; even lower for larger supercells), one can get closer to true disorder despite the periodic boundary conditions of plane-wave DFT, and one can study the formation of impurity-clusters in the crystal.

Future research in this area could be done in several directions. Staying with BTO, one direction is clearly to use larger supercells to investigate the effect of more disordered impurities, as mentioned earlier, as well as the range of lower doping levels. Additionally, increasing the supercell size would allow the study of oxygen vacancies (with a charge of $2-$), which were used in ref. [52] to introduce free carriers, but are quite difficult to capture properly in ab-initio calculations, as a recent study of oxygen vacancies in STO has shown [174]. Finally, one could take the quantum nature of the ions into consideration. While this has been shown to have a minimal effect for high-T_c proper ferroelectrics like BTO [175], it is known to be important for quantum paraelectrics like STO [175] and KTO [176]. One possible way of doing this is based on the model we have developed for quantum paraelectricity in STO and KTO, which is the centerpiece of the next chapter.

4

A simple model for quantum paraelectrics

4.1 Preface

Quantum criticality is at the origin of several unusual materials' phenomena, one of them is high-temperature superconductivity, as e.g. in the cuprates, in which a quantum critical point sits in the middle of the superconducting dome (and many other peculiar phases) [177, 178]. In quantum *paraelectric* materials, quantum fluctuations prevent the transition to a ferroelectric phase by stabilizing the paraelectric one, as first observed in $SrTiO_3$ in 1979 [18] (for more details on quantum phase transitions and quantum paraelectricity in $SrTiO_3$, see sections 1.1.2 and 1.2.2, respectively). In the case of quantum paraelectricity, a paper by Edge et al. in 2015 [35] proposed a mechanism linking the quantum fluctuations with superconductivity in STO, based on an observation reproduced here as figure 4.1.

The superconducting dome is represented by the blue dots, while the red lines indicate the calculated hardening of the ferroelectric soft phonon mode, which is imaginary at low doping values, and becomes real when it crosses the dashed horizontal line, which happens just in the center of the superconducting dome. This observation motivated the construction of a model which was not only able to reproduce the dome shape of the critical temperatures, but also predicted an unusual superconducting isotope effect in STO: The critical temperature should increase upon ^{18}O-isotope substitution, in contrast to the usual BCS-predicted T_c lowering upon isotope substitution with a heavier isotope [27, 179]. The experimental confirmation of this unusual isotope effect

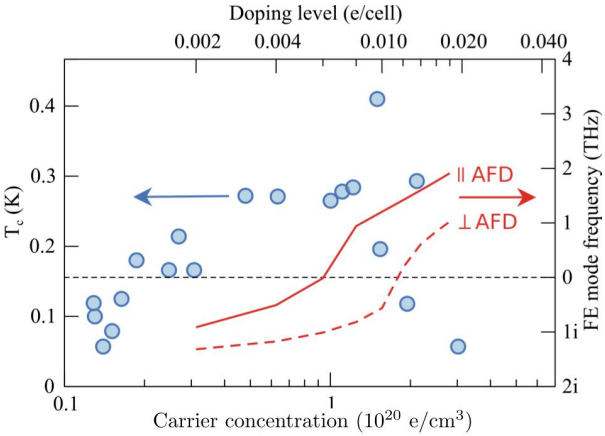

FIGURE 4.1: Plot of the superconducting dome in $SrTiO_3$ (blue dots) and the quantum critical point as defined by the hardening of the soft phonon modes (red lines) (right). The general idea of a quantum critical point sitting in the center of the superconducting dome is very similar to the phase diagram of high-temperature superconductors, e.g. the cuprate ones [177, 178].

—

Figure reproduced and adapted from Figure 1 of "Quantum Critical Origin of the Superconducting Dome in SrTiO3" by Edge *et al.* [35], with permission from the authors. Copyright (2015) by the American Physical Society.

just one year later [69] led to an increase in research efforts trying to explain the origin of superconductivity in STO [67, 173, 180–182].

The still-unexplained superconductivity and the possible connection to quantum paraelectricity were a strong incentive for us to investigate in more detail the quantum paraelectric state in both STO and KTO. However, we quickly realized that the definition of the quantum critical point may not be as straightforward as the previously assumed crossover of the soft phonon mode from imaginary to real frequencies. First, the calculation of the phonon frequency is within the harmonic and the Born Oppenheimer approximations, where the atoms are assumed to be classical particles and essentially static from the perspective of the electrons and there is no anharmonicity. This is incompatible with the picture of a quantum paraelectric state in which

quantum fluctuations stabilize the paraelectric phase by means of ions fluctuating or tunneling through energy barriers they should not be able to cross in a classical model [183]. Additionally, in reviewing the literature models for tunneling in this quantum paraelectric state, the preferred view seemed to be that of the titanium ion fluctuating within its oxygen cage, which already seems unlikely for the titanium ions, and even less likely for the heavy tantalum ion in KTO.

All of these points led us down a rabbit hole of literature research and new calculations, including a foray into quantum chemistry, and resulted in the peer-reviewed work that constitutes the main part of this chapter. We first present a model for quantum paraelectricity, based on simple DFT- and DFPT-calculated quantities and including the quantum nature of the ions. We then use this model, first to check its validity going from BTO to STO to KTO, and then to investigate the isotope effect in STO and compare it with a simple geometric distortion of the unit cell. We find that the model works best for (quantum) paraelectrics and still reasonably well for ferroelectrics, although it yields an isotope effect that is smaller than reported. We also summarize the various possibilities for separating mass and displacement and which one to choose if necessary.

Explanatory Remarks

The following section is published as:

Tobias Esswein and Nicola A. Spaldin. Ferroelectric, quantum paraelectric or paraelectric? Calculating the evolution from $BaTiO_3$ to $SrTiO_3$ to $KTaO_3$ using a single-particle quantum-mechanical description of the ions. *Phys. Rev. Research* 4, 033020 (2022). DOI: 10.1103/PhysRevResearch.4.033020.

—

4.2 Abstract

We present an inexpensive first-principles approach for describing quantum paraelectricity that combines density functional theory (DFT) treatment of the electronic subsystem with quantum-mechanical treatment of the ions through solution of the single-particle Schrödinger equation with the DFT-calculated potential. Using $BaTiO_3$, $SrTiO_3$ and $KTaO_3$ as model systems, we show that the approach can straightforwardly distinguish between ferroelectric, paraelectric and quantum paraelectric materials, based on simple quantities extracted from standard density functional and density functional perturbation theories. We calculate the influence of isotope substitution and strain on quantum paraelectric behavior and find that, while complete replacement of oxygen-16 by oxygen-18 has a surprisingly small effect, experimentally accessible strains can induce large changes. Finally, we collect the various choices for the phonon mass that have been introduced in the literature. We identify these that are most physically meaningful by comparing them with our results that avoid such a choice through the use of mass-weighted coordinates.

4.3 Introduction

Quantum paraelectric materials, such as strontium titanate, $SrTiO_3$ (STO) and potassium tantalate, $KTaO_3$ (KTO), are incipient ferroelectrics whose ferroelectric phase transition on cooling is suppressed by quantum fluctuations [18]. They are characterized by a temperature-dependent transverse optical phonon, whose frequency tends to but does not reach zero at low temperature [184], and a correspondingly high low-temperature dielectric susceptibility [61] that deviates from classical Curie behavior with a cross-over to a characteristic T^{-2} scaling below a few tens of kelvin [17, 185]. Their proximity to ferroelectricity means that the ferroelectric state can be reached readily with external perturbations, including pressure [186, 187], homovalent A-site [188] or B-site substitution [189, 190], oxygen isotope substitution [191, 192] and strain [193, 194]. This sensitivity, combined with the low temperatures,

makes detailed characterization of the structure of the quantum paraelectric state challenging: Neutron and x-ray Rietveld analysis of STO, for example, indicate a centrosymmetric structure down to 1.5 K [195]. In contrast, nuclear magnetic resonance (NMR) shows local dynamic polar off-centering of the Ti ions [196], consistent with the anomalous vibrational amplitudes seen in γ-ray Bragg scattering [197], and scanning transmission electron microscopy reveals local polar nanoregions [198].

From a theoretical perspective, the quantum paraelectric behavior is broadly understood to result from quantum fluctuations suppressing the softening of the polar phonon, which would otherwise drive a ferroelectric phase transition at low temperature. Indeed, extension of the classic Slater model of ferroelectricity [199] to treat the soft polar mode quantum mechanically [76, 200] and with anharmonic coupling to other phonon modes modes [18, 201], correctly reproduces the T^{-2} scaling of the dielectric susceptibility. The importance of a shallow "double well" potential energy surface with its correspondingly small zero-point energy (Fig. 4.2) has been emphasized [202], with the isotope effect then explained by suppression of the zero-point motion by larger atomic masses [203]. First-principles electronic structure calculations based on density functional theory (DFT) confirm the shallow double-well picture [204] and indicate the importance of transition-metal – oxygen polarizability [205, 206], manifesting in anomalously large Born effective charges and giant LO-TO splittings [207, 208]. DFT studies have also explored the relationship between polar distortions and tetragonality, strain, unit-cell volume and oxygen octahedral rotations [209–211], as well as the effect of point defects on the structural properties [212].

Particularly important insights are provided by atomistic simulations using path-integral quantum Monte Carlo methods, in which the ionic motions are treated quantum mechanically. In such simulations, quantum effects are found to suppress the ferroelectric transition in STO completely as well as to strongly affect the behavior of the polar mode up to ~100 K; in KTO, quantum effects cause local correlated polar nanoregions [176]. In contrast, ionic quantum effects have a less prominent effect in the prototypical ferroelectric barium titanate, $BaTiO_3$

(BTO), with its high ferroelectric ordering temperature [175], although they can become important at high pressure [213]. Unfortunately, however, path-integral quantum Monte Carlo methods are computationally expensive even at high temperatures, and become unfeasible on approaching zero kelvin, and so are impractical for routine evaluation of material properties.

While many features of quantum paraelectricity are now established, major questions about the detailed nature of the quantum paraelectric state remain open. First, the existence or not of a zero-kelvin quantum critical point. While susceptibility measurements have been interpreted in terms of a quantum critical point that is crossed by either strain or ^{18}O substitution [17, 214, 215], the zero-kelvin limit has not in fact been reached [190], and instead an up-turn in dielectric susceptibility has been reported at very low temperatures [17, 216]. The up-turn points to a discontinuous transition, which is indeed captured by a Hamiltonian based on a polarizability model [217–219], and has been attributed to coupling to strain [214, 215]. Second, and related to the previous point, is the appropriateness of a double-well picture for describing the crossover from paraelectric through quantum paraelectric to ferroelectric behavior. Finally, unconventional superconductivity has been observed in both STO [31] and KTO [70, 72, 73], with ferroelectric quantum fluctuations proposed as the source of the pairing mechanism [35]. While the results of subsequent experiments, particularly the effects of strain and ^{18}O substitution, have proved consistent with the predictions of the quantum fluctuations model [67, 69, 173, 180–182], further insight into the nature of the quantum criticality would be invaluable in better understanding and optimizing the superconductivity.

In this work we use electronic structure calculations based on standard density functional theory (DFT), to explore the potential energy landscapes of a series of quantum paraelectrics and conventional ferroelectrics. Since conventional DFT does not treat the ions quantum mechanically, we then account for the quantum mechanical behavior of the ions in a second step by solving the Schrödinger equation explicitly for the ionic subspace using the calculated DFT potential. Our approach is similar to that used in Ref. [204], with the important differ-

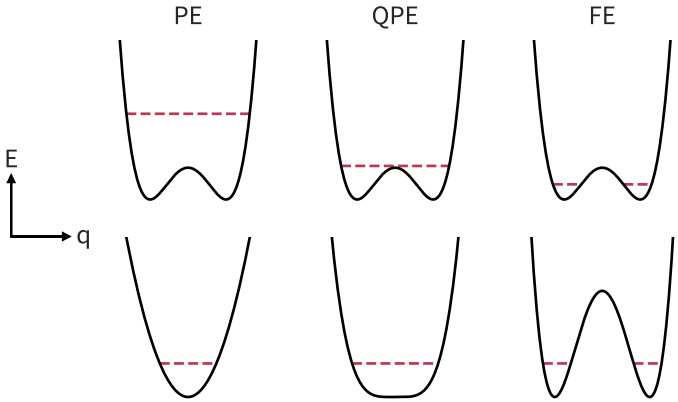

FIGURE 4.2: Illustration of two possible mechanisms for the crossover from the paraelectric (left) to ferroelectric (right) state. In each panel the vertical axis is internal energy, and the horizontal axis is the polarization (or relative displacements of the anionic and cationic sublattices), with the curves centered around zero polarization. The green dashed lines represent the zero-point energy levels. The lower row shows a behavior analogous to the usual Landau model of displacive phase transitions as a function of temperature: The internal energy has a double well potential resulting in a ferroelectric state at low temperature (right panel) with the barrier height reducing as temperature increases, so that there is a single minimum corresponding to zero polarization above the Curie temperature. Such a crossover could also occur at zero kelvin as a function of an external parameter such as strain or pressure, in which case the middle panel, in which the potential has a pronounced quartic component but not yet a barrier, would correspond to the quantum paraelectric state. In the upper row, the free energy is unchanged as a function of tuning parameter, but the zero-point energy evolves from high (corresponding to the paraelectric state) to low (corresponding to the ferroelectric state). In this case, quantum paraelectric behavior would be expected when the zero-point energy is in the vicinity of the top of the barrier between the oppositely polarized states. This behavior could be achieved by changing the masses of the atoms through isotopic substitution, which changes the mass without changing the form of the potential energy.

ence that we work in mass-weighted coordinates and so are not forced to make arbitrary assumptions about the sizes of the phonon mass and displacement.

Our primary scientific goal is to answer the question of how a ferroelectric emerges from a paraelectric as a function of an external (non-thermal) tuning parameter. In Fig. 4.2 we sketch two commonly discussed scenarios for this crossover, each of which might be applicable in certain regimes. In all cases the vertical axis is internal energy and the horizontal axis is the soft-mode coordinate q. The lower panel shows the usual Landau theory picture in which a paraelectric (PE) parabolic potential evolves into a ferroelectric (FE) double-well potential via a strongly anharmonic single-well potential, with the zero-point energy remaining largely constant. In this scenario, which might be achieved for example by applying pressure or strain, the quantum paraelectric (QPE) regime corresponds to the intermediate strongly anharmonic, but still single-well, potential. The upper panel of Fig. 4.2 shows a complementary limit in which the double-well potential is unchanged across the transition but the zero-point energy shifts. Such behavior could be induced by isotope substitution, with the zero-point energy shifting down as the ionic masses are increased, and QPE would be expected in the region for which the zero-point energy coincides with the top of the double well. A second, methodological goal is to explore whether simple, inexpensive standard DFT-based methods are appropriate for addressing questions that are explicitly related to quantum tunneling of ions. Such a finding would, in turn, allow easy determination of whether new hypothetical materials could exhibit quantum paraelectric behavior.

4.4 Methods & Theoretical Approach

In this section we describe our methodology for calculating the potential wells of the type shown in Fig. 4.2, and solving the resulting Schrödinger equations for these potentials.

4.4.1 Mass-weighted coordinates and the Schrödinger equation

In a first step, we map the multi-atom and three-dimensional tunneling problem onto a single-particle, one-dimensional one with the Schrödinger equation

$$\left(-\frac{\hbar^2}{2m}\frac{d^2}{d\xi^2}+V(\xi)\right)\psi(\xi)=E\psi(\xi). \tag{4.1}$$

(We describe how we extract the one-dimensional potential from the full three-dimensional system in sub-section B below). Solving this equation is numerically trivial given the calculated form of the potential, V, as a function of ionic displacements, ξ, and knowing the masses of the ions, m, contributing to the phonon eigenvector. In practice, however, for the lattice vibrations in *periodic solids* considered here, there is a conceptual subtlety, in that neither the *mass* nor the *displacement* of a phonon is well-defined. Many plausible choices have been made in the literature and we return to this point in sections 4.6.1 and 4.6.2, where we provide a summary of the literature choices and use our results to determine which are most appropriate. Here, we prefer to combine the mass and displacement into mass-weighted coordinates, q, defined as $q=\sqrt{m}\xi$, which are rigorously defined and avoid an arbitrary choice for the phonon mass and displacement. In mass-weighted coordinates, the 1D Schrödinger equation is reformulated as

$$\left(-\frac{\hbar^2}{2}\frac{d^2}{dq^2}+V(q)\right)\psi(q)=E\psi(q) \quad , \tag{4.2}$$

which we then solve to obtain the zero-point and higher energy levels, using a fourth-order finite-difference approach for the second derivative [220] combined with the eigenvalue solver for sparse and square matrices implemented in the python SciPy package [130].

4.4.2 Construction of the potential V(q)

We write the double-well potential $V(q)$ as a fourth-order polynomial

$$V(q) = V_0\left(\frac{q^4}{\sigma^4} - 2\frac{q^2}{\sigma^2} + 1\right) \quad , \tag{4.3}$$

where V_0 is the height of the barrier and σ is the width from the peak of the barrier to the energy minimum of one well, as shown in Fig. 4.3. The "+1" sets the zero of energy to the bottom of the well rather than the top of the barrier. We find that this simple fourth-order polynomial deviates only slightly from a full calculation of the energy as a function of polar distortion over the relevant energy range.

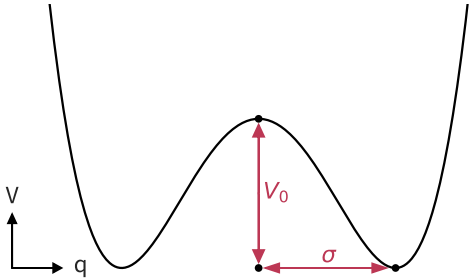

FIGURE 4.3: Sketch of the double-well construction in mass-weighted coordinates, indicating the parameters V_0 and σ. The height of the double well barrier, V_0, is calculated from the energy difference between the polar and non-polar structures. The half-width of the double well, σ, (defined here as the distance between the barrier top and the bottom on one side) is calculated from the imaginary phonon frequency of the non-polar structure at the Γ-point, ω, and the energy difference V_0 as described in the text.

The height of the barrier, V_0, is extracted straightforwardly from the energy difference per formula unit between the non-polar reference structure and the lower-energy polar structure. The half-width of the barrier, σ, is obtained from the frequency, ω of the imaginary phonon at the Γ point as follows: By definition, for a harmonic potential ω^2 is related to the curvature by

$$\omega^2 = \left.\frac{d^2V(q)}{dq^2}\right|_{q=0} \quad . \tag{4.4}$$

(Note that in this case ω^2 is negative). Taking the second derivative of Eqn. 4.3 and setting $q = 0$ yields

$$\left.\frac{d^2V(q)}{dq^2}\right|_{q=0} = -\frac{4V_0}{\sigma^2} \quad , \tag{4.5}$$

and equating Eqns. 4.4 and 4.5 we obtain

$$\sigma^2 = -\frac{4V_0}{\omega^2} \quad . \tag{4.6}$$

We mention that this one-dimensional model corresponds physically to the case where the system inverts its polarization via the high-symmetry zero-polarization reference structure, rather than for example rotating the polarization into another orientation. As such, it provides an upper bound on the barrier height between the oppositely polarized states.

4.4.3 Computational details

To calculate the forces and total energies needed to construct our potentials, we use density functional theory within the generalized gradient approximation (GGA) as implemented in the Quantum Espresso 6.4.1 code [115, 116]. We describe the exchange-correlation functional using the PBE functional [94], which, as already reported for STO [204], gives shallow double wells for both STO and KTO, and perform the core-valence separation with the GBRV pseudopotentials [97, 98]. We use a kinetic energy cutoff of 60 Ry (816 eV) for the wavefunctions, and a Γ-centered 16×16×16 k-point mesh for all unit cells. Total energies are converged to 1 µeV (7.35×10^{-8} Ry) and forces to 0.1 meV/Å (3.89×10^{-6} Ry/Bohr). For comparison, we provide the main results obtained using LDA and PBEsol functionals in Tab. 4.4 of the Appendix.

In a first step, we calculate the lattice constants and internal coordinates of a non-polar reference structure for each material as follows: For BTO we fully relax the atomic positions and lattice parameters to obtain the known experimental low-temperature rhombohedral phase with polarization along the pseudocubic [111] direction; we then remove the polar distortion by hand while keeping the lattice parameters fixed.

For STO, we construct a non-polar tetragonal unit cell containing the experimentally observed rotations of the oxygen octahedra around the [001] direction, then relax the atomic positions and cell parameters while constraining the symmetry to maintain the inversion center. For KTO we relax the lattice constants for the primitive cubic unit cell with the symmetry constraint that the atoms remain at their high-symmetry cubic perovskite positions and the unit cell remains cubic. We then calculate the ferroelectric soft-mode phonon frequencies at Γ for these non-polar reference structures using density functional perturbation theory (DFPT), as implemented in Quantum Espresso 6.4.1. In all cases these frequencies are imaginary (that is ω^2 is negative), indicating a double-well potential.

In a second step, we calculate the polar structures by manually adding a polarization to each material following the eigenvector of the imaginary phonon mode, then relaxing the internal coordinates, while keeping the shape and volume of the unit cells fixed. For BTO, the resulting structure is the original polar structure of the first step. The energy difference between each polar and corresponding non-polar structure gives us directly the V_0 parameter in each case. This is then combined with the calculated ω^2 value to obtain the barrier half-width, σ.

4.5 Evolution from ferroelectric to quantum paraelectric to paraelectric

Next, we present and analyze our calculated potential energy double wells, as well as the zero-point and higher energies obtained from solving the respective Schrödinger equations, for our example materials BTO, STO, and KTO, as well as for experimentally plausible generalized double wells.

4.5.1 Potential and energy trends across the $BaTiO_3$, $SrTiO_3$, $KTaO_3$ series

In Fig. 4.4 we show our calculated potential energies (black solid lines), as well as the two lowest-energy eigenvalues (blue and green dashed lines) for BTO, STO, and KTO. The energy scale is the same for all materials, and each horizontal axis is in mass-weighted coordinates.

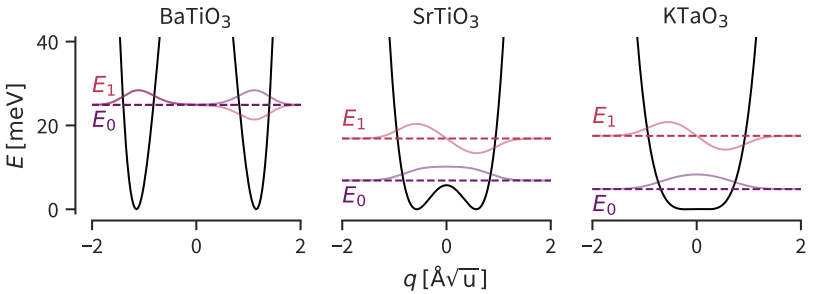

FIGURE 4.4: Ferroelectric double-well potentials of BTO, STO and KTO calculated in this work using density functional theory (solid black lines), and their respective zero-point (dashed blue) and first excited state (dashed green) energies and eigenfunctions (solid blue/green) obtained by subsequent solution of the Schrödinger equation. We note that the trend follows that of the lower panel of Fig. 4.2. In ferroelectric BTO (left), the zero-point energy and first excited state are deep below the barrier of the double-well and almost degenerate (the wavefunction of the first excited state is partially covered by that of the ground state). In quantum paraelectric STO (middle), the zero-point energy is around the same height as the double-well barrier. In KTO (right), the zero-point energy is higher than the double-well barrier, indicating that KTO, while still having quantum paraelectric features, is closer to conventional paraelectric behavior than STO. Corresponding numerical data are given in Tab. 4.1.

We note first that all materials have a double-well potential, with both the height and width of the barrier decreasing from ferroelectric BTO to paraelectric KTO. The barrier height of BTO is ~105 meV, which is high compared to $k_B T$ at room temperature, consistent with its ferroelectric ground state; likewise the lowest energy eigenvalue (dashed blue line)

lies far below the top of the barrier, and its eigenfunction (solid blue line) is largely localized in one or other of the oppositely polarized wells. The energy of the first excited state (dashed green line) is indistinguishable from the zero-point energy at this scale, but they are not degenerate. This small energy splitting means that both states have almost equal probability of being occupied even at low temperature. The resulting linear superposition of the ground and first excited state will be localized in one well or the other with a low tunneling frequency between the wells, consistent with the known ferroelectric ground state of BTO.

The barrier height of STO is more than one order of magnitude smaller than that of BTO, and its width in mass-weighted coordinates is approximately half. The zero-point energy lies just 1.12 meV above the top of the barrier, and the ground-state eigenfunction has its maximum at $q = 0$; this corresponds to the "extreme quantum" regime of Ref. [202]. The splitting between the ground and first excited states is 10.02 meV, much larger than that of BTO, and so at low temperatures most of the system will occupy the lowest state and will be in a centrosymmetric configuration. For the small fraction that forms a linear combination of the lowest and first excited states, and thus has its probability maximum probability at non-zero q, we can extract a "tunneling" or oscillation frequency f from the usual formula for a two-state system [183], $f = \frac{E_1 - E_0}{h}$. For STO, this frequency is 2.42 THz, intriguingly close to the measured 5 K soft-mode phonon frequency of 0.5 THz [63, 221, 222].

While KTO still has a double-well potential for our choice of computational parameters, the barrier is small, and barely visible on the energy scale of Fig. 4.4. The zero-point energy is clearly above the barrier, indicating that KTO should behave more like a conventional paraelectric than STO. The splitting between the ground and first excited states is 12.71 meV, even larger than in STO, and therefore the occupancy of the first-excited state will be even smaller. Most of the system will be in the ground state with its probability maximum corresponding to the centrosymmetric structure, and the tiny fraction that is in a superposition of the ground and first-excited state will evolve with the very high fre-

quency of $f = 3.07$ THz. In this case, it is more appropriate to describe this value as an oscillation rather than a tunneling frequency, since the relevant energy levels are above the barrier. We will discuss these tunneling frequencies in more detail, both for our example materials and more generally, in section 4.5.4.

TABLE 4.1: Calculated double-well half-widths, σ, and barriers, V_0, and resulting energy splittings, $E_1 - E_0$, and energy differences $E_0 - V_0$, of BTO, STO and KTO, corresponding to the double wells shown in Figs. 4.4 (upper three rows of the table) and 4.5 (lower four rows of the table).

	double well		energies [meV]	
	σ [Å$\sqrt{\text{u}}$]	V_0 [meV]	$E_1 - E_0$	$E_0 - V_0$
$BaTiO_3$	1.149	104.8	0.008	−79.94
$SrTiO_3$	0.571	5.74	10.02	1.12
$KTaO_3$	0.215	0.056	12.71	4.75
$SrTi^{18}O_3$	0.591	5.74	9.38	0.91
$KTa^{18}O_3$	0.223	0.056	12.09	4.52
$SrTiO_3$ V.+1 %	0.646	9.52	7.95	−1.10
$KTaO_3$ V.+1 %	0.471	1.35	10.60	3.14

4.5.2 Isotope effect

Our calculated double wells and low-energy eigenvalues and wavefunctions in ^{18}O-substituted STO (top row) and KTO (bottom row) are shown in the left column of Fig. 4.5; the reference data from Fig. 4.4 are shown in the central column. For both STO and KTO we see in the mass-weighted coordinates used here that the heavy-oxygen double well is slightly wider than the reference one, since the heavier oxygen ions result in a lower phonon frequency, ω, for the same forces. This in turn causes lower zero-point energy levels and smaller energy differences between the lowest energy levels. The resulting "oscillation frequencies" (2.27 THz for STO and 2.92 THz for KTO) are $\sim 5\,\%$ smaller than those of the reference cases (2.42 THz and 3.07 THz, respectively).

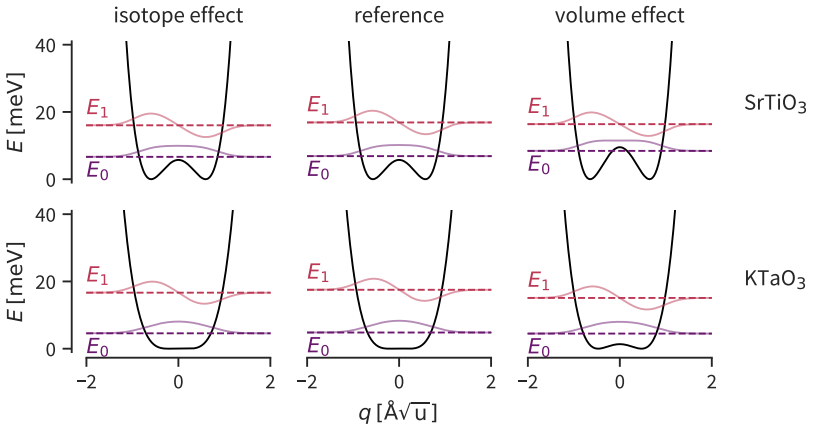

FIGURE 4.5: Double wells and lowest-energy eigenvalues and wavefunctions for ^{18}O-substituted (left column) and 1 %-volume-expanded STO (top) and KTO (bottom). The middle column shows the reference calculations from Fig. 4.4 for comparison. Numerical data are given in Tab. 4.1. We see that heavy-isotope substitution widens the wells, while keeping the barrier heights constant, resulting in a lowering of the zero-point energies and energy differences. The 1 % increase in volume increases the well widths by a slightly larger amount than the ^{18}O substitution and also increases the barrier heights.

These small changes are surprising, in particular for STO, for which strong changes in ferroelectric and superconducting properties have been reported on ^{18}O-substitution [67, 69, 173, 180–182].

4.5.3 Effect of strain

Changes in lattice constant, introduced by applying uniaxial stress, or through biaxial coherent heteroepitaxy, have also been shown to have a substantial effect on both ferroelectric and superconducting behaviors of $SrTiO_3$ [193, 223]. We investigate the effect of strain on the double-well profiles and properties next. In the right column of Fig. 4.5 we show our calculated double wells and energy eigenvalues and eigenfunctions for STO (top) and KTO (bottom) when the volume

of the unit cell is increased by 1 % (without isotope substitution). This corresponds to pseudocubic lattice constants of $a = b = 3.9422\,\text{Å}$ and $c = 3.9613\,\text{Å}$ for STO and $a = b = c = 4.0268\,\text{Å}$ for KTO, which is an increase of slightly more than 0.013 Å for each direction. Note that volume changes of this order have been reported in transition-metal oxides on changing the point defect chemistry by annealing in reducing or oxidizing atmospheres [224]. We find that a volume increase causes changes in the same direction as an increase in isotopic mass, with a 1 % volume increase having a markedly stronger effect than complete $^{16}O \rightarrow {}^{18}O$ substitution. Compared to the reference structure, the barrier height in STO is almost doubled, and the lowest energy eigenvalue lies just below the barrier (by −1.10 meV), indicating that STO moves into the ferroelectric regime under strain. In KTO, the barrier height increases by a factor of 24, and both energy eigenvalues move lower and closer together.

An increase in *lattice constant* (rather than volume) of 1 %, which is accessible in biaxially strained coherent thin-film heterostructures, causes even larger changes (not shown in Figs. 4.5 and 4.6): In STO, the lowest two energy eigenvalues lie below the energy barrier (20.54 meV) and, combined with the σ of $0.765\,\text{Å}\sqrt{u}$, the tunneling frequency is lowered to 1.01 THz, less than half of the reference frequency. In KTO, the changes are even more significant, with a crossover from the oscillating to the tunneling regime occurring. The double well width and height are $0.757\,\text{Å}\sqrt{u}$ and 10.07 meV, giving a tunneling frequency of 1.34 THz, reduced from the reference 3.07 THz.

Since the lattice constants of complex oxides are strongly sensitive to oxygen stoichiometry [224], it is clear that care must be taken in comparing the quantum paraelectric behavior of different STO and KTO samples. In particular, while we note that the only known measurement for STO after isotope substitution does not show any significant change of lattice parameters [191], if the process of isotopic substitution also changes the oxygen vacancy concentration, it might be difficult to disentangle intrinsic isotope effects from changes in behavior resulting from changes in the lattice constant.

4.5.4 Discussion

In Fig. 4.6 we present a map of the "fluctuation frequencies", $f = \frac{E_1 - E_0}{h}$, calculated using our approach for a physically relevant range of barrier heights, V_0, between 0.01 and 1000 meV, and barrier half-widths, σ, between 0.01 and 2.5 $\text{Å}\sqrt{u}$. Our motivation is to provide a convenient chart for looking up the tunneling or oscillation frequency, and hence the proximity to quantum paraelectric behavior, for any material, given the double-well height and width. Frequencies, ranging from high-THz (white) on the left, to low-Hz (black) on the top right, are color-coded from white to black, and the crossover from "tunneling" (zero-point energy $<$ double-well barrier) to "oscillating" (zero-point energy $>$ double-well barrier) is shown by the dashed black line (top left to center right).

Before analyzing our example materials, and discussing the relevance of this quantity for bulk, periodic solids, we first point out some general trends. A narrow free energy barrier (left border) generally results in high oscillation frequencies, and the narrower the well, the higher the barrier required to reach the tunneling regime. Widening the barrier (by increasing σ) lowers the frequency, which can be reduced to the high-GHz range, even for the smallest barrier heights, V_0, shown. At any given barrier half-width σ, increasing the barrier height from close-to-zero first increases the frequency, until the barrier height reaches the zero-point energy; for larger barrier heights the frequency decreases with increasing barrier height. The point where the zero-point energy crosses the double-well barrier, indicated by the dashed line in the plot, therefore corresponds to the frequency maximum and marks the crossover between the oscillating and tunneling regimes. We propose that this crossover provides the best measure of the quantum critical point within the density functional theory formalism.

The solid black symbols show the results of our calculations for BTO, STO, and KTO presented earlier, as well as for an isolated molecule of ammonia, NH_3, the canonical example of molecular quantum tunneling [225, 226], for which we use V_0 and σ values from refs. [227, 228]. The white outlined circle, diamond and square show the results

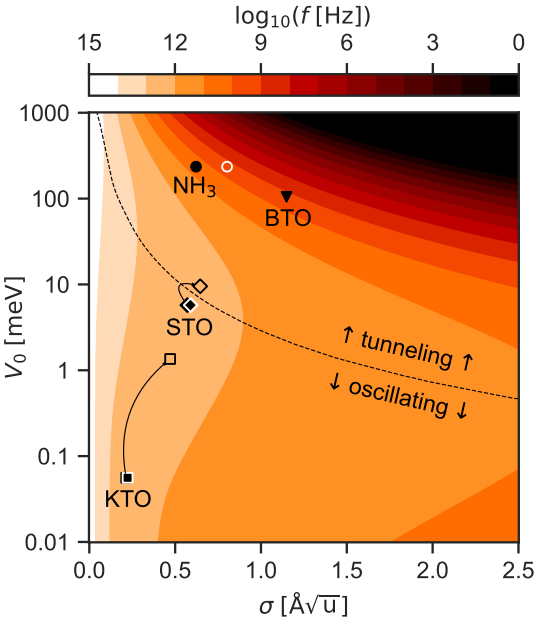

FIGURE 4.6: 2D map of our calculated oscillation/tunneling frequencies (color bar) for quartic double-well potentials with barrier height V_0 ranging from 0.01 to 1000 meV (note the log scale) and barrier half-width, σ less than 2.5 Å$\sqrt{u}$. The black dashed line separates the "oscillating" region (lower left), in which the zero-point energy is above the double-well barrier, from the "tunneling" region (upper right), in which the zero-point energy is below the double-well barrier. Frequencies are color-coded on a logarithmic scale, ranging from white on the left (corresponding to frequencies >100 THz), through orange (THz and GHz) and red (MHz and kHz) to black (<10 Hz). Solid black symbols show the frequency for each material calculated in this work. White open symbols show the frequencies for the corresponding isotope-substituted materials; black open symbols, the frequencies at 1 % increased volumes.

of our calculations for isotope-substituted NH_3, STO, and KTO, in which D is substituted for H in the NH_3 case, and ^{18}O is substituted for ^{16}O in STO and KTO. In the case of the ammonia molecule, the isotope substitution of deuterium for hydrogen moves the zero-point energy substantially lower in the double well, and lowers the tunneling

frequency correspondingly, consistent with experimental observations. In contrast, the small calculated effect of 100 % oxygen isotope substitution that we pointed out earlier is strikingly clear in this visualization. The small oxygen isotope effect is consistent with the small percentage change in mass (only 2 % (3 %) of the mass per formula unit for KTO (STO) or equivalently 12.5 % of the oxygen mass) within the simple model considered here, although it is in striking contrast to the experimental observation of ^{18}O-induced ferroelectricity in STO [191, 192].

Our calculated results for STO and KTO with 1 % volume increase are shown with the black outlined diamond and square, connected to the reference values by black arrows. In both cases the substantial effect mentioned above is clearly visible: For STO, the volume effect leads to a crossover from the oscillating to the tunneling regime; for KTO, there is a strong shift towards tunneling behavior. We emphasize again that even a small volume change during the isotope substitution process will likely overshadow any direct isotope effect, and one has to take special care to exclude this factor when attributing changes in behavior to changes in the masses of the atoms.

We see from Fig. 4.6 that the simple model analyzed here gives a quantitatively correct result for the isolated ammonia molecule. In addition, it appropriately captures the evolution from ferroelectric through quantum paraelectric to paraelectric across bulk, periodic BTO, STO and KTO. It is clear, however, that the low-GHz value of tunneling frequency obtained for BTO does not reflect the rate of spontaneous ferroelectric switching in physical BTO samples, which are stable on time-scales of months or years. Part of this limitation is numerical: A tunneling time of 180 days for BTO, for example, would result from an energy splitting of less than 10×10^{-22} eV. This is smaller than we can resolve with our eigenvalue solver, which is limited to frequencies above around 1 Hz. The limitation is also physical, and reflects the fact that both the $\sqrt{m}$ in our mass-weighted q coordinate as well as the corresponding energy are both the values *per formula unit*. In a macroscopic sample with cooperative behavior between the unit cells like ferroelectric BTO, these values should be scaled by Avogadro's

number, and the resulting value of tunneling frequency, f, is then effectively zero. In practice, reversal of the ferroelectric polarization in BTO takes place via domain wall motion which is not included in our simple model.

Conversely, by scaling the energy barrier and effective particle mass in our model calculations until our calculated tunneling frequencies match experimental optical mode frequencies, we can estimate a length-scale for inter-unit-cell correlations. In the case of STO, the experimental low temperature frequency of $\sim 0.5\,\mathrm{THz}$ [63, 221] is reached from our reference value of 2.27 THz by multiplying V_0 by ~ 2 and σ by $\sim \sqrt{2}$, hinting towards small local polar nano-domains of a couple of unit cells, consistent with recent observations in doped STO thin films [198]. Applying the same procedure to KTO, in which the measured low temperature optical mode frequency is $\sim 0.6\,\mathrm{THz}$ [55, 221], yields a slightly larger four-to-five unit cell estimate.

4.6 Appropriate choices of phonon effective mass and displacement

In this final section, we collect the many definitions that have been used in the literature for the mass of the phonon. We compare the predictions of the various choices with the results that we obtained above using mass-weighted coordinates, for which no arbitrary choice has to be made. Our main finding is that one has to take care when separating mass and displacement in order to obtain physically sensible results. In particular, the popular choice of the B-site ion off-centering as a measure of the polar displacement, while giving accidentally reasonable values for the titanates, is not generally appropriate. For the perovskite oxides, if the full phonon eigenvector is not available, the combination of the mass of the oxygen ions in the unit cell for the effective mass, combined with the average displacement of an oxygen ion between para- and ferroelectric structures as the effective displacement is the most self-consistent choice.

4.6.1 Phonon effective mass

In Table 4.2 we collect the mass values for BTO, STO and KTO for the various definitions that have been used in the literature. All numbers are in units of atomic mass, u.

4.6.1.1 Based only on masses

The definitions in the first six columns in Table 4.2 use only the masses of the constituent atoms.

Column 1 shows the ABO_3 *atomic* mass, which is just the sum of the individual atoms in one formula unit. STO is the lightest at 183.5 u, followed by BTO and KTO with 233.2 u and 268.0 u, respectively. A problem with this definition is that the effective mass is the same for each phonon mode; this is clearly unphysical since different phonons correspond to different patterns of atomic displacements. For example, the heavy barium atom in BTO and tantalum atom in KTO contribute strongly to their respective atomic masses, but do not displace much in the soft mode, which is dominated by motion of the lighter atoms.

A popular choice in the ferroelectrics community is the mass of the B-site atom (column 2), that is titanium (47.9 u) for BTO, and STO [76], and tantalum (180.9 u) for KTO. This choice is motivated by the fact that ferroelectric polarization results in large part from the relative displacement of the B-site cation and its oxygen coordination octahedron. We note, however, that the A-site cation is also displaced from its high-symmetry position in the ferroelectric ground state, and that the cations contribute less to the dynamical displacements in the soft mode than the oxygen anions due to their large mass.

With this in mind, the masses of the lighter oxygens (column 3) probably provide a better definition for the mass of the soft mode in perovskite oxides, since they have the largest displacements in the polar phonons. Their combined mass is coincidentally equal to that of titanium, as already observed by Nakamura et al. [229], possibly explaining why the choice of the Ti mass yields sensible results in perovskite-oxide ferroelectric titanates.

TABLE 4.2: Values of the BTO, STO and KTO phonon effective masses, m^* (in u) for various definitions used in the literature (top three rows). The bottom three rows show the displacement value (in Å) for each mass definition, calculated according to $\delta = \sigma/\sqrt{m*}$, using the σ values that we reported in Table 4.1.

		based only on masses						including eigenvector info.	
		ABO_3	B [76]	O_3 [229]	reduced [230]	AB/O_3 [231]	Wentzcovich [204]	eigenvector [175, 208]	curvature
masses (u)	$BaTiO_3$	233.2	48	48	4.6	38	18	22	0.022
	$SrTiO_3$	183.5	48	48	4.6	35	14	22	0.036
	$KTaO_3$	268.0	181	48	4.6	39	20	22	0.005
displacement (Å)	$BaTiO_3$	0.075	0.166	0.166	0.536	0.186	0.271	0.245	3.65
	$SrTiO_3$	0.042	0.082	0.082	0.266	0.097	0.153	0.122	3.01
	$KTaO_3$	0.013	0.016	0.031	0.100	0.034	0.048	0.046	3.04

The generalized, mode-independent reduced masses [230], defined as $\mu = (\sum_i \frac{1}{m_i})^{-1}$ (column 4) are 4.6 u for all three materials. Since the reduced mass is dominated by the lightest atom, the value will be similar for all perovskite oxides. A recently proposed modified reduced mass [231], $m_{eff} = (\frac{1}{m_A+m_B} + \frac{1}{m_{O_3}})^{-1}$, (column 5) is also dominated by the oxygen ions and gives almost the same value for all three materials considered.

Recently, use of a "Wentzcovich-type" mass, defined as $\frac{3*M_{tot}}{4\pi^2}$ and first introduced in the context of molecular-dynamics simulations with variable cell shape [232] was proposed in the ferroelectrics context [204]. Our values using this formula are shown in column 6 and obviously are smaller than the ABO_3 masses but with the same relative values.

4.6.1.2 Incorporating information about the eigenvectors

The definitions shown in columns 7 and 8 incorporate information about the phonon eigenvector as well as the masses of the atoms.

In the PI-QMC simulations of refs. [175, 208], the pseudoparticle mass was calculated as the sum of each atomic mass times its displacement in the normalized phonon mode eigenvector squared. Interestingly, this eigenvector mass, listed in column 7 for the softest phonon mode in each case, has almost the same value in all three materials, and is almost independent (varying by $< 5\,\%$) of the particular low-energy polar phonon mode at Γ chosen for the calculation.

Finally, a phonon effective mass can be defined by analogy to the electronic effective mass, from the quadratic part of the phonon dispersion around the Γ point, using $m^* = \frac{\hbar^2}{\partial^2 E/\partial k^2}$. (Note that this can not be used for the acoustic modes, which are linear at Γ). We list our calculated values in the final column, noting that they are much smaller than those obtained from all other methods, and also that the precise values are strongly sensitive to the detailed numerics of the phonon calculation.

4.6.1.3 From experiment

Finally, we mention that an effective mass was extracted from experimental measurements of the domain-wall motion near the ferroelectric quantum critical point in TTF-QBr_2I_2, using a simple Wentzel-Kramers-Brillouin approximation [233]. The value extracted in this way is roughly half the proton mass, which is three orders of magnitude smaller than the mass of the TTF-QBr_2I_2 molecule.

4.6.1.4 Summary of phonon effective mass definitions

The preceding discussion clearly illustrates the difficulty with assigning a mass to a phonon, with the physically justifiable values given in Table 4.2 spanning a range of several orders of magnitudes, from less than 1 u to 268 u for the materials considered here. In addition, most of the approaches reviewed assign a mass per formula unit or unit cell, without considering interactions or coupling between unit cells. Since polar nanometer-sized domains have recently been observed in strained STO thin films close to the quantum critical point [198, 234], an appropriate correction could be to multiply any chosen effective mass m_{eff} by a factor corresponding to the number of correlated unit cells [235]. Such an argument was used in ref. [175] to justify a large effective mass, and correspondingly minimal quantum effects, for the antiferrodistortive rotational mode of STO.

4.6.2 Effective displacements

The same argument that precludes an unambiguous definition of phonon mass also results in the phonon displacement not being unambiguously defined. Our results obtained with mass-weighted coordinates, however, allow us to extract the appropriate displacement within the double-well potential model corresponding to a particular choice of the mass. As reported in Table 4.1, our calculated values of σ are 1.15 Å$\sqrt{\text{u}}$, 0.57 Å$\sqrt{\text{u}}$ and 0.22 Å$\sqrt{\text{u}}$ for BTO, STO and KTO respectively. In the lower rows of Table 4.2 we list the calculated displacements, $\delta = \sigma/\sqrt{m^*}$, resulting from these σ values for each choice of mass.

For comparison, in Table 4.3 we list (in Å) the calculated displacement of each individual atom between the high-symmetry centrosymmetric and low-symmetry polar phases, corrected for any shift in the center of mass. For the O_3 and ABO_3 columns, the reported numbers are the average absolute displacement of all ions, with the direction of displacements of the oxygens in ABO_3 being opposite to that of the cations. As expected, the displacement of the lightest oxygen ions is largest in all three materials, although the displacements of the Ti ions in BTO and STO are also substantial, consistent with the usual Slater model of the ferroelectric soft mode. Also as expected, the average displacements are largest for BTO, with its deeper well and largest σ and progressively smaller for STO and KTO. Both the O_3 and ABO_3 values have approximately the same BTO : STO : KTO displacement ratios of ~5.5 : ~3 : 1.

TABLE 4.3: Various definitions of displacement and corresponding values (in Å) for the materials BTO, STO and KTO (all numbers normalized to one formula unit and the center-of-mass motion).

	A	B	O_3	ABO_3
$BaTiO_3$	0.007	0.114	0.139	0.107
$SrTiO_3$	0.016	0.044	0.073	0.056
$KTaO_3$	0.006	0.008	0.026	0.019

Six of the mass choices in Table 4.2 – the O_3, ABO_3, reduced, AB/O_3. Wentzcovich and eigenvector masses – give BTO : STO : KTO displacement ratios close to the ~5.5 : ~3 : 1 pattern identified for the O_3 and ABO_3 displacements of Table 4.3. Of these, the O_3 values give the most consistent match between the two definitions, with the displacements extracted from the ABO_3 mass choice underestimating the ABO_3 displacements in the double well, and all other mass choices providing values that are larger than any of the double-well displacement options. In particular, the tiny effective mass calculated from the phonon dispersion curvature, yields displacements comparable to the size of one unit

cell which are likely unphysically large, even in the strongly fluctuating quantum regime.

To summarize this section, if one is working with a model for polar quantum fluctuations that requires a separation into mass and displacement, then the best choice for the mass is the eigenvector-weighted one, as it provides the closest match with the calculations in mass-weighted coordinates that make no arbitrary mass choice. If the phonon eigenvectors are not available, then the mass of the lightest atoms provides a good approximation, since it correctly captures the dominance of the lightest atoms in the displacements of the soft polar mode. For perovskite titanates, the displacement of the B atom accidentally gives good results, since the mass of the titanium ion is equal to that of the three oxygens. It is not a good choice, however, for general non-titanate perovskites. This finding that the mass of the tunneling entity is best described by the oxygen mass implies that the effective mass shift on $^{16}O \rightarrow {}^{18}O$ substitution should be as large as the change in mass of the oxygens (12.5 %). Note, however, that this is still considerably smaller than the 100 % change on deuteration of ammonia.

4.7 Conclusion

In summary, we find that a simple one-dimensional quantum model, incorporating only two parameters – the energy difference between polar and non-polar structures and the frequency of the soft polar mode in the non-polar structure – can straightforwardly distinguish between ferroelectric, quantum-paraelectric and paraelectric materials. We illustrate the model using conventional DFT and DFPT calculations for the cases of ferroelectric $BaTiO_3$, strongly quantum paraelectric $SrTiO_3$ and weakly quantum paraelectric $KTaO_3$. In addition, we provide a chart that indicates the behavior of any material given the values of these two parameters.

Within our model, we find that experimentally accessible changes in lattice parameter have a strong effect on the shape of the double-well potential and hence the zero-point and low-lying energy levels, and

readily transform STO and KTO from quantum paraelectric to ferroelectric behavior, consistent with experimental observations [66, 187, 193, 236, 237]. Complete isotopic substitution of ^{18}O for ^{16}O, on the other hand, has a minimal effect, in contrast to the reported behavior in $SrTiO_3$ [17, 69, 191, 192]. This could of course be a result of our model's simple description of the quantum mechanical behavior of the ions, although we note that the model accurately captures the change in tunneling frequency on deuteration of ammonia. Therefore, we suggest that care should be taken on interpreting changes in behavior after isotopic substitution in STO and KTO, and in particular that any possible changes in lattice parameters during the oxygen exchange process are accounted for. Here, path-integral quantum Monte Carlo simulations, similar to those of refs. [175, 176, 238], for ^{18}O-substituted STO and KTO, would be invaluable in determining the detailed influence of the oxygen mass increase on the quantum paraelectric behavior. Finally, we summarize the various choices that have been made in the literature for phonon mass and use the results from our calculations in mass-weighted coordinates to determine the corresponding phonon displacement in each case. While we prefer the use of mass-weighted coordinates to avoid such an arbitrary and unphysical separation, we identify some choices which lead to reasonably sensible combinations of mass and displacement, particularly for BTO and STO.

Acknowledgments

This work was funded by the European Research Council under the European Union's Horizon 2020 Research and Innovation Program, grant agreement no. 810451. Computational resources were provided by ETH Zurich and the Swiss National Supercomputing Center (CSCS) under project ID s889.

4.8 Appendix

Here we provide double well properties obtained using LDA and PBEsol functionals for comparison to the ones shown in Table 4.1, which were obtained using the PBE functional.

TABLE 4.4: Calculated double-well barrier half-widths, σ, and barrier heights, V_0, and resulting energy splittings, $E_1 - E_0$, and energy difference $E_0 - V_0$, of BTO, STO and KTO, using LDA and PBEsol functionals. Entries with $V_0 = 0.00$ and no entry for σ have single-well potentials rather than double wells. The main differences from the PBE values of the main text result from slightly smaller lattice parameters which in turn favor the paraelectric states.

		double well		energies [meV]	
		σ [Å$\sqrt{\text{u}}$]	V_0 [meV]	$E_1 - E_0$	$E_0 - V_0$
LDA	$BaTiO_3$	0.647	11.82	7.77	−2.11
	$SrTiO_3$		0.00	9.26	4.63
	$KTaO_3$		0.00	14.60	7.30
PBEsol	$BaTiO_3$	0.856	34.63	1.67	−17.36
	$SrTiO_3$	0.214	0.172	18.18	6.68
	$KTaO_3$		0.00	11.14	5.57

4.9 Data availability

All input data and the core double well program is available here:

Tobias Esswein and Nicola A. Spaldin. Ferroelectric, quantum paraelectric or paraelectric? Calculating the evolution from $BaTiO_3$ to $SrTiO_3$ to $KTaO_3$ using a single-particle quantum mechanical description of the ions. *Materials Cloud Archive* 2022.105 (2022).
DOI: 10.24435/materialscloud:r3-df .

4.10 Additional results: Virtual crystal approximation

Using the same method as presented before, we now look at the phase transition from quantum paraelectric $KTaO_3$ (KTO) to ferroelectric $KNbO_3$ (KNO) using the so-called *virtual crystal approximation* (VCA). This transition has been well-studied since the 1980s as a prime example of a paraelectric to ferroelectric phase transition [239–241]. Tantalum and niobium are of roughly the same size and have the same valence charge, nevertheless their respective potassium perovskite-structure oxides differ vastly in their polar properties: As we already know, KTO stays cubic and (quantum) paraelectric down to zero kelvin, whereas KNO undergoes three phase transitions to ferroelectric states, similarly to BTO [241]. This behavior has been attributed to a large difference in the way that the O-2p orbitals hybridize with the Ta/Nb-d orbitals [241–243]. We chose this system because crystals can be grown experimentally over the whole composition range [241], providing data to compare against, and because Ta and Nb are chemically similar, allowing us to test the suitability of the virtual crystal approximation for our model.

The virtual crystal approximation, first described in 1931 [244], is a method in which a real atom is replaced by a virtual atom, which is constructed in the context of DFT by a linear combination of the pseudo potentials of two or more individual atoms. It is a widely used method in DFT calculations [245–247], and has been shown to successfully describe dielectric and piezoelectric properties of perovskite alloys [248–250].

Here, we calculate the lattice properties and double well characteristics of the phase space between pure KTO and pure KNO in steps using the VCA, and compare it to two calculations of comparable alloy values within $2 \times 2 \times 2$ supercells. To simplify the comparison, we calculate all properties in the rhombohedral structure, which is the experimental lowest-energy structure for KNO. Using the relaxed lattice constants calculated with the PBE functional, the lowest-energy structure of KTO is rhombohedral as well, as indicated by the imaginary phonon

frequency at Γ of cubic KTO in the published work above. The main results of these calculations are summarized in figure 4.7, which has the same layout and color scale as figure 4.6.

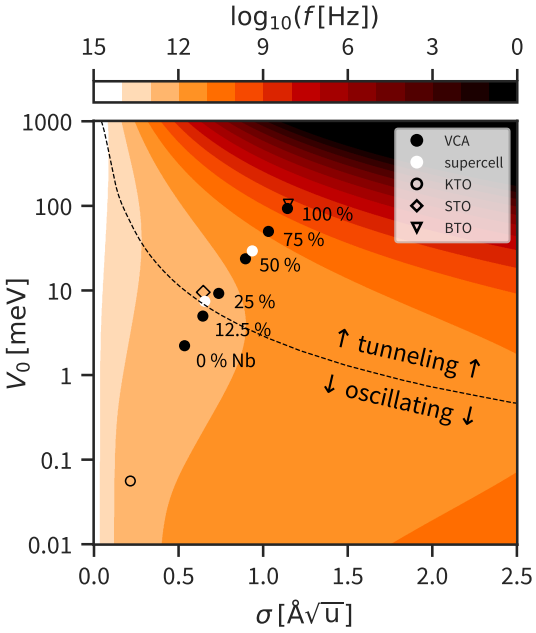

FIGURE 4.7: 2D map of our calculated oscillation/tunneling frequencies (color bar), the same as in figure 4.6. Solid black circles show the evolution from pure $KTaO_3$ to pure $KNbO_3$ using the virtual crystal approximation (VCA). Solid white circles show the results of the corresponding supercell calculations with 12.5 % and 50 % niobium content, respectively. The black open symbols serve as reference points for comparison with figure 4.6.

Black open symbols show the original results for KTO, STO and BTO from figure 4.6 and serve as reference for comparison. The solid black circles show the new results, namely the double well characteristics of the phase space from KTO to KNO in four steps. The solid white circles show the results of the two $2 \times 2 \times 2$ supercell calculations we made, one at 12.5 % Nb with one niobium in the supercell, and one at 50 % Nb with tantalum and niobium ions arranged regularly in a

three-dimensional checkerboard pattern within the supercell. The white dots are very close to their VCA counterparts with the same alloy level, suggesting that the VCA is a reasonable way to approximate this system. We also find that various geometric properties (not shown here) are quite similar between VCA and supercell structures.

One can clearly see that a crossover from the (quantum) paraelectric *oscillating* to the more ferroelectric *tunneling* regime occurs as the percentage of niobium is increased, with pure KNO lying very close to BTO. The crossover takes place just above 12.5 % Nb, which is a higher value than that of the experimentally observed transition at around 1 % [241]. There is no simple explanation for this shift, but the easiest way to tune the calculation results towards the experimental ones would be the application of small negative hydrostatic pressure, which slightly enlarges the unit cells. Additionally, the pure KTO value shown here sits much closer to the transition line compared to the KTO of figure 4.6, because here we allowed KTO to relax into its lower-energy rhombohedral structure, increasing both the barrier height V_0 and the double well width σ. This large shift in properties, caused by only a small change in lattice geometry (from KTO to KNO, the rhombohedral angle shrinks from 89.97° to 89.80°, while the lattice constant grows from 4.02 Å to 4.06 Å), emphasizes again how sensitive the quantum paraelectric properties are to small differences in the lattice parameters.

The KTO–KNO system could be a very interesting one to also test superconductivity on surfaces, as the materials are perfectly mixable, and a small addition of niobium tunes KTO towards the quantum critical point, potentially enhancing the superconducting T_c. To get a better idea of the potential properties of this system at very low doping, one could build on the results presented here, by first testing the VCA against larger and differently ordered supercells, and then by calculating the properties at very low doping values around the experimental transition concentration of $\sim$ 1 at.-% Nb, a regime conventional supercells can not easily reach.

4.11 Summary and Outlook

From this chapter, we have learned several things. The first and probably most important one is that defining the quantum critical point in a quantum paraelectric is more difficult than initially expected. The exact definition is not clear, and different models to describe the quantum fluctuations have been used in the past, some of which only accidentally worked reasonably well for titanates. Within our model, probably the best definition of the quantum critical point is the point at which the zero-point energy (ZPE) crosses the double-well barrier. If the ZPE lies *above* the double-well barrier, the maximum of the quantum-mechanical observation probability is centered and a non-polar structure results. If the ZPE lies *below* the double-well barrier, the observation probability has two non-centered maxima, indicating the crossover to a preferably polar structure.

There are several possible ways of extending this model to capture more of the properties of the real system. One idea is to extend the model to two dimensions, allowing the ions to tunnel not only through the barrier, but also around it, similar to the Mexican-hat like potential observed e.g. in hexagonal manganites [251, 252]. Nudged-elastic band (NEB) calculations [253] could be very useful for that, as they are effective in calculating the lowest-energy path and saddle points between two energy minima. Another idea could be to study systems with imaginary phonon modes that do not sit at Γ, allowing one to capture e.g. the alternating antiferroelectric ordering that corresponds to using a zone-boundary phonon [254]. Finally, as already mentioned in the main text, path-integral quantum Monte-Carlo simulations of the isotope effect in STO would be important to check if the predictions of our model, namely that the isotope effect is much smaller than expected, can be reproduced or not.

A NOTE ON LINEAR AND ANGULAR FREQUENCIES

Experimental phonon frequencies are usually given as linear frequencies ν with units THz, or $1/s$. The phonon frequencies in the output of Quantum Espresso (from dynmat.x or matdyn.x) are given with units THz and cm^{-1}, and called ω, which is usually an angular frequency with the unit $2\pi/s$. This would lead to the naive conclusion that one can use the calculated frequencies directly in a Schrödinger equation, which requires angular frequencies, and one has to multiply experimental frequencies with 2π to match with the calculated frequencies. Unfortunately, the quantity called ω in the output of QE is actually the linear frequency ν with the unit $1/s$ and not the angular frequency ω with the unit $2\pi/s$ – something which had already been noticed in 2012 [255], but, at the time of writing, has not been corrected in the output. Therefore, when working with phonon frequencies and Schrödinger equations, one should always keep this difference in mind and pay special attention to dimensionless factors of 2π.

5

Electron-phonon coupling in $KTaO_3$

5.1 Preface

Research on superconductivity in $KTaO_3$ has seen a surge in the past two years, as there have been several experimental reports of superconducting critical temperatures reaching up to 2 K since 2021 [72–74], clearly surpassing the previous number of 0.05 K in KTO [70], and even the 0.6 K observed in more quantum paraelectric STO [31, 256].

The coupling between electrons and phonons plays a key role in all established theories of superconductivity, from early BCS theory [23] to the more recent Eliashberg theory [29, 30]. The issue with KTO and also STO is that these theories are not directly applicable, mainly because one main assumption in these systems is not valid: the so-called Migdal criterion [68, 257] is not fulfilled. This criterion states that the factor ω_D/ϵ_F must be small, which is the case for most superconductors, but not for quantum paraelectric STO and KTO. Quantum fluctuations push the ferroelectric soft phonon mode up in frequency, and superconductivity can be observed at very low doping, so that ω_D/ϵ_F can become rather large [67]. This poses a particular problem for STO, where superconductivity has been observed at doping levels down to 5×10^{17} e/cm^{-3}.

The detailed electron-phonon coupling spectrum of STO was calculated in 2018 [258]. The work focused on transport properties and showed that the unusual electron mobility in STO can be attributed to the higher-energy LO modes and the ferroelectric soft mode, both of which are discussed as being relevant for superconductivity [67, 182, 259, 260].

Such calculations were previously lacking for KTO, so motivated by the recent measurements of surface and interface superconductivity in KTO [72–74], we present in this chapter the calculated electron-phonon coupling strength in KTO.

Before presenting our results, I address the question of why we perform our calculations for bulk KTO, rather than for KTO slabs with surfaces, which would resemble the experimental systems more closely. The main reason for this is computational cost: the calculation of electron-phonon coupling properties is quite expensive. To give an example, one complete EPW calculation of a five-atom KTO unit cell with a coarse k mesh of $24 \times 24 \times 24$ and a coarse q mesh of $4 \times 4 \times 4$ (the standard meshes we use in the paper, resulting in one panel of figure 5.2) needs $\sim 25'000$ core hours, which corresponds to more than two days on four nodes on Euler, the high-performance computing cluster of ETH Zurich. While this may seem like a reasonable amount of time, increasing the phonon mesh to just $8 \times 8 \times 8$ roughly doubles the required resources, mainly because the phonon calculation now needs $\sim 26'000$ core hours instead of just $\sim 1'300$, resulting in almost 5 days total computation time. Using parallelization and more than four nodes (with 128 cores each) may seem like a quick fix for this problem, but unfortunately EPW does not scale well beyond ~ 600 cores, so four to five nodes is the maximum above which no reasonable gain is achieved, at least with our current software setup.

From this it can be seen that the calculation of slabs with several unit cells of KTO and lower symmetry of the overall system due to the surface would quickly take months and more, optimistically assuming that no additional issues arise due to the larger system. This leaves us for now with the computational results for bulk KTO as presented in this chapter, which provides insight into possibly coupling mechanisms, in spite of not addressing directly the anisotropic surface superconductivity.

Explanatory Remarks

The following section is available as preprint:

Tobias Esswein and Nicola A. Spaldin. First-principles calculation of electron-phonon coupling in doped $KTaO_3$. *arXiv* 2210.14113 (2022). DOI: 10.48550/arXiv.2210.14113.

—

Minor changes have been made to formatting of text and figures to adapt to the layout of this thesis, in compliance with the CC BY SA 4.0 license of the preprint.

5.2 Abstract

Motivated by the recent experimental discovery of strongly surface-plane-dependent superconductivity at surfaces of $KTaO_3$ single crystals, we calculate the electron-phonon coupling strength, λ, of doped $KTaO_3$ along the reciprocal-space high-symmetry directions. Using the Wannier-function approach implemented in the EPW package, we calculate λ across the experimentally covered doping range and compare its mode-resolved distribution along the [001], [110] and [111] directions. We find that the electron-phonon coupling is strongest in the optical modes around the Γ point, with some distribution to higher k values in the [001] direction. The electron-phonon coupling strength as a function of doping has a dome-like shape in all three directions, and is largest in the [001] direction and weakest in the [111] direction. This is in contrast to the experimentally measured critical temperatures, which are highest for the (111) plane, pointing to a non-BCS character of the superconductivity. The strong localization of λ in the soft optical modes around Γ suggests an importance of ferroelectric soft-mode fluctuations.

5.3 Introduction

Perovskite-structure potassium tantalate ($KTaO_3$, KTO) exhibits many interesting phenomena, resulting from its high dielectric constant [76], strong spin orbit coupling [261] and charged ionic layers [262]. The

strong spin-orbit coupling (SOC), caused mainly by the heavy tantalum ion, leads to a band splitting of up to 400 meV [261, 263] and possible applications in spintronic devices [78, 81]. The high dielectric constant, associated with a quantum paraelectric state [17] similar to that of $SrTiO_3$ (STO) [18], indicates proximity to ferroelectricity, and is predicted to yield a large strain-dependent Rashba spin splitting [79]. The need to compensate the alternating charged ionic layers at the surfaces is predicted to induce lattice polarization in thin films [264], and leads to the accumulation of compensating charges at the surfaces of bulk samples [262]. The origin and nature of the compensating charge are still open questions, with reports of conducting two-dimensional electron gases (2DEGs) [80, 265], charge-density waves and strongly-localized electron polarons [266], and terrace-like structures of alternating termination [267], depending on the annealing atmosphere and temperature.

Perhaps the most intriguing behavior of KTO, is its recently discovered low-temperature superconductivity on electron doping [70]. Superconductivity was first achieved using ionic liquid gating on the (001) surfaces of KTO single crystals, for which critical temperatures of up to 50 mK were found at 2D doping concentrations of between 2×10^{14} and 4×10^{14} cm^{-2} [70, 71]. Note that these values correspond to 3D doping concentrations of approximately 4.1×10^{20} cm^{-3} to 1.2×10^{21} cm^{-3}, considerably higher than the $\sim 1.4 \times 10^{20}$ cm^{-3} possible using chemical doping with barium in bulk KTO [82]. (For the conversion between 2D and 3D carrier concentrations see Ref. [70] and the Appendix). A subsequent study of $LaAlO_3$-capped KTO (110) surfaces, with 2D doping concentrations of 7×10^{13} cm^{-2}, reached markedly higher critical temperatures up to 0.9 K [72]; (111)-oriented KTO interfaces with either EuO or $LaAlO_3$ showed even higher T_cs of up to 2.2 K at similar carrier concentrations [73]. Note that no superconductivity was found down to 25 mK at (001)-oriented KTO interfaces at these lower carrier concentrations [73]. More recently, in an ionic liquid gating setup similar to that of Ref. [70], but at lower 2D doping densities of around 5×10^{13} cm^{-2}, superconductivity was found at the (110) and (111) surfaces with T_c of around 1 K and 2 K respectively, and not at the (001) surface down to 0.4 K [74]. The reported critical temperatures from the literature are collected as a function of carrier concentration in figure 5.1.

The mechanism underlying the superconductivity, as well as its strong and unusual dependence on the orientation of the surface or interfacial plane, are not yet established. Indeed, even in the related quantum paraelectric STO, in which superconductivity was found more than half a century ago [31, 268], the pairing mechanism remains a subject of heated debate (for a recent review see Ref. [67]). While the persistence to low carrier concentrations [268] and the anomalous isotope effect [69] challenge conventional BCS theories [23, 179], it is likely that electron-phonon coupling in some form, as well as proximity to ferroelectricity [35, 180–182, 269, 270] play a role. Spin-orbit coupling has also been implicated [271–274], and would be consistent with the observed higher critical temperatures in KTO, with its heavy tantalum ion, compared to STO [85, 269, 270]. The surface-plane dependence in KTO is captured by a model in which out-of-plane polar displacements of the Ta and O ions allow a linear coupling of the transverse optical (TO) phonon to the electrons in the t_{2g} orbitals (d_{xy}, d_{yx} and d_{zx}); this coupling would otherwise go to zero as q approaches Γ [84]. The strong dependence of the superconducting T_c on surface orientation is then explained by different inter-orbital hopping of electrons between adjacent tantalum sites via the oxygen orbitals, with the highest hopping at (111) surfaces, followed by (110) surfaces, and no hopping allowed by symmetry at (001) surfaces.

It is clear that a thorough picture of the electron-phonon coupling (as a function of electron doping and throughout the Brillouin Zone) in KTO is an essential step towards developing a complete theory of its superconductivity. While the electron-phonon coupling has been calculated from first-principles for STO [258], to our knowledge it is lacking for KTO, and the goal of this work is to remedy this gap. Here we report the mode-resolved electron-phonon coupling strengths, λ, obtained using first-principles calculations based on density functional theory, for cubic $KTaO_3$ across the range of experimentally accessible electron doping values. We extract the mode-resolved total λ as a function of carrier density, and focus in particular on differences between the [001], [110] and [111] high-symmetry directions, which are reciprocal to the experimentally measured surface and interfacial planes. Our main findings are that the calculated total electron-phonon coupling strengths

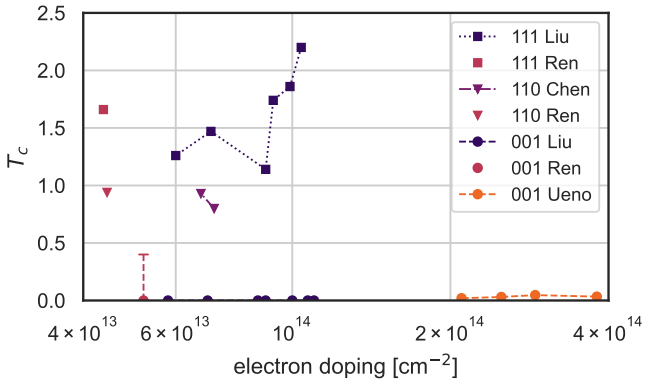

FIGURE 5.1: Superconducting critical temperatures, extracted from references by Ueno et al. [70], Chen et al. [72], Liu et al. [73], and Ren et al. [74]. One can see that the (111) surface/interface reaches the highest T_c of up to 2 K, followed by the (110) surface/interface reaching almost 1 K. While the original paper by Ueno et al. [70] reported T_c up to 0.05 K at high doping, more recent publications were not able to reproduce this at lower doping, down to 0.025 K [73] and 0.4 K [74].

do not follow the measured trends in superconducting T_c, and that a concentration of λ around Γ suggests a mechanism involving the polar soft mode.

5.4 Methods

To calculate the forces and total energies we use density functional theory within the generalized gradient approximation (GGA) as implemented in the Quantum ESPRESSO 7.0 code [115–117]. We describe the exchange-correlation functional using the PBEsol functional [95], and perform the core-valence separation with the ultrasoft GBRV pseudopotentials [97, 98]. We use a kinetic energy cutoff of 60 Ry (816 eV) for the wavefunctions and a $24 \times 24 \times 24$ k-point mesh including Γ for all unit cells. Doping is achieved in the range from 0.0001 to 0.1 electrons/formula unit (e/fu) using the background-charge method with

Gaussian smearing of 1 meV width. Total energies are converged to 1 µeV (7.35×10^{-8} Ry) and forces to 0.1 meV/Å (3.89×10^{-6} Ry/Bohr).

Both unit cell size and shape, as well as internal coordinates, are fully relaxed, resulting in a non-polar cubic perovskite structure with a lattice constant of 3.988 Å, which is very close to the experimental one of 3.989 Å [275]. Phonons are calculated on a $4 \times 4 \times 4$ q-point mesh, with convergence tests on $6 \times 6 \times 6$ and $8 \times 8 \times 8$ q-point meshes showing only minor differences (see appendix on page 109). The resulting phonon dispersion for very low doping, using the PBEsol-relaxed unit cell, corresponds well with the room-temperature phonon dispersion calculated recently using Quantum Self-Consistent Ab Initio Lattice Dynamics (QSCAILD), which is based on DFT and a self-consistent sampling method to capture both thermal and quantum fluctuations [276].

The electron-phonon coupling properties are calculated using the EPW 5.4.1 code [105, 109], which is included in the Quantum ESPRESSO package. The relevant electronic bands in $KTaO_3$ are the three Ta-5d t_{2g} bands, which are reproduced using maximally localized Wannier functions as implemented in the Wannier90 code [277], used internally by EPW. The electron-phonon matrix elements are first calculated on coarse $24 \times 24 \times 24$ k-point and $4 \times 4 \times 4$ q-point meshes and then interpolated onto fine grids using maximally localized Wannier functions. We use a random fine mesh with 1'000'000 k points to calculate the mode-resolved electron-phonon coupling strengths, $\lambda_{q\nu}$, along a path between cubic high-symmetry points with 200 q points between each point. Convergence test results can be found in the appendix on page 109.

5.5 Results and Discussion

Our calculated mode-resolved electron-phonon coupling strengths λ at seven different doping levels are shown in figure 5.2, with λ integrated over each q point shown in the top part of each subplot, and λ integrated over frequency (decomposed into 100 frequency bins) shown on the right of each subplot. The doping range spans from 0.0001 e/fu to

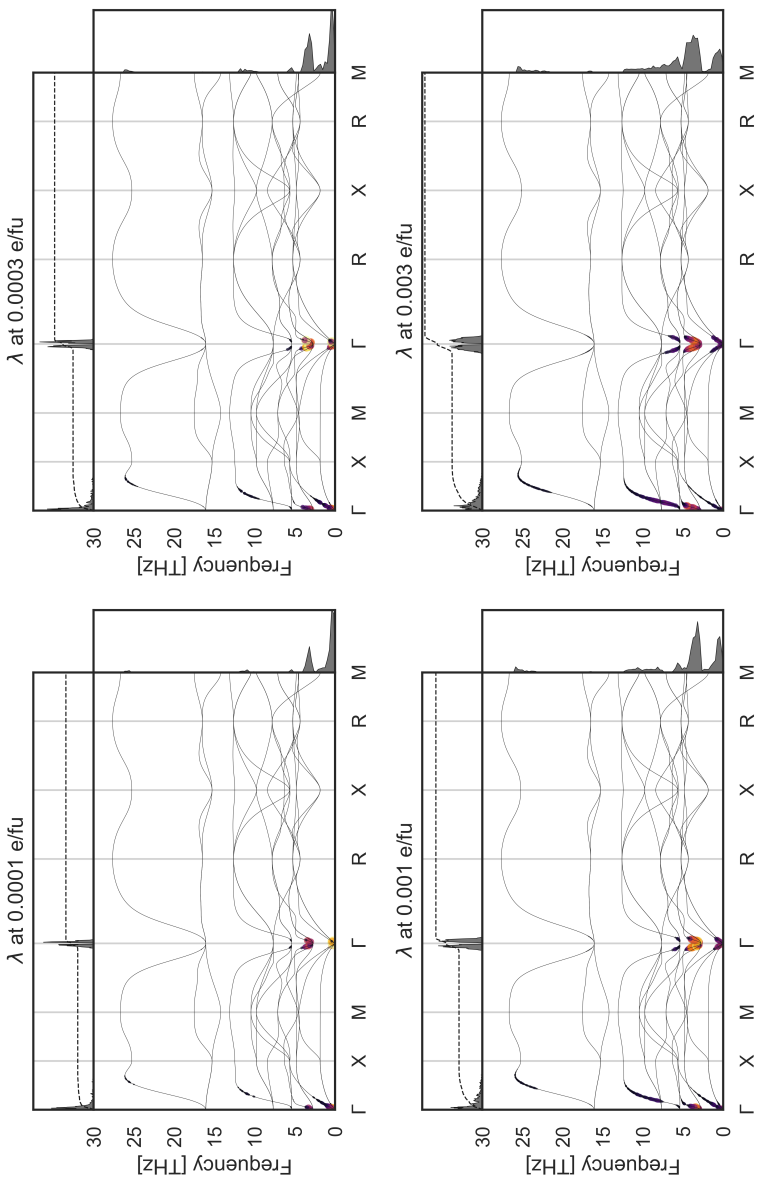
λ at 0.0001 e/fu
λ at 0.0003 e/fu
λ at 0.001 e/fu
λ at 0.003 e/fu
Frequency [THz]
0
5
10
15
20
25
30
Γ X M Γ R X R M

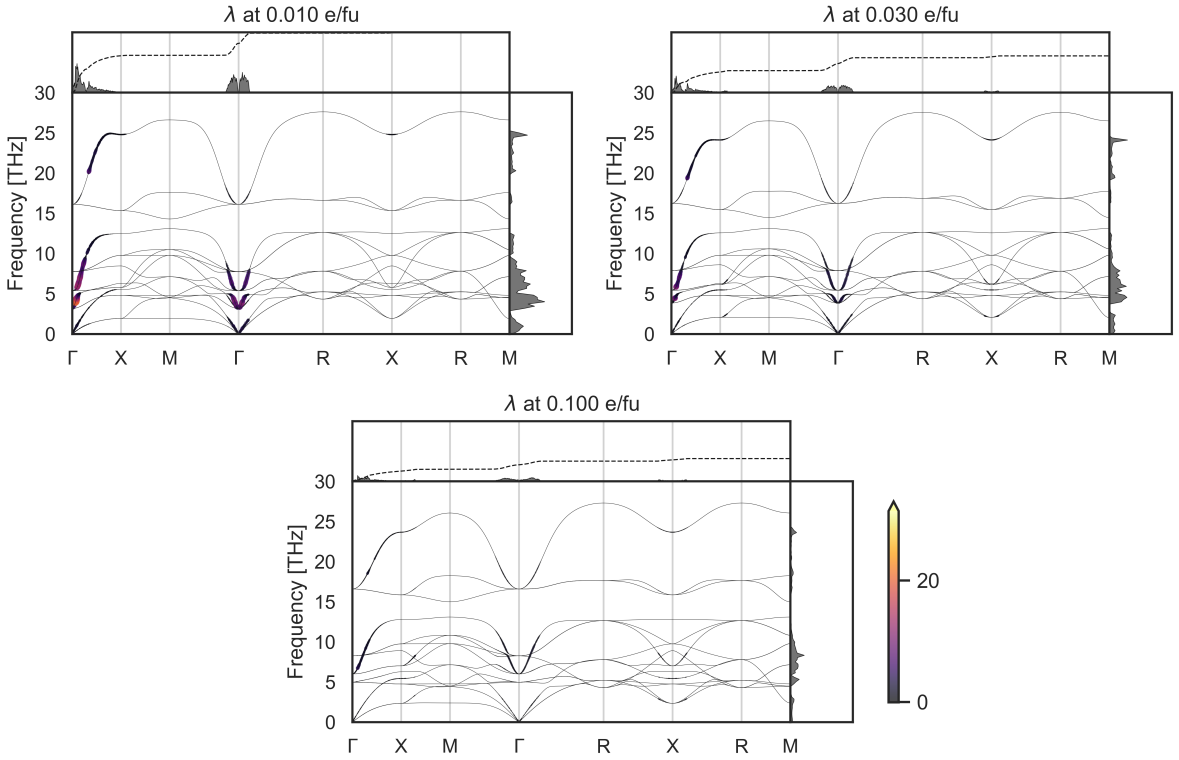

FIGURE 5.2: Phonon-mode-resolved electron-phonon coupling strength λ at different doping values ranging from 0.0001 e/fu to 0.1 e/fu, which correspond to 1.6×10^{18} e/cm^3 to 1.6×10^{21} e/cm^3 or roughly 6.2×10^{12} e/cm^2 to 4.7×10^{14} e/cm^2. All plots share the same colorbar for the dimensionless λ, shown at the bottom.

0.1 e/fu, corresponding to 1.6×10^{18} e/cm^3 to 1.6×10^{21} e/cm^3 (3D) or roughly 6.2×10^{12} e/cm^2 to 4.7×10^{14} e/cm^2 (2D), which covers the whole experimental doping range.

There are several points to note. First, there are no imaginary frequencies, as the structural relaxation of KTO using the PBEsol functional results in a cubic unit cell with no structural instabilities. The frequency of the polar soft mode at Γ, which can be imaginary using the PBE functional, is 2.7 THz for the lowest doping value of 0.0001 e/fu, and hardens to 5.0 THz at the highest doping value of 0.1 e/fu. It has the strongest electron-phonon coupling strength λ throughout the whole doping range. Additionally, contributions to λ can be seen in the higher-energy optical modes around Γ. The strong coupling of the electrons to the polar modes at the Γ point suggests that the ferroelectric fluctuations associated with quantum paraelectricity could play a key role in the superconductivity in KTO, as already suggested for quantum paraelectric STO [35, 67, 182].

In the [110] (Γ to M) and [111] (Γ to R) directions, the electron-phonon coupling occurs only close to the Γ point; here the optical phonons correspond to long-wavelength ferroelectric displacements. In the [001] Γ-X direction, in contrast, the coupling, while strongest close to Γ, remains present along the entire high-symmetry line, also at higher doping. This results also in a larger total contribution along the [001] direction than along [110] and [111]. We note that the form of λ in reciprocal space closely follows that of the Fermi surface, which at these doping levels is close to spherical except for elongations along the cartesian reciprocal axes reflecting the flat electronic bands along Γ to X (see e.g. fig 3.3 of Ref. [278]). As expected, at low doping, the electron-phonon coupling is limited largely to the lowest phonon frequencies, then extends to higher frequencies as the doping is increased and higher energy electronic bands are populated.

The calculated integrated λ values along the three high-symmetry directions, which we use as proxies for the total electron-phonon coupling strength in each reciprocal direction, are shown as a function of doping concentration in figure 5.3.

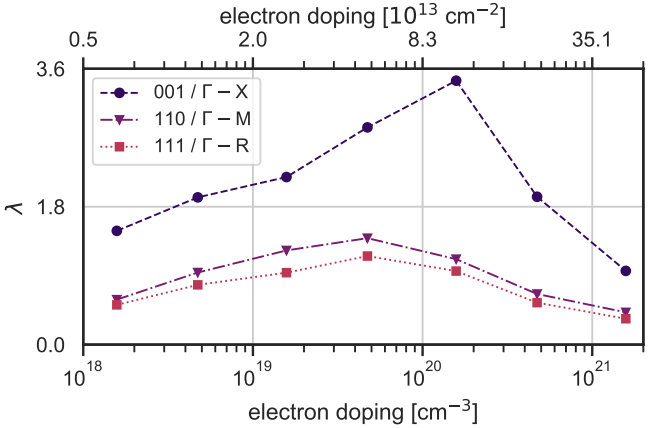

FIGURE 5.3: Total electron-phonon coupling strength λ integrated along each high-symmetry direction at different doping values, covering a range from low concentration to the maximum achieved by ionic liquid gating [70]. The numbers on the left axis correspond to the mean lambda value of each point along each high-symmetry direction. The 2D doping values on top are estimated from the 3D values on the bottom axis using the a conversion method described in the appendix (see fig. 5.4). The strongest electron-phonon coupling is along the [001] direction, while the [110] and [111] directions have almost the same magnitude and evolution with doping.

In all directions in reciprocal space there is a dome-like structure in the calculated λ, with a smooth maximum between 1×10^{19} e/cm^{-3} to 1×10^{20} e/cm^{-3} (2.0×10^{13} e/cm^{-2} to 8.3×10^{13} e/cm^{-2}) for the [110] and [111] directions. The more pronounced peak around 1×10^{20} e/cm^{-3} in the [001] direction coincides with the electron doping reaching the X point of the phonon band structure, as can also be seen in figure 5.2. The experimental data do not show such a dome-like trend, with the (111) surfaces/interfaces in particular showing a linear increase of T_c with increasing doping.

If KTO were a classical BCS theory superconductor, we would expect the critical temperatures of figure 5.1 to follow roughly the electron-phonon coupling strength of figure 5.3. Comparing these two figures, it

is obvious that there is no observable correlation. While experimentally the highest T_c is observed for the (111) surfaces/interfaces, and the T_c for the (001) surfaces/interfaces is very low, the electron-phonon coupling is strongest for the [001] direction, and weakest for the [111] direction.

Summary

In summary, we have presented the calculated electron-phonon coupling in $KTaO_3$ as a function of electron doping between 1.6×10^{18} e/cm^3 and 1.6×10^{21} e/cm^3 and analyzed the results in light of the recently reported superconductivity and its surface dependence. Our calculations indicate that the measured trends in superconducting T_c are not reflected in the calculated electron-phonon coupling strengths λ, confirming earlier suggestions that the superconductivity is not BCS-like in nature [17, 71, 73, 279]. The concentration of λ in the lowest frequency optical modes close to Γ hints towards a mechanism in which the polar soft mode plays a role.

Acknowledgments

This work was funded by the European Research Council under the European Union's Horizon 2020 Research and Innovation Program, grant agreement no. 810451. Computational resources were provided by ETH Zurich and the Swiss National Supercomputing Center (CSCS) under project ID s1128.

5.6 Data availability

All input data is available on the materialscloud archive at DOI: 10.24435/materialscloud:7z-wx .

5.7 Appendix

This chapter contains data and information on the charge carrier conversion and numerical convergence of the calculations presented in the main text.

Conversion between 2D and 3D carrier densities

The interpolation used for conversion between n_{2D} and n_{3D} carrier densities is shown in figure 5.4. It is based on data from figure S6 of the supplementary information of Ref. [70].

The corresponding interpolation formula is

$$n_{3D} = 6.1078 * 10^{-3} * n_{2D}^{1.5960} \quad .$$

According to this conversion, a 3D carrier concentration of 1.4×10^{20} cm^{-3} corresponds to 1.0×10^{14} cm^{-2}, and 2×10^{21} cm^{-3} to 5.4×10^{14} cm^{-2}.

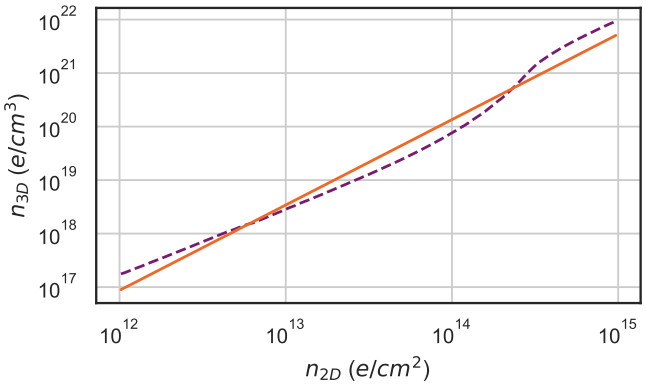

FIGURE 5.4: Interpolation used for conversion between n_{2D} and n_{3D} carrier densities (solid line), based on data for KTO from figure S6 of the supplementary information of Ref. [70] (dotted line). The corresponding interpolation formula is $n_{3D} = 6.1078 * 10^{-3} * n_{2D}^{1.5960}$.

Decay properties in real space

The spatial decay of the electron-phonon matrix elements in real space for different q-meshes is shown in figure 5.5 (see Refs. [109] and [110] for more details). We observe a decay of the phonon perturbation of almost three orders of magnitude using the q4 mesh, and a flattening after, without a lowering in absolute numbers, using the q6 and q8 meshes, indicating that the q4 mesh is enough for the qualitative comparison we make. The decay of the electronic Wannier functions is well-converged using the $24 \times 24 \times 24$ coarse k-point mesh, as can be seen from the bottom right panel of figure 5.5.

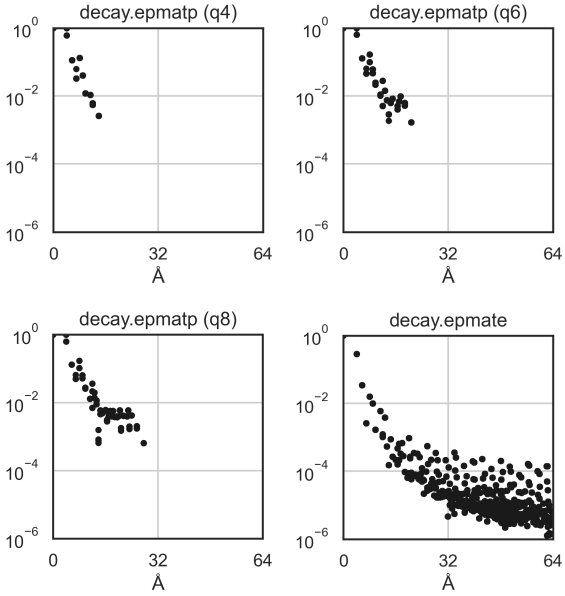

FIGURE 5.5: Decay of the electronic Wannier functions and phonon perturbation part of the electron-phonon matrix elements in real space for $4 \times 4 \times 4$ (q4), $6 \times 6 \times 6$ (q6) and $8 \times 8 \times 8$ (q8) q meshes (top left, top right and bottom left). The electronic part (bottom right) is the same in all cases and well converged using a $24 \times 24 \times 24$ k-mesh.

Convergence with coarse q mesh

To test the convergence of our results, we calculate the phonons and the electron-phonon coupling strength λ along the same high-symmetry path based on different q-meshes, with results shown in figure 5.6. The phonon frequencies themselves at the high-symmetry points are well converged, there are only minor variations in between due to the interpolation method used. The colorscale in each plot is adjusted to each respective maximum λ value and not directly comparable with the one of fig. 5.2, to highlight the relative similarity of the λ values. The actual λ values increase by roughly a factor of two in the q6 and q8 cases, as visible from the integrated values in the top and side panels of each plot.

5.8 Summary and Outlook

We can draw two conclusions from this chapter: On the one hand, there is no correlation between the electron-phonon coupling strength λ and the surface dependence of the experimentally observed superconducting T_c, at least when using the reciprocal directions of bulk KTO as proxies for surface orientation. This indicates that the BCS theory is not sufficient to describe superconductivity in KTO. On the other hand, the strong localization of λ around Γ at the polar soft mode points to ferroelectric fluctuations as possible facilitators of superconductivity.

Computationally, a few things could be done to improve the quantitativeness of our reported results, and to gain more insight into the surface-termination dependence of KTO superconductivity.

One obvious next step would be the inclusion of spin-orbit coupling (SOC) into the EPW calculations, increasing in computational cost by a factor of five to eight. Spin-orbit coupling and Rashba coupling have been suggested as relevant for enabling the coupling of the ferroelectric soft mode to the electrons in incipient ferroelectrics [270]. The main effect of SOC on the electronic bands is an electronic band splitting at the bottom of the conduction band of around 400 meV. This affects the

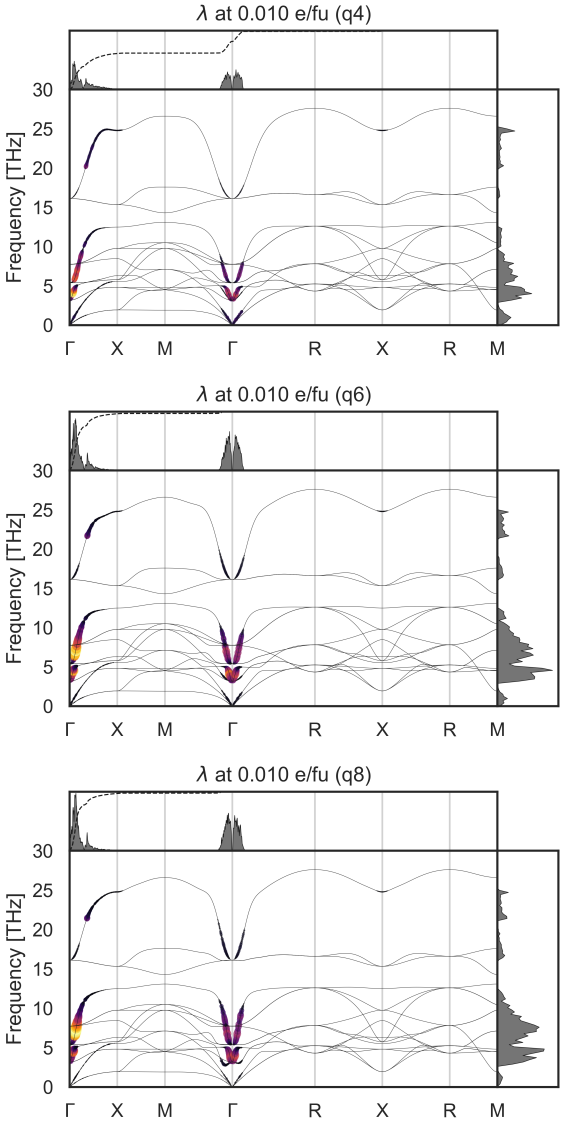

FIGURE 5.6: Phonon dispersion and mode-resolved electron-phonon coupling strength λ at a doping level of 0.01 e/fu for q4, q6 and q8 meshes (top to bottom).

density of states at low doping values, but has an almost negligible influence on the phonon frequencies, as we see in preliminary calculations. How this splitting affects the electron-phonon coupling strength is difficult to predict, but it could lead to a change of λ.

Next, an increase of the coarse phonon mesh from $4 \times 4 \times 4$ to higher values is needed for quantitative convergence of the results, with tests with denser meshes up to $16 \times 16 \times 16$ or more required to see to what values λ converges numerically. This would not necessarily improve the qualitative understanding of the problem as discussed in the main body of the text, but accurate numbers for mode-resolved and total λ could benefit research in all areas connected to electron-phonon interactions.

Finally, the computation of already mentioned KTO slabs with relaxed surfaces would result in new insights into surface effects. Relaxing the slabs while screening for imaginary modes indicating structural instabilities could already be very helpful in understanding if and how polar fluctuations manifest at the different surfaces. Calculation of electron-phonon coupling properties using these slabs, however, is currently unfeasible.

6

Summary and Outlook

Throughout the previous chapters, I have presented my work on ferroelectric and quantum paraelectric materials, their properties, and how they change with doping, using first-principle calculations on the perovskite materials $BaTiO_3$, $SrTiO_3$ and $KTaO_3$.

In chapter 3, we showed that polarization and metallicity can coexist in $BaTiO_3$. We discovered that different dopants have different effects on the polarization, ranging from an unexpected increase to complete suppression. We found that the main contribution to the polarization change comes from geometry changes, followed by the charge carriers (electron-doping) and the impurity atom itself (hole-doping).

In chapter 4, we focused on the quantum paraelectric state. We developed a model that explicitly treats the quantum nature of the ions and is based on quantities that can be extracted from simple DFT and DFPT calculations. We showed that substitution of ^{18}O in $SrTiO_3$ may have a smaller effect on the quantum paraelectric properties than previously expected. We also collected and summarized different ways of describing this quantum paraelectric state in the literature and showed that the quantum tunneling is best described by the eigenvector of the ferroelectric soft phonon mode and its imaginary phonon frequency.

Finally, in chapter 5, we calculated the mode-resolved and total electron-phonon coupling strength λ in the context of the highly surface-termination dependent superconductivity in $KTaO_3$. We showed that there is no direct correlation between the total λ along different reciprocal directions and the experimentally measured T_c of different surfaces, indicating that the superconductivity is not of the simple BCS-type. Instead, the strong localization of λ at the ferroelectric soft mode at low energies hints towards a coupling mechanism involving this phonon mode.

Looking ahead, several interesting topics and directions are worth pursuing, both computationally and experimentally.

On the topic of ferroelectricity in metals, our calculations predicted an increase in polarization with potassium doping, which should be tested experimentally. For the model for quantum paraelectricity, a computational test of our isotope effect predictions using more sophisticated path-integral quantum Monte-Carlo simulations would be valuable in confirming the validity of our model. Furthermore, an extension to two dimensions would be worthwhile, in improving the model by capturing more of the underlying energy surface.

The topic of superconductivity in $KTaO_3$ is probably the most intriguing at the moment, and the absence of correlation between electron-phonon coupling strength λ and superconducting critical temperatures T_c in our bulk calculations points to two extensions. Including spin-orbit coupling in the calculations would be the natural next step to determine how the electronic band splitting caused by the spin-orbit coupling influences the λ values. Using actual surface slabs to calculate λ would bring us much closer to the experimental geometry and would require either greater computer resources or a methodological extension, due to the much larger number of atoms and lower symmetry.

Finally – while I have to admit that we will most probably not see room-temperature superconductivity in any of the three studied materials – a better understanding of the ferroelectric and quantum paraelectric phases and their behavior upon doping, to which I have contributed with this thesis, will hopefully lead to a better understanding of the origin of superconductivity in exotic superconductors and, ultimately, to room-temperature superconductivity in related systems, where superconductivity and quantum effects are intimately linked.

Publications

Scientific Journals

- **Tobias Esswein** and Nicola A. Spaldin. First-principles calculation of electron-phonon coupling in doped $KTaO_3$. *arXiv preprint* 2210.14113 (2022). DOI: 10.48550/arXiv.2210.14113.
- **Tobias Esswein** and Nicola A. Spaldin. Ferroelectric, quantum paraelectric or paraelectric? Calculating the evolution from $BaTiO_3$ to $SrTiO_3$ to $KTaO_3$ using a single-particle quantum-mechanical description of the ions. *Phys. Rev. Research 4*, 033020 (2022). DOI: 10.1103/PhysRevResearch.4.033020.
- Veronica F. Michel, **Tobias Esswein**, and Nicola A. Spaldin. Interplay between Ferroelectricity and Metallicity in $BaTiO_3$ *J. Mater. Chem. C 9*, 8640–8649 (2021). DOI: 10.1039/D1TC01868J.

Conference Contributions & Workshops

- Poster Presentation: *A simple single-particle quantum model for quantum paraelectricity in $SrTiO_3$*. Theoretical Physics Symposium, Hamburg, Germany (2022).
- Poster Presentation: *A simple single-particle quantum model for quantum paraelectricity in $SrTiO_3$*. MaP Graduate Symposium, Zurich, Switzerland (2022).
- Conference Talk: *Ferroelectric, quantum paraelectric or paraelectric? Calculating the evolution from $BaTiO_3$ to $SrTiO_3$ to $KTaO_3$ using a single-particle quantum-mechanical description of the ions*. Psi-k conference, Lausanne, Switzerland (2022).

- Workshop: Virtual School on Electron-Phonon Physics and the EPW code, Online (Pandemic) (2021).
- Conference Talk: *A Simple Model for Quantum Paraelectricity in $SrTiO_3$ and $KTaO_3$ based on standard DFT*. Fundamental Physics of Ferroelectrics and related materials, Online (Pandemic) (2021).
- Invited Talk: *Quantum paraelectricity in $SrTiO_3$ and $KTaO_3$ from density functional theory*. MARVEL Junior Seminar, Online (Pandemic) (2020).
- Workshop: Advanced Electronic Structure Methods in Condensed Matter Physics, Lausanne, Switzerland (2019).
- Poster Presentation: *Quantum Criticality, Superconductivity and Electron-Phonon Coupling in $KTaO_3$ and $SrTiO_3$*. ABINIT Hands-on 2019: ab-initio nanoscience simulations, Paris, France (2019).
- Workshop: ABINIT Hands-on 2019: ab-initio nanoscience simulations, Paris, France (2019).

Bibliography

1. Dimos, D. & Mueller, C. H. Perovskite Thin Films for High-Frequency Capacitor Applications. *Annu. Rev. Mater. Sci.* **28,** 397–419. doi:10.1146/annurev.matsci.28.1.397 (1998).
2. Webber, K. G. *et al.* Review of the Mechanical and Fracture Behavior of Perovskite Lead-Free Ferroelectrics for Actuator Applications. *Smart Mater. Struct.* **26,** 063001. doi:10.1088/1361-665X/aa590c (2017).
3. Huang, Y. *et al.* The Application of Perovskite Materials in Solar Water Splitting. *J. Semicond.* **41,** 011701. doi:10.1088/1674-4926/41/1/011701 (2020).
4. Wang, W. *et al.* Perovskite Oxide Based Electrodes for High-Performance Photoelectrochemical Water Splitting. *Angew. Chem. Int. Ed.* **59,** 136–152. doi:10.1002/anie.201900292 (2020).
5. Correa-Baena, J.-P. *et al.* Promises and Challenges of Perovskite Solar Cells. *Science* **358,** 739–744. doi:10.1126/science.aam6323 (2017).
6. *Perovskite Oxide for Solid Oxide Fuel Cells* (ed Ishihara, T.) ISBN: 978-0-387-77707-8. doi:10.1007/978-0-387-77708-5 (Springer US, Boston, MA, 2009).
7. Megaw, H. D. in *Crystal Structures : A Working Approach* (W.B. Saunders, Philadelphia, 1973). ISBN: 0-7216-6260-9.
8. Glazer, A. M. Simple Ways of Determining Perovskite Structures. *Acta Crystallogr. A* **31,** 756–762. doi:10.1107/S0567739475001635 (1975).
9. Rimai, L. & deMars, G. A. Electron Paramagnetic Resonance of Trivalent Gadolinium Ions in Strontium and Barium Titanates. *Phys. Rev.* **127,** 702–710. doi:10.1103/physrev.127.702 (1962).
10. Hampel, A. & Ederer, C. Interplay between breathing mode distortion and magnetic order in rare-earth nickelates $RNiO_3$ within DFT+U. *Phys. Rev. B* **96,** 165130. doi:10.1103/PhysRevB.96.165130 (2017).
11. Muralt, P. Ferroelectric Thin Films for Micro-Sensors and Actuators: A Review. *J. Micromech. Microeng.* **10,** 136–146. doi:2011050205491300 (2000).
12. Scott, J. F. *Ferroelectric Memories* red. by Itoh, K. & Sakurai, T. ISBN: 978-3-642-08565-9. doi:10.1007/978-3-662-04307-3 (Springer, Berlin, Heidelberg, 2000).
13. Yun, Y. *et al.* Strongly Enhanced and Tunable Photovoltaic Effect in Ferroelectric-Paraelectric Superlattices. *Sci. Adv.* **7,** eabe4206. doi:10.1126/sciadv.abe4206 (2021).
14. Cochran, W. Crystal Stability and the Theory of Ferroelectricity. *Adv. Phys.* **9,** 387–423. doi:10.1080/00018736000101229 (1960).
15. *Physics of Ferroelectrics: A Modern Perspective* (eds Rabe, K. M., Ahn, C. H. & Triscone, J.-M.) *Topics in Applied Physics* **v. 105.** 388 pp. ISBN: 978-3-540-34590-9 (Springer, Berlin, New York, 2007).

16. Sachdev, S. *Quantum Phase Transitions, Second Edition* 2nd ed. 520 pp. ISBN: 978-0-521-51468-2 (Cambridge University Press, 2011).
17. Rowley, S. E. *et al.* Ferroelectric Quantum Criticality. *Nat. Phys.* **10,** 367–372. doi:10.1038/nphys2924 (2014).
18. Müller, K. A. & Burkard, H. SrTiO3: An Intrinsic Quantum Paraelectric below 4 K. *Phys. Rev. B* **19,** 3593–3602. doi:10.1103/PhysRevB.19.3593 (1979).
19. Narayan, A. *et al.* Multiferroic Quantum Criticality. *Nat. Mater.* **18,** 223–228. doi:10.1038/s41563-018-0255-6 (2019).
20. Senthil, T. Critical Fermi Surfaces and Non-Fermi Liquid Metals. *Phys. Rev. B* **78,** 035103. doi:10.1103/PhysRevB.78.035103 (2008).
21. Van Delft, D. & Kes, P. The Discovery of Superconductivity. *Phys. Today* **63,** 38–43. doi:10.1063/1.3490499 (2010).
22. Landau, L. in *Collected Papers of L.D. Landau* (ed Ter haar, D.) 546–568 (Pergamon, 1965). ISBN: 978-0-08-010586-4. doi:10.1016/B978-0-08-010586-4.50078-X.
23. Bardeen, J., Cooper, L. N. & Schrieffer, J. R. Microscopic Theory of Superconductivity. *Phys. Rev.* **106,** 162–164. doi:10.1103/PhysRev.106.162 (1957).
24. Cooper, L. N. Bound Electron Pairs in a Degenerate Fermi Gas. *Phys. Rev.* **104,** 1189–1190. doi:10.1103/PhysRev.104.1189 (1956).
25. Fröhlich, H. Theory of the Superconducting State. I. The Ground State at the Absolute Zero of Temperature. *Phys. Rev.* **79,** 845–856. doi:10.1103/PhysRev.79.845 (1950).
26. Reynolds, C. A. *et al.* Superconductivity of Isotopes of Mercury. *Phys. Rev.* **78,** 487–487. doi:10.1103/PhysRev.78.487 (1950).
27. Maxwell, E. Isotope Effect in the Superconductivity of Mercury. *Phys. Rev.* **78,** 477–477. doi:10.1103/PhysRev.78.477 (1950).
28. Schrieffer, J. R. *Theory of Superconductivity* 352 pp. ISBN: 978-0-7382-0120-7. doi:10.1201/9780429495700 (CRC Press, Boca Raton, 1964).
29. Eliashberg, G. Interactions between Electrons and Lattice Vibrations in a Superconductor. *Sov. Phys. JETP* **11,** 696–702 (1960).
30. Marsiglio, F. Eliashberg Theory: A Short Review. *Ann. Phys. (N. Y.) Eliashberg Theory at 60: Strong-coupling Superconductivity and Beyond* **417,** 168102. doi:10.1016/j.aop.2020.168102 (2020).
31. Schooley, J. F., Hosler, W. R. & Cohen, M. L. Superconductivity in Semiconducting SrTiO3. *Phys. Rev. Lett.* **12,** 474–475. doi:10.1103/PhysRevLett.12.474 (1964).
32. McMillan, W. L. Transition Temperature of Strong-Coupled Superconductors. *Phys. Rev.* **167,** 331–344. doi:10.1103/PhysRev.167.331 (1968).
33. Sleight, A. W., Gillson, J. L. & Bierstedt, P. E. High-temperature superconductivity in the $BaPb_{1-x}Bi_xO_3$ systems. *Solid State Commun.* **17,** 27–28. doi:10.1016/0038-1098(75)90327-0 (1975).
34. Bednorz, J. G. & Müller, K. A. Possible High Tc Superconductivity in the Ba-La-Cu-O System. *Z. Physik B - Condens. Matter* **64,** 189–193. doi:10.1007/BF01303701 (1986).
35. Edge, J. M. *et al.* Quantum Critical Origin of the Superconducting Dome in SrTiO3. *Phys. Rev. Lett.* **115,** 247002. doi:10.1103/PhysRevLett.115.247002 (2015).

36. Waugh, M. D. Design Solutions for DC Bias in Multilayer Ceramic Capacitors, 3 (2010).
37. Acosta, M. *et al.* $BaTiO_3$-based Piezoelectrics: Fundamentals, Current Status, and Perspectives. *Appl. Phys. Rev.* **4,** 041305. doi:10.1063/1.4990046 (2017).
38. Jona, F. & Shirane, G. *Ferroelectric Crystals* (Pergamon, Oxford [etc, 1962).
39. Kwei, G. H. *et al.* Structures of the Ferroelectric Phases of Barium Titanate. *J. Phys. Chem.* **97,** 2368–2377. doi:10.1021/j100112a043 (1993).
40. King-Smith, R. D. & Vanderbilt, D. Theory of Polarization of Crystalline Solids. *Phys. Rev. B* **47,** 1651–1654. doi:10.1103/PhysRevB.47.1651 (1993).
41. Spaldin, N. A. A Beginner's Guide to the Modern Theory of Polarization. *J. Solid State Chem. Polar Inorganic Materials: Design Strategies and Functional Properties* **195,** 2–10. doi:10.1016/j.jssc.2012.05.010 (2012).
42. Yuk, S. F. *et al.* Towards an Accurate Description of Perovskite Ferroelectrics: Exchange and Correlation Effects. *Sci. Rep.* **7,** 43482. doi:10.1038/srep43482 (2017).
43. Wahl, R., Vogtenhuber, D. & Kresse, G. $SrTiO_3$ and $BaTiO_3$ revisited using the projector augmented wave method: Performance of hybrid and semilocal functionals. *Phys. Rev. B* **78,** 104116. doi:10.1103/PhysRevB.78.104116 (2008).
44. Anderson, P. W. & Blount, E. I. Symmetry Considerations on Martensitic Transformations: "Ferroelectric" Metals? *Phys. Rev. Lett.* **14,** 217–219. doi:10.1103/PhysRevLett.14.217 (1965).
45. Shi, Y. *et al.* A Ferroelectric-like Structural Transition in a Metal. *Nat. Mater.* **12,** 1024–1027. doi:10.1038/nmat3754 (2013).
46. Kolodiazhnyi, T. *et al.* Thermoelectric power, Hall effect, and mobility of n-type $BaTiO_3$. *Phys. Rev. B* **68,** 085205. doi:10.1103/PhysRevB.68.085205 (2003).
47. Kolodiazhnyi, T. Insulator-metal transition and anomalous sign reversal of the dominant charge carriers in perovskite $BaTiO_{3-\delta}$. *Phys. Rev. B* **78,** 045107. doi:10.1103/PhysRevB.78.045107 (2008).
48. Kolodiazhnyi, T. *et al.* Persistence of Ferroelectricity in $BaTiO_3$ through the Insulator-Metal Transition. *Phys. Rev. Lett.* **104,** 147602. doi:10.1103/PhysRevLett.104.147602 (2010).
49. Rischau, C. W. *et al.* A ferroelectric quantum phase transition inside the superconducting dome of $Sr_{1-x}Ca_xTiO_{3-\delta}$. *Nat. Phys.* **13,** 643–648. doi:10.1038/nphys4085 (2017).
50. Bréhin, J. *et al.* Switchable two-dimensional electron gas based on ferroelectric Ca:$SrTiO_3$. *Phys. Rev. Materials* **4,** 041002. doi:10.1103/PhysRevMaterials.4.041002 (2020).
51. Takahashi, K. S. *et al.* Polar Metal Phase Stabilized in Strained La-doped BaTiO3 Films. *Sci. Rep.* **7,** 4631. doi:10.1038/s41598-017-04635-3 (2017).
52. Cordero, F. *et al.* Probing ferroelectricity in highly conducting materials through their elastic response: Persistence of ferroelectricity in metallic $BaTiO_{3-\delta}$. *Phys. Rev. B* **99,** 064106. doi:10.1103/PhysRevB.99.064106 (2019).
53. Bhowal, S. & Spaldin, N. A. *Polar Metals: Principles and Prospects* 2022. doi:10.48550/arXiv.2210.02993.

54. Unoki, H. & Sakudo, T. Electron Spin Resonance of Fe3+ in $SrTiO_3$ with Special Reference to the 110°K Phase Transition. *J. Phys. Soc. Jpn.* **23,** 546–552. doi:10.1143/JPSJ.23.546 (1967).
55. Fleury, P. A. & Worlock, J. M. Electric-Field-Induced Raman Scattering in $SrTiO_3$ and $KTaO_3$. *Phys. Rev.* **174,** 613–623. doi:10.1103/PhysRev.174.613 (1968).
56. Pytte, E. & Feder, J. Theory of a Structural Phase Transition in Perovskite-Type Crystals. *Phys. Rev.* **187,** 1077–1088. doi:10.1103/PhysRev.187.1077 (1969).
57. Müller, K. A. The Study of Structural Phase Transitions Using Paramagnetic Resonance. Static Investigations. *Struct. Phase Transit. Soft Modes,* 73–84 (1971).
58. Scott, J. F. Soft-Mode Spectroscopy: Experimental Studies of Structural Phase Transitions. *Rev. Mod. Phys.* **46,** 83–128. doi:10.1103/RevModPhys.46.83 (1974).
59. Klose, W. & Schuster, H. On Superconductivity in $SrTiO_3$. *Solid State Commun.* **6,** 89–91. doi:10.1016/0038-1098(68)90007-0 (1968).
60. Appel, J. Soft-Mode Superconductivity in SrTiO3-x. *Phys. Rev.* **180,** 508–516. doi:10.1103/PhysRev.180.508 (1969).
61. Weaver, H. E. Dielectric Properties of Single Crystals of $SrTiO_3$ at Low Temperatures. *J. Phys. Chem. Solids* **11,** 274–277. doi:10.1016/0022-3697(59)90226-4 (1959).
62. Cowley, R. A. Lattice Dynamics and Phase Transitions of Strontium Titanate. *Phys. Rev.* **134,** A981–A997. doi:10.1103/PhysRev.134.A981 (1964).
63. Yamada, Y. & Shirane, G. Neutron Scattering and Nature of the Soft Optical Phonon in $SrTiO_3$. *J. Phys. Soc. Jpn.* **26,** 396–403. doi:10.1143/JPSJ.26.396 (1969).
64. Samara, G. A. Pressure and Temperature Dependences of the Dielectric Properties of the Perovskites $BaTiO_3$ and $SrTiO_3$. *Phys. Rev.* **151,** 378–386. doi:10.1103/PhysRev.151.378 (1966).
65. Sakudo, T. & Unoki, H. Dielectric Properties of $SrTiO_3$ at Low Temperatures. *Phys. Rev. Lett.* **26,** 851–853. doi:10.1103/PhysRevLett.26.851 (1971).
66. Burke, W. J. & Pressley, R. J. Stress Induced Ferroelectricity in $SrTiO_3$. *Solid State Commun.* **9,** 191–195. doi:10.1016/0038-1098(71)90115-3 (1971).
67. Gastiasoro, M. N., Ruhman, J. & Fernandes, R. M. Superconductivity in Dilute SrTiO3: A Review. *Ann. Phys. (N. Y.)* **417,** 168107. doi:10.1016/j.aop.2020.168107 (2020).
68. Migdal, A. B. Interaction between Electrons and Lattice Vibrations in a Normal Metal. *JETP* **7,** 996. http://www.jetp.ac.ru/cgi-bin/e/index/e/7/6/p996?a=list (1958).
69. Stucky, A. *et al.* Isotope Effect in Superconducting n-doped $SrTiO_3$. *Sci. Rep.* **6,** 37582. doi:10.1038/srep37582 (2016).
70. Ueno, K. *et al.* Discovery of Superconductivity in $KTaO_3$ by Electrostatic Carrier Doping. *Nat. Nano.* **6,** 408–412. doi:10.1038/nnano.2011.78 (2011).
71. Ueno, K. *et al.* Field-Induced Superconductivity in Electric Double Layer Transistors. *J. Phys. Soc. Jpn.* **83,** 032001. doi:10.7566/JPSJ.83.032001 (2014).
72. Chen, Z. *et al.* Two-Dimensional Superconductivity at the $LaAlO_3/KTaO_3(110)$ Heterointerface. *Phys. Rev. Lett.* **126,** 026802. doi:10.1103/PhysRevLett.126.026802 (2021).

73. Liu, C. *et al.* Two-Dimensional Superconductivity and Anisotropic Transport at KTaO3 (111) Interfaces. *Science* **371,** 716–721. doi:10.1126/science.aba5511 (2021).
74. Ren, T. *et al.* Two-Dimensional Superconductivity at the Surfaces of $KTaO_3$ Gated with Ionic Liquid. *Sci. Adv.* **8,** eabn4273. doi:10.1126/sciadv.abn4273 (2022).
75. Hulm, J. K., Matthias, B. T. & Long, E. A. A Ferromagnetic Curie Point in $KTaO_3$ at Very Low Temperatures. *Phys. Rev.* **79,** 885–886. doi:10.1103/PhysRev.79.885 (1950).
76. Barrett, J. H. Dielectric Constant in Perovskite Type Crystals. *Phys. Rev.* **86,** 118–120. doi:10.1103/PhysRev.86.118 (1952).
77. Samara, G. A. & Morosin, B. Anharmonic Effects in $KTaO_3$: Ferroelectric Mode, Thermal Expansion,and Compressibility. *Phys. Rev. B* **8,** 1256–1264. doi:10.1103/PhysRevB.8.1256 (1973).
78. Nakamura, H. & Kimura, T. Electric Field Tuning of Spin-orbit Coupling in $KTaO_3$ Field-effect Transistors. *Phys. Rev. B* **80,** 121308. doi:10.1103/PhysRevB.80.121308 (2009).
79. Tao, L. L. & Wang, J. Strain-Tunable Ferroelectricity and Its Control of Rashba Effect in KTaO3. *J. Appl. Phys.* **120,** 234101. doi:10.1063/1.4972198 (2016).
80. King, P. D. C. *et al.* Subband Structure of a Two-Dimensional Electron Gas Formed at the Polar Surface of the Strong Spin-Orbit Perovskite $KTaO_3$. *Phys. Rev. Lett.* **108,** 117602. doi:10.1103/PhysRevLett.108.117602 (2012).
81. Gupta, A. *et al.* KTaO3—The New Kid on the Spintronics Block. *Adv. Mater.* **34,** 2106481. doi:10.1002/adma.202106481 (2022).
82. Sakai, A. *et al.* Thermoelectric Properties of Electron-Doped KTaO3. *Jpn. J. Appl. Phys.* **48,** 097002. doi:10.1143/JJAP.48.097002 (2009).
83. Sarfraz, S. *et al.* Physical Properties of $KTaO_3$ Compound for Optoelectronic and Thermoelectric Applications: A DFT Study. *Mater. Sci. Semicond. Process.* **148,** 106811. doi:10.1016/j.mssp.2022.106811 (2022).
84. Liu, C. *et al. Tunable superconductivity at the oxide-insulator/$KTaO_3$ interface and its origin* 2022. doi:10.48550/arXiv.2203.05867.
85. Yu, Y. *et al.* Theory of Superconductivity in Doped Quantum Paraelectrics. *npj Quantum Mater.* **7,** 63. doi:10.1038/s41535-022-00466-2 (2022).
86. Michel, V. F., Esswein, T. & Spaldin, N. A. Interplay between Ferroelectricity and Metallicity in BaTiO3. *J. Mater. Chem. C* **9,** 8640–8649. doi:10.1039/D1TC01868J (2021).
87. Esswein, T. & Spaldin, N. A. Ferroelectric, quantum paraelectric, or paraelectric? Calculating the evolution from $BaTiO_3$ to $SrTiO_3$ to $KTaO_3$ using a single-particle quantum mechanical description of the ions. *Phys. Rev. Research* **4,** 033020. doi:10.1103/PhysRevResearch.4.033020 (2022).
88. Esswein, T. & Spaldin, N. A. *First-principles calculation of electron-phonon coupling in doped $KTaO_3$* 2022. doi:10.48550/arXiv.2210.14113.
89. Born, M. & Oppenheimer, R. Zur Quantentheorie Der Molekeln. *Ann. Phys.* **389,** 457–484. doi:10.1002/andp.19273892002 (1927).
90. Hohenberg, P. & Kohn, W. Inhomogeneous Electron Gas. *Phys. Rev.* **136,** B864–B871. doi:10.1103/PhysRev.136.B864 (1964).

91. Kohn, W. & Sham, L. J. Self-Consistent Equations Including Exchange and Correlation Effects. *Phys. Rev.* **140,** A1133–A1138. doi:10.1103/PhysRev.140.A1133 (1965).
92. Ceperley, D. M. & Alder, B. J. Ground State of the Electron Gas by a Stochastic Method. *Phys. Rev. Lett.* **45,** 566–569. doi:10.1103/PhysRevLett.45.566 (1980).
93. Perdew, J. P. & Wang, Y. Accurate and Simple Analytic Representation of the Electron-Gas Correlation Energy. *Phys. Rev. B* **45,** 13244–13249. doi:10.1103/PhysRevB.45.13244 (1992).
94. Perdew, J. P., Burke, K. & Ernzerhof, M. Generalized Gradient Approximation Made Simple. *Phys. Rev. Lett.* **77,** 3865–3868. doi:10.1103/PhysRevLett.77.3865 (1996).
95. Perdew, J. P. *et al.* Restoring the Density-Gradient Expansion for Exchange in Solids and Surfaces. *Phys. Rev. Lett.* **100,** 136406. doi:10.1103/PhysRevLett.100.136406 (2008).
96. *SSSP Efficiency* doi:10.24435/materialscloud:rz-77.
97. Garrity, K. F. *et al.* Pseudopotentials for High-Throughput DFT Calculations. *Comput. Mater. Sci.* **81,** 446–452. doi:10.1016/j.commatsci.2013.08.053 (2014).
98. Garrity, K. F. *et al. GBRV Pseudopotentials* GBRV high-throughput pseudopotentials. https://www.physics.rutgers.edu/gbrv/ (2021).
99. Urru, A. *Lattice Dynamics with Fully Relativistic Pseudopotentials for Magnetic Systems, with Selected Applications* PhD thesis (2020). http://hdl.handle.net/20.500.11767/115671.
100. Baroni, S. *et al.* Phonons and Related Crystal Properties from Density-Functional Perturbation Theory. *Rev. Mod. Phys.* **73,** 515–562. doi:10.1103/revmodphys.73.515 (2001).
101. Hellmann, H. *Einführung in die Quantenchemie* (Deuticke, Leipzig, 1937).
102. Feynman, R. P. Forces in Molecules. *Phys. Rev.* **56,** 340–343. doi:10.1103/PhysRev.56.340 (1939).
103. Giannozzi, P. *et al.* Ab Initio Calculation of Phonon Dispersions in Semiconductors. *Phys. Rev. B* **43,** 7231–7242. doi:10.1103/PhysRevB.43.7231 (1991).
104. Togo, A. & Tanaka, I. First Principles Phonon Calculations in Materials Science. *Scr. Mater.* **108,** 1–5. doi:10.1016/j.scriptamat.2015.07.021 (2015).
105. Poncé, S. *et al.* EPW: Electron–Phonon Coupling, Transport and Superconducting Properties Using Maximally Localized Wannier Functions. *Comput. Phys. Commun.* **209,** 116–133. doi:10.1016/j.cpc.2016.07.028 (2016).
106. Wannier, G. H. The Structure of Electronic Excitation Levels in Insulating Crystals. *Phys. Rev.* **52,** 191–197. doi:10.1103/PhysRev.52.191 (1937).
107. Marzari, N. & Vanderbilt, D. Maximally Localized Generalized Wannier Functions for Composite Energy Bands. *Phys. Rev. B* **56,** 12847–12865. doi:10.1103/PhysRevB.56.12847 (1997).
108. Marzari, N. *et al.* Maximally Localized Wannier Functions: Theory and Applications. *Rev. Mod. Phys.* **84,** 1419–1475. doi:10.1103/RevModPhys.84.1419 (2012).
109. Giustino, F., Cohen, M. L. & Louie, S. G. Electron-Phonon Interaction Using Wannier Functions. *Phys. Rev. B* **76,** 165108. doi:10.1103/PhysRevB.76.165108 (2007).

110. Noffsinger, J. *et al.* EPW: A Program for Calculating the Electron–Phonon Coupling Using Maximally Localized Wannier Functions. *Comput. Phys. Commun.* **181,** 2140–2148. doi:10.1016/j.cpc.2010.08.027 (2010).
111. *List of Quantum Chemistry and Solid-State Physics Software* Wikipedia. https://en.wikipedia.org/w/index.php?title=List_of_quantum_chemistry_and_solid-state_physics_software&oldid=1099932843 (2022).
112. Kresse, G. & Hafner, J. Norm-Conserving and Ultrasoft Pseudopotentials for First-Row and Transition Elements. *J. Phys.: Condens. Matter* **6,** 8245. doi:10.1088/0953-8984/6/40/015 (1994).
113. Kresse, G. & Furthmüller, J. Efficiency of Ab-Initio Total Energy Calculations for Metals and Semiconductors Using a Plane-Wave Basis Set. *Comput. Mater. Sci.* **6,** 15–50. doi:10.1016/0927-0256(96)00008-0 (1996).
114. Kresse, G. & Furthmüller, J. Efficient Iterative Schemes for Ab Initio Total-Energy Calculations Using a Plane-Wave Basis Set. *Phys. Rev. B* **54,** 11169–11186. doi:10.1103/PhysRevB.54.11169 (1996).
115. Giannozzi, P. *et al.* QUANTUM ESPRESSO: A Modular and Open-Source Software Project for Quantum Simulations of Materials. *J. Phys. Condens. Matter* **21,** 395502. doi:10.1088/0953-8984/21/39/395502 (2009).
116. Giannozzi, P. *et al.* Advanced Capabilities for Materials Modelling with Quantum ESPRESSO. *J. Phys. Condens. Matter* **29,** 465901. doi:10.1088/1361-648X/aa8f79 (2017).
117. Giannozzi, P. *et al.* Quantum ESPRESSO toward the Exascale. *J. Chem. Phys.* **152,** 154105. doi:10.1063/5.0005082 (2020).
118. *The VASP Manual - Vaspwiki* https://www.vasp.at/wiki/index.php/The_VASP_Manual (2020).
119. Maintz, S. *et al.* LOBSTER: A Tool to Extract Chemical Bonding from Plane-Wave Based DFT. *J. Comput. Chem.* **37,** 1030–1035. doi:10.1002/jcc.24300 (2016).
120. Nelson, R. *et al.* LOBSTER: Local Orbital Projections, Atomic Charges, and Chemical-Bonding Analysis from Projector-Augmented-Wave-Based Density-Functional Theory. *J. Comput. Chem.* **41,** 1931–1940. doi:10.1002/jcc.26353 (2020).
121. Dronskowski, R. & Bloechl, P. E. Crystal Orbital Hamilton Populations (COHP): Energy-Resolved Visualization of Chemical Bonding in Solids Based on Density-Functional Calculations. *J. Phys. Chem.* **97,** 8617–8624. doi:10.1021/j100135a014 (1993).
122. Gonze, X. *et al.* First-Principles Computation of Material Properties: The ABINIT Software Project. *Comput. Mater. Sci.* **25,** 478–492. doi:10.1016/S0927-0256(02)00325-7 (2002).
123. Gonze, X. *et al.* The Abinitproject: Impact, Environment and Recent Developments. *Comput. Phys. Commun.* **248,** 107042. doi:10.1016/j.cpc.2019.107042 (2020).
124. *QEF - Quantum ESPRESSO Foundation / q-e · GitLab* GitLab. https://gitlab.com/QEF/q-e (2022).
125. *Documentation* Quantum Espresso. https://www.quantum-espresso.org/documentation/ (2022).

126. *Pseudopotentials* Quantum Espresso. https://www.quantum-espresso.org/pseudopotentials/ (2022).
127. Van Rossum, G. & Drake Jr, F. L. *Python Reference Manual* (Centrum voor Wiskunde en Informatica Amsterdam, 1995).
128. *JupyterLab* JupyterLab, 2022. https://github.com/jupyterlab/jupyterlab (2022).
129. Harris, C. R. *et al.* Array Programming with NumPy. *Nature* **585,** 357–362. doi:10.1038/s41586-020-2649-2 (2020).
130. Virtanen, P. *et al.* SciPy 1.0: Fundamental Algorithms for Scientific Computing in Python. *Nat. Methods* **17,** 261–272. doi:10.1038/s41592-019-0686-2 (2020).
131. Wes McKinney. *Data Structures for Statistical Computing in Python* in *Proc. 9th Python Sci. Conf.* (eds van der Walt, S. & Jarrod Millman) (2010), 56–61. doi:10.25080/Majora-92bf1922-00a.
132. The pandas development team. *Pandas-Dev/Pandas: Pandas* version latest. Zenodo, 2020. doi:10.5281/zenodo.3509134.
133. Hunter, J. D. Matplotlib: A 2D Graphics Environment. *Comput. Sci. Eng.* **9,** 90–95. doi:10.1109/MCSE.2007.55 (2007).
134. Holstein, T. Studies of Polaron Motion: Part I. The Molecular-Crystal Model. *Ann. Phys. (N. Y.)* **8,** 325–342. doi:10.1016/0003-4916(59)90002-8 (1959).
135. Holstein, T. Studies of Polaron Motion: Part II. The "Small" Polaron. *Ann. Phys. (N. Y.)* **8,** 343–389. doi:10.1016/0003-4916(59)90003-X (1959).
136. Iguchi, E. *et al.* Polaronic conduction in n-type $BaTiO_3$ doped with La_2O_3 or Gd_2O_3. *Phys. Rev. B* **43,** 8646–8649. doi:10.1103/PhysRevB.43.8646 (1991).
137. Gillot, C. *et al.* DC Electrical Resistivity of Nb-Doped $BaTiO_3$ and EPR Measurements. *Solid State Commun.* **84,** 1033–1038. doi:10.1016/0038-1098(92)90434-B (1992).
138. Page, K. *et al.* Local Structural Origins of the Distinct Electronic Properties of Nb-Substituted $SrTiO_3$ and $BaTiO_3$. *Phys. Rev. Lett.* **101,** 205502. doi:10.1103/PhysRevLett.101.205502 (2008).
139. Landau, L. Über Die Bewegung Der Elektronen Im Kristallgitter. *Phys. Z. Sowjetunion* **3,** 664–665 (1933).
140. Pekar, S. Local Quantum States of Electrons in an Ideal Ion Crystal. *Zhurnal Eksp. Teor. Fiz.* **16,** 341–348 (1946).
141. Dykman, M. I. & Rashba, E. I. The Roots of Polaron Theory. *Phys. Today* **68,** 10–11. doi:10.1063/PT.3.2735 (2015).
142. Devreese, J. T. More on Polaron Theory History. *Phys. Today* **68,** 11–11. doi:10.1063/PT.3.2897 (2015).
143. Landau, L. D. & Pekar, S. I. Effective Mass of a Polaron. *Ukr. J. Phys.* **53,** 71–74. http://archive.ujp.bitp.kiev.ua/files/journals/53/si/53SI15p.pdf (2008).
144. René de Cotret, L. P. *et al.* Direct Visualization of Polaron Formation in the Thermoelectric SnSe. *PNAS* **119,** e2113967119. doi:10.1073/pnas.2113967119 (2022).
145. Hill, N. A. Why Are There so Few Magnetic Ferroelectrics? *J. Phys. Chem. B* **104,** 6694–6709. doi:10.1021/jp000114x (2000).

146. Wang, Y. *et al.* Ferroelectric Instability Under Screened Coulomb Interactions. *Phys. Rev. Lett.* **109,** 247601. doi:10.1103/PhysRevLett.109.247601 (2012).
147. Bruneval, F. *et al.* Pressure, Relaxation Volume, and Elastic Interactions in Charged Simulation Cells. *Phys. Rev. B* **91,** 024107. doi:10.1103/PhysRevB.91.024107 (2015).
148. Iwazaki, Y. *et al.* Doping-induced phase transitions in ferroelectric $BaTiO_3$ from first-principles calculations. *Phys. Rev. B* **86,** 214103. doi:10.1103/PhysRevB.86.214103 (2012).
149. Deringer, V. L., Tchougréeff, A. L. & Dronskowski, R. Crystal Orbital Hamilton Population (COHP) Analysis As Projected from Plane-Wave Basis Sets. *J. Phys. Chem. A* **115,** 5461–5466. doi:10.1021/jp202489s (2011).
150. Maintz, S. *et al.* Analytic Projection from Plane-Wave and PAW Wavefunctions and Application to Chemical-Bonding Analysis in Solids. *J. Comput. Chem.* **34,** 2557–2567. doi:10.1002/jcc.23424 (2013).
151. Sanchez-Portal, D., Artacho, E. & Soler, J. M. Projection of Plane-Wave Calculations into Atomic Orbitals. *Solid State Commun.* **95,** 685–690. doi:10.1016/0038-1098(95)00341-X (1995).
152. Maintz, S., Esser, M. & Dronskowski, R. Efficient Rotation of Local Basis Functions Using Real Spherical Harmonics. *Acta Phys. Pol. B* **47,** 1165. doi:10.5506/APhysPolB.47.1165 (2016).
153. Lines, M. E. & Glass, A. M. *Principles and Applications of Ferroelectrics and Related Materials* ISBN: 978-0-19-170994-4. https://doi.org/10.1093/acprof:oso/9780198507789.001.0001 (2022) (Oxford University Press, 2001).
154. Benedek, N. A. & Birol, T. 'Ferroelectric' Metals Reexamined: Fundamental Mechanisms and Design Considerations for New Materials. *J. Mater. Chem. C* **4,** 4000–4015. doi:10.1039/C5TC03856A (2016).
155. Kim, T. H. *et al.* Polar Metals by Geometric Design. *Nature* **533,** 68–72. doi:10.1038/nature17628 (2016).
156. Puggioni, D. *et al.* Design of a Mott Multiferroic from a Nonmagnetic Polar Metal. *Phys. Rev. Lett.* **115,** 087202. doi:10.1103/PhysRevLett.115.087202 (2015).
157. Smidman, M. *et al.* Superconductivity and Spin–Orbit Coupling in Non-Centrosymmetric Materials: A Review. *Rep. Prog. Phys.* **80,** 036501. doi:10.1088/1361-6633/80/3/036501 (2017).
158. Jeong, I.-K. *et al.* Structural evolution across the insulator-metal transition in oxygen-deficient $BaTiO_{3-\delta}$ studied using neutron total scattering and Rietveld analysis. *Phys. Rev. B* **84,** 064125. doi:10.1103/PhysRevB.84.064125 (2011).
159. Hickox-Young, D., Puggioni, D. & Rondinelli, J. M. Persistent Polar Distortions from Covalent Interactions in Doped BaTiO 3. *Phys. Rev. B* **102,** 014108. doi:10.1103/PhysRevB.102.014108 (2020).
160. Gu, F., Murray, É. & Tangney, P. Carrier-Mediated Control over the Soft Mode and Ferroelectricity in $BaTiO_3$. *Phys. Rev. Materials,* 17. doi:10.1103/PhysRevMaterials.5.034414 (2021).
161. Zhao, H. J. *et al.* Meta-Screening and Permanence of Polar Distortion in Metallized Ferroelectrics. *Phys. Rev. B* **97,** 054107. doi:10.1103/PhysRevB.97.054107 (2018).

162. Kresse, G. & Joubert, D. From Ultrasoft Pseudopotentials to the Projector Augmented-Wave Method. *Phys. Rev. B* **59,** 1758–1775. doi:10.1103/PhysRevB.59.1758 (1999).
163. Buttner, R. H. & Maslen, E. N. Structural Parameters and Electron Difference Density in BaTiO3. *Acta Crystallogr. B* **48,** 764–769. doi:10.1107/S010876819200510X (1992).
164. Ghosez, P. *et al.* Born Effective Charges of Barium Titanate: Band-by-band Decomposition and Sensitivity to Structural Features. *Phys. Rev. B* **51,** 6765–6768. doi:10.1103/PhysRevB.51.6765 (1995).
165. Resta, R. Macroscopic Electric Polarization as a Geometric Quantum Phase. *EPL* **22,** 133–138. doi:10.1209/0295-5075/22/2/010 (1993).
166. Rondinelli, J. M., Eidelson, A. S. & Spaldin, N. A. Non-d^0 Mn-driven ferroelectricity in antiferromagnetic $BaMnO_3$. *Phys. Rev. B* **79,** 205119. doi:10.1103/PhysRevB.79.205119 (2009).
167. Shannon, R. D. Revised Effective Ionic Radii and Systematic Studies of Interatomic Distances in Halides and Chalcogenides. *Acta Crystallogr. A* **32,** 751–767. doi:10.1107/S0567739476001551 (1976).
168. *Shannon Radii* http://abulafia.mt.ic.ac.uk/shannon/ptable.php (2020).
169. Morrison, F. D. *et al.* Charge Compensation Mechanisms in La-Doped BaTiO3. *J. Electroceramics* **6,** 219–232. doi:10.1023/A:1011400630449 (2001).
170. Janotti, A. *et al.* Dual Behavior of Excess Electrons in Rutile TiO2. *Phys. Status Solidi Rapid Res. Lett.* **7,** 199–203. doi:10.1002/pssr.201206464 (2013).
171. Chandra, H. K. *et al.* Ferroelectric distortions in doped ferroelectrics: $BaTiO_3$:M (M = V—Fe). *Phys. Rev. B* **87,** 214110. doi:10.1103/PhysRevB.87.214110 (2013).
172. Cai, W. *et al.* Vanadium Doping Effects on Microstructure and Dielectric Properties of Barium Titanate Ceramics. *Ceram. Int.* **37,** 3643–3650. doi:10.1016/j.ceramint.2011.06.024 (2011).
173. Collignon, C. *et al.* Metallicity and Superconductivity in Doped Strontium Titanate. *Annu. Rev. Condens. Matter Phys.* **10,** 25–44. doi:10.1146/annurev-conmatphys-031218-013144 (2019).
174. Ricca, C. *et al.* Self-consistent DFT + U + V study of oxygen vacancies in $SrTiO_3$. *Phys. Rev. Research* **2,** 023313. doi:10.1103/PhysRevResearch.2.023313 (2020).
175. Zhong, W. & Vanderbilt, D. Effect of quantum fluctuations on structural phase transitions in $SrTiO_3$ and $BaTiO_3$. *Phys. Rev. B* **53,** 5047–5050. doi:10.1103/PhysRevB.53.5047 (1996).
176. Akbarzadeh, A. R. *et al.* Atomistic Simulations of the Incipient Ferroelectric KTaO3. *Phys. Rev. B* **70,** 054103. doi:10.1103/PhysRevB.70.054103 (2004).
177. Badoux, S. *et al.* Change of Carrier Density at the Pseudogap Critical Point of a Cuprate Superconductor. *Nature* **531,** 210–214. doi:10.1038/nature16983 (2016).
178. Wolchover, N. *The Quantum Secret to Superconductivity* Quanta Magazine. https://www.quantamagazine.org/mega-magnet-reveals-superconductor-secret-20160222/ (2022).
179. Bardeen, J., Cooper, L. N. & Schrieffer, J. R. Theory of Superconductivity. *Phys. Rev.* **108,** 1175–1204. doi:10.1103/PhysRev.108.1175 (1957).

180. Ruhman, J. & Lee, P. A. Superconductivity at Very Low Density: The Case of Strontium Titanate. *Phys. Rev. B* **94,** 224515. doi:10.1103/PhysRevB.94.224515 (2016).
181. Coak, M. J. *et al.* Pressure Dependence of Ferroelectric Quantum Critical Fluctuations. *Phys. Rev. B* **100,** 214111. doi:10.1103/PhysRevB.100.214111 (2019).
182. Van der Marel, D., Barantani, F. & Rischau, C. W. Possible mechanism for superconductivity in doped $SrTiO_3$. *Phys. Rev. Research* **1,** 013003. doi:10.1103/PhysRevResearch.1.013003 (2019).
183. Razavy, M. *Quantum Theory of Tunneling* 2nd ed. ISBN: 978-981-4525-00-8. doi:10.1142/8901 (WORLD SCIENTIFIC, 2014).
184. Cowley, R. A. Temperature Dependence of a Transverse Optic Mode in Strontium Titanate. *Phys. Rev. Lett.* **9,** 159–161. doi:10.1103/PhysRevLett.9.159 (1962).
185. Fujishita, H. *et al.* Quantum Paraelectric States in SrTiO3 and KTaO3: Barrett Model, Vendik Model, and Quantum Criticality. *J. Phys. Soc. Jpn.* **85,** 074703. doi:10.7566/JPSJ.85.074703 (2016).
186. Uwe, H. & Sakudo, T. Stress-induced ferroelectricity and soft phonon modes in $SrTiO_3$. *Phys. Rev. B* **13,** 271–286. doi:10.1103/PhysRevB.13.271 (1976).
187. Fujii, Y., Uwe, H. & Sakudo, T. Stress-Induced Quantum Ferroelectricity in SrTiO3. *J. Phys. Soc. Jpn.* **56,** 1940–1942. doi:10.1143/JPSJ.56.1940 (1987).
188. Bednorz, J. G. & Müller, K. A. Sr(1-x)Ca(x)TiO3: An XY Quantum Ferroelectric with Transition to Randomness. *Phys. Rev. Lett.* **52,** 2289–2292. doi:10.1103/PhysRevLett.52.2289 (1984).
189. Hochli, U. T., Weibel, H. E. & Boatner, L. A. Quantum Limit of Ferroelectric Phase Transitions in $KTa_{1-x}Nb_xO_3$. *Phys. Rev. Lett.* **39,** 1158–1161. doi:10.1103/PhysRevLett.39.1158 (1977).
190. Rytz, D., Höchli, U. T. & Bilz, H. Dielectric Susceptibility in Quantum Ferroelectrics. *Phys. Rev. B* **22,** 359–364. doi:10.1103/PhysRevB.22.359 (1980).
191. Itoh, M. *et al.* Ferroelectricity Induced by Oxygen Isotope Exchange in Strontium Titanate Perovskite. *Phys. Rev. Lett.* **82,** 3540–3543. doi:10.1103/PhysRevLett.82.3540 (1999).
192. Itoh, M. & Wang, R. Quantum Ferroelectricity in SrTiO3 Induced by Oxygen Isotope Exchange. *Appl. Phys. Lett.* **76,** 221–223. doi:10.1063/1.125708 (2000).
193. Haeni, J. H. *et al.* Room-Temperature Ferroelectricity in Strained SrTiO3. *Nature* **430,** 758–761. doi:10.1038/nature02773 (2004).
194. Tyunina, M. *et al.* Evidence for Strain-Induced Ferroelectric Order in Epitaxial Thin-Film $KTaO_3$. *Phys. Rev. Lett.* **104,** 227601. doi:10.1103/PhysRevLett.104.227601 (2010).
195. Kiat, J. M. & Roisnel, T. Rietveld Analysis of Strontium Titanate in the Müller State. *J. Phys. Condens. Matter* **8,** 3471–3475. doi:10.1088/0953-8984/8/19/021 (1996).
196. Zalar, B. *et al.* NMR study of disorder in $BaTiO_3$ and $SrTiO_3$. *Phys. Rev. B* **71,** 064107. doi:10.1103/PhysRevB.71.064107 (2005).
197. Jauch, W. & Palmer, A. Anomalous zero-point motion in $SrTiO_3$: Results from γ-ray diffraction. *Phys. Rev. B* **60,** 2961–2963. doi:10.1103/PhysRevB.60.2961 (1999).

198. Salmani-Rezaie, S., Ahadi, K. & Stemmer, S. Polar Nanodomains in a Ferroelectric Superconductor. *Nano Lett.* **20,** 6542–6547. doi:10.1021/acs.nanolett.0c02285 (2020).
199. Slater, J. C. The Lorentz Correction in Barium Titanate. *Phys. Rev.* **78,** 748–761. doi:10.1103/PhysRev.78.748 (1950).
200. Khmel'nitskii, D. E. & Shneerson, V. L. Low-Temperature Displacement-Type Phase Transition in Crystals. *Sov. Phys. Solid State* **13,** 687 (1971).
201. Bendik, O. Model of the Ferroelectric Mode. *Sov. Phys. Solid State* **14,** 849–856 (1972).
202. Tosatti, E. & Martoňák, R. Rotational Melting in Displacive Quantum Paraelectrics. *Solid State Commun.* **92,** 167–180. doi:10.1016/0038-1098(94)90870-2 (1994).
203. Kvyatkovskii, O. E. Theory of Isotope Effect in Displacive Ferroelectrics. *Solid State Commun.* **117,** 455–459. doi:10.1016/S0038-1098(00)00496-8 (2001).
204. Shin, D. *et al.* Quantum paraelectric phase of $SrTiO_3$ from first principles. *Phys. Rev. B* **104,** L060103. doi:10.1103/PhysRevB.104.L060103 (2021).
205. Migoni, R., Bilz, H. & Bäuerle, D. Origin of Raman Scattering and Ferroelectricity in Oxidic Perovskites. *Phys. Rev. Lett.* **37,** 1155–1158. doi:10.1103/PhysRevLett.37.1155 (1976).
206. Bilz, H., Benedek, G. & Bussmann-Holder, A. Theory of Ferroelectricity: The Polarizability Model. *Phys. Rev. B* **35,** 4840–4849. doi:10.1103/PhysRevB.35.4840 (1987).
207. King-Smith, R. D. & Vanderbilt, D. First-Principles Investigation of Ferroelectricity in Perovskite Compounds. *Phys. Rev. B* **49,** 5828–5844. doi:10.1103/PhysRevB.49.5828 (1994).
208. Zhong, W., King-Smith, R. D. & Vanderbilt, D. Giant LO-TO Splittings in Perovskite Ferroelectrics. *Phys. Rev. Lett.* **72,** 3618–3621. doi:10.1103/PhysRevLett.72.3618 (1994).
209. Zhong, W. & Vanderbilt, D. Competing Structural Instabilities in Cubic Perovskites. *Phys. Rev. Lett.* **74,** 2587–2590. doi:10.1103/PhysRevLett.74.2587 (1995).
210. Sai, N. & Vanderbilt, D. First-principles study of ferroelectric and antiferrodistortive instabilities in tetragonal $SrTiO_3$. *Phys. Rev. B* **62,** 13942–13950. doi:10.1103/PhysRevB.62.13942 (2000).
211. Aschauer, U. & Spaldin, N. A. Competition and Cooperation between Antiferrodistortive and Ferroelectric Instabilities in the Model Perovskite SrTiO3. *J. Phys. Condens. Matter* **26,** 122203. doi:10.1088/0953-8984/26/12/122203 (2014).
212. Luo, W. *et al.* Structural and electronic properties of n-doped and p-doped $SrTiO_3$. *Phys. Rev. B* **70,** 214109. doi:10.1103/PhysRevB.70.214109 (2004).
213. Íñiguez, J. & Vanderbilt, D. First-Principles Study of the Temperature-Pressure Phase Diagram of $BaTiO_3$. *Phys. Rev. Lett.* **89,** 115503. doi:10.1103/PhysRevLett.89.115503 (2002).
214. Coak, M. J. *et al.* Dielectric Response of Quantum Critical Ferroelectric as a Function of Pressure. *Sci. Rep.* **8,** 14936. doi:10.1038/s41598-018-33320-2 (2018).
215. Coak, M. J. *et al.* Quantum Critical Phenomena in a Compressible Displacive Ferroelectric. *PNAS* **117,** 12707–12712. doi:10.1073/pnas.1922151117 (2020).

216. Rowley, S. *et al.* Ferromagnetic and Ferroelectric Quantum Phase Transitions. *Phys. Status Solidi B* **247,** 469–475. doi:10.1002/pssb.200983081 (2010).
217. Bussmann-Holder, A. & Bishop, A. R. Incomplete ferroelectricity in $SrTi^{18}O_3$. *Eur. Phys. J. B* **53,** 279–282. doi:10.1140/epjb/e2006-00373-8 (2006).
218. Bussmann-Holder, A., Büttner, H. & Bishop, A. R. Polar-Soft-Mode-Driven Structural Phase Transition in $SrTiO_3$. *Phys. Rev. Lett.* **99,** 167603. doi:10.1103/PhysRevLett.99.167603 (2007).
219. Bussmann-Holder, A. & Bishop, A. R. Dimensional crossover and absence of quantum criticality in $SrTi^{16}O_{1-x}{}^{18}O_x$. *Phys. Rev. B* **78,** 104117. doi:10.1103/PhysRevB.78.104117 (2008).
220. *Finite Difference Coefficient* Wikipedia. https://en.wikipedia.org/w/index.php?title=Finite_difference_coefficient&oldid=1078320339 (2022).
221. Vogt, H. Refined treatment of the model of linearly coupled anharmonic oscillators and its application to the temperature dependence of the zone-center soft-mode frequencies of $KTaO_3$ and $SrTiO_3$. *Phys. Rev. B* **51,** 8046–8059. doi:10.1103/PhysRevB.51.8046 (1995).
222. Yamanaka, A. *et al.* Evidence for Competing Orderings in Strontium Titanate from Hyper-Raman Scattering Spectroscopy. *EPL* **50,** 688. doi:10.1209/epl/i2000-00325-6 (2000).
223. Herrera, C. *et al.* Strain-Engineered Interaction of Quantum Polar and Superconducting Phases. *Phys. Rev. Materials* **3,** 124801. doi:10.1103/PhysRevMaterials.3.124801 (2019).
224. Grande, T., Tolchard, J. R. & Selbach, S. M. Anisotropic Thermal and Chemical Expansion in Sr-Substituted $LaMnO_{3+\delta}$: Implications for Chemical Strain Relaxation. *Chem. Mater.* **24,** 338–345. doi:10.1021/cm2030608 (2012).
225. Weeks, W. T., Hecht, K. T. & Dennison, D. M. Inversion-Vibration and Inversion-Rotation Interactions in the Ammonia Molecule. *J. Mol. Spectrosc.* **8,** 30–57. doi:10.1016/0022-2852(62)90004-8 (1962).
226. Sakurai, J. J. & Napolitano, J. *Modern Quantum Mechanics* ISBN: 978-1-108-58728-0. doi:10.1017/9781108587280 (Cambridge University Press, 2020).
227. Halpern, A. M. & Glendening, E. D. Intrinsic Reaction Coordinate Calculations of the Inversion/Bending Potentials in the X and A States of Ammonia. *Chem. Phys. Lett.* **333,** 391–396. doi:10.1016/S0009-2614(00)01370-1 (2001).
228. Halpern, A. M., Ramachandran, B. R. & Glendening, E. D. The Inversion Potential of Ammonia: An Intrinsic Reaction Coordinate Calculation for Student Investigation. *J. Chem. Educ.* **84,** 1067. doi:10.1021/ed084p1067 (2007).
229. Nakamura, T. *et al.* On the Perovskite-Related Materials of High Dielectric Permittivity with Small Temperature Dependence and Low Dielectric Loss. *Ferroelectrics* **196,** 205–209. doi:10.1080/00150199708224163 (1997).
230. Atkins, P. W. & Friedman, R. *Molecular Quantum Mechanics* 5th ed. 537 pp. ISBN: 978-0-19-954142-3 (Oxford University Press, 2011).
231. Pal, S. *et al.* Origin of Terahertz Soft-Mode Nonlinearities in Ferroelectric Perovskites. *Phys. Rev. X* **11,** 021023. doi:10.1103/PhysRevX.11.021023 (2021).
232. Wentzcovitch, R. M. Invariant Molecular-Dynamics Approach to Structural Phase Transitions. *Phys. Rev. B* **44,** 2358–2361. doi:10.1103/PhysRevB.44.2358 (1991).

233. Kagawa, F. *et al.* Athermal Domain-Wall Creep near a Ferroelectric Quantum Critical Point. *Nat. Commun.* **7,** 10675. doi:10.1038/ncomms10675 (2016).
234. Salmani-Rezaie, S. *et al.* Order-Disorder Ferroelectric Transition of Strained $SrTiO_3$. *Phys. Rev. Lett.* **125,** 087601. doi:10.1103/PhysRevLett.125.087601 (2020).
235. Brooke, J., Rosenbaum, T. F. & Aeppli, G. Tunable Quantum Tunnelling of Magnetic Domain Walls. *Nature* **413,** 610–613. doi:10.1038/35098037 (2001).
236. Wördenweber, R. *et al.* Induced Ferroelectricity in Strained Epitaxial $SrTiO_3$ Films on Various Substrates. *J. Appl. Phys.* **102,** 044119. doi:10.1063/1.2773680 (2007).
237. Verma, A. *et al.* Ferroelectric Transition in Compressively Strained $SrTiO_3$ Thin Films. *Appl. Phys. Lett.* **107,** 192908. doi:10.1063/1.4935592 (2015).
238. Zhong, W., Vanderbilt, D. & Rabe, K. M. First-principles theory of ferroelectric phase transitions for perovskites: The case of $BaTiO_3$. *Phys. Rev. B* **52,** 6301–6312. doi:10.1103/PhysRevB.52.6301 (1995).
239. Samara, G. A. Nature of the Phase Transition in KTaO3 with Random Site Impurities. *Jpn. J. Appl. Phys.* **24,** 80. doi:10.7567/JJAPS.24S2.80 (1985).
240. Samara, G. A. & Boatner, L. A. Ferroelectric-to-relaxor crossover and oxygen vacancy hopping in the compositionally disordered perovskites $KTa_{1-x}Nb_xO_3$: Ca. *Phys. Rev. B* **61,** 3889–3896. doi:10.1103/PhysRevB.61.3889 (2000).
241. Samara, G. A. From Ferroelectric to Quantum Paraelectric: KTa1-xNbxO3 (KTN), A Model System. *AIP Conf. Proc.* **706,** 176–179. doi:10.1063/1.1780211 (2004).
242. Singh, D. J. Structure and energetics of antiferroelectric $PbZrO_3$. *Phys. Rev. B* **52,** 12559–12563. doi:10.1103/PhysRevB.52.12559 (1995).
243. Singh, D. J. Stability and phonons of $KTaO_3$. *Phys. Rev. B* **53,** 176–180. doi:10.1103/PhysRevB.53.176 (1996).
244. Nordheim, L. Zur Elektronentheorie Der Metalle. I. *Ann. Phys.* **401,** 607–640. doi:10.1002/andp.19314010507 (1931).
245. De Gironcoli, S., Giannozzi, P. & Baroni, S. Structure and thermodynamics of Si_xGe_{1-x} alloys from ab initio Monte Carlo simulations. *Phys. Rev. Lett.* **66,** 2116–2119. doi:10.1103/PhysRevLett.66.2116 (1991).
246. Marzari, N., de Gironcoli, S. & Baroni, S. Structure and phase stability of $Ga_xIn_{1-x}P$ solid solutions from computational alchemy. *Phys. Rev. Lett.* **72,** 4001–4004. doi:10.1103/PhysRevLett.72.4001 (1994).
247. Saitta, A. M., de Gironcoli, S. & Baroni, S. Structural and Electronic Properties of a Wide-Gap Quaternary Solid Solution: $Zn, Mg\ S, Se$. *Phys. Rev. Lett.* **80,** 4939–4942. doi:10.1103/PhysRevLett.80.4939 (1998).
248. Ramer, N. & Rappe, A. Application of a New Virtual Crystal Approach for the Study of Disordered Perovskites. *J. Phys. Chem. Solids* **61,** 315–320. doi:10.1016/S0022-3697(99)00300-5 (2000).
249. Bellaiche, L. & Vanderbilt, D. Virtual Crystal Approximation Revisited: Application to Dielectric and Piezoelectric Properties of Perovskites. *Phys. Rev. B* **61,** 7877–7882. doi:10.1103/PhysRevB.61.7877 (2000).
250. Ramer, N. J. & Rappe, A. M. Virtual-crystal approximation that works: Locating a compositional phase boundary in $Pb(Zr_{1-x}Ti_x)O_3$. *Phys. Rev. B* **62,** R743–R746. doi:10.1103/PhysRevB.62.R743 (2000).

251. Skjærvø, S. H. *et al.* Unconventional Continuous Structural Disorder at the Order-Disorder Phase Transition in the Hexagonal Manganites. *Phys. Rev. X* **9,** 031001. doi:10.1103/PhysRevX.9.031001 (2019).
252. Juraschek, D. M., Meier, Q. N. & Narang, P. Parametric Excitation of an Optically Silent Goldstone-Like Phonon Mode. *Phys. Rev. Lett.* **124,** 117401. doi:10.1103/PhysRevLett.124.117401 (2020).
253. Henkelman, G., Uberuaga, B. P. & Jónsson, H. A Climbing Image Nudged Elastic Band Method for Finding Saddle Points and Minimum Energy Paths. *J. Chem. Phys.* **113,** 9901–9904. doi:10.1063/1.1329672 (2000).
254. Kittel, C. Theory of Antiferroelectric Crystals. *Phys. Rev.* **82,** 729–732. doi:10.1103/PhysRev.82.729 (1951).
255. Moeller, J. *[Pw_forum] Phonon Omega or Nu? Factors of 2pi* E-mail. 2012. https://lists.quantum-espresso.org/pipermail/users/2012-September/025123.html (2022).
256. Tomioka, Y. *et al.* Enhanced Superconductivity Close to a Non-Magnetic Quantum Critical Point in Electron-Doped Strontium Titanate. *Nat. Commun.* **10,** 738. doi:10.1038/s41467-019-08693-1 (2019).
257. Allen, P. B. & Mitrović, B. in *Solid State Physics* (eds Ehrenreich, H., Seitz, F. & Turnbull, D.) 1–92 (Academic Press, 1983). doi:10.1016/S0081-1947(08)60665-7.
258. Zhou, J.-J., Hellman, O. & Bernardi, M. Electron-Phonon Scattering in the Presence of Soft Modes and Electron Mobility in $SrTiO_3$ Perovskite from First Principles. *Phys. Rev. Lett.* **121,** 226603. doi:10.1103/PhysRevLett.121.226603 (2018).
259. Wölfle, P. & Balatsky, A. V. Superconductivity at low density near a ferroelectric quantum critical point: Doped $SrTiO_3$. *Phys. Rev. B* **98,** 104505. doi:10.1103/PhysRevB.98.104505 (2018).
260. Ruhman, J. & Lee, P. A. Comment on "Superconductivity at low density near a ferroelectric quantum critical point: Doped $SrTiO_3$". *Phys. Rev. B* **100,** 226501. doi:10.1103/PhysRevB.100.226501 (2019).
261. Uwe, H. *et al.* Raman Scattering from Conduction Electrons in KTaO3. *J. Phys. Soc. Jpn.* **49,** 577–580 (1980).
262. Stengel, M. Electrostatic Stability of Insulating Surfaces: Theory and Applications. *Phys. Rev. B* **84,** 205432. doi:10.1103/PhysRevB.84.205432 (2011).
263. Mattheiss, L. F. Energy Bands for $KNiF_3$, $SrTiO_3$, $KMoO_3$, and $KTaO_3$. *Phys. Rev. B* **6,** 4718–4740. doi:10.1103/physrevb.6.4718 (1972).
264. Gattinoni, C. & Spaldin, N. A. Prediction of a Strong Polarizing Field in Thin Film Paraelectrics. *Phys. Rev. Research* **4,** L032020. doi:10.1103/PhysRevResearch.4.L032020 (2022).
265. Santander-Syro, A. F. *et al.* Orbital symmetry reconstruction and strong mass renormalization in the two-dimensional electron gas at the surface of $KTaO_3$. *Phys. Rev. B* **86,** 121107. doi:10.1103/PhysRevB.86.121107 (2012).
266. Reticcioli, M. *et al.* Competing Electronic States Emerging on Polar Surfaces. *Nat. Commun.* **13,** 4311. doi:10.1038/s41467-022-31953-6 (2022).
267. Setvin, M. *et al.* Polarity Compensation Mechanisms on the Perovskite Surface KTaO3(001). *Science* **359,** 572–575. doi:10.1126/science.aar2287 (2018).

268. Schooley, J. F. *et al.* Dependence of the Superconducting Transition Temperature on Carrier Concentration in Semiconducting $SrTiO_3$. *Phys. Rev. Lett.* **14,** 305–307. doi:10.1103/PhysRevLett.14.305 (1965).
269. Gastiasoro, M. N., Trevisan, T. V. & Fernandes, R. M. Anisotropic Superconductivity Mediated by Ferroelectric Fluctuations in Cubic Systems with Spin-Orbit Coupling. *Phys. Rev. B* **101,** 174501. doi:10.1103/PhysRevB.101.174501 (2020).
270. Gastiasoro, M. N. *et al.* Theory of Superconductivity Mediated by Rashba Coupling in Incipient Ferroelectrics. *Phys. Rev. B* **105,** 224503. doi:10.1103/PhysRevB.105.224503 (2022).
271. Kozii, V. & Fu, L. Odd-Parity Superconductivity in the Vicinity of Inversion Symmetry Breaking in Spin-Orbit-Coupled Systems. *Phys. Rev. Lett.* **115,** 207002. doi:10.1103/PhysRevLett.115.207002 (2015).
272. Kanasugi, S. & Yanase, Y. Spin-Orbit-Coupled Ferroelectric Superconductivity. *Phys. Rev. B* **98,** 024521. doi:10.1103/PhysRevB.98.024521 (2018).
273. Kanasugi, S. & Yanase, Y. Multiorbital ferroelectric superconductivity in doped $SrTiO_3$. *Phys. Rev. B* **100,** 094504. doi:10.1103/PhysRevB.100.094504 (2019).
274. Kozii, V., Bi, Z. & Ruhman, J. Superconductivity near a Ferroelectric Quantum Critical Point in Ultralow-Density Dirac Materials. *Phys. Rev. X* **9,** 031046. doi:10.1103/PhysRevX.9.031046 (2019).
275. Wemple, S. H. Some Transport Properties of Oxygen-Deficient Single-Crystal Potassium Tantalate ($KTaO_3$). *Phys. Rev.* **137,** A1575–A1582. doi:10.1103/PhysRev.137.A1575 (1965).
276. Meier, Q. N., Mingo, N. & van Roekeghem, A. *Finite temperature dielectric properties of $KTaO_3$ from first principles and machine learning: Phonon spectra, Barrett law, strain engineering and electrostriction* 2022. doi:10.48550/arXiv.2206.08296.
277. Pizzi, G. *et al.* Wannier90 as a Community Code: New Features and Applications. *J. Phys. Condens. Matter* **32,** 165902. doi:10.1088/1361-648X/ab51ff (2020).
278. Esswein, T. Exploring Ferroelectric Quantum Criticality and Superconductivity in KTaO3. *Master Thesis.* doi:10.3929/ethz-b-000560845 (2018).
279. Klein, A. *et al. A Theory of Criticality for Quantum Ferroelectric Metals* 2022. doi:10.48550/arXiv.2209.02733.